超音波を援用したSiCセラミックス内面の超精密加工の研究

Ultra-fine internal grinding of SiC ceramics with the assistance of ultrasonic vibration

2014年9月

曹　建国

Jianguo Cao

This page intentionally left blank.

CONTENTS

Abstract 1
Chapter 1 Introduction 3
1.1 Silicon carbide (SiC) Ceramics 3
1.2 Ultrasonic assisted internal grinding (UAIG) 5
1.2.1 Internal grinding 5
1.2.2 Ultrasonic assisted internal grinding (UAIG) 8
1.3 Objective of the study 10
1.4 Thesis organization 11
Reference 13
Chapter 2 Experiment apparatus and details 19
2.1 Principal of UAIG 19
2.2 Experiment apparatus 20
2.2.1. Ultrasonic spindle 20
2.2.2 Workpiece 22
2.2.3 Experiment setup 23
2.3 Measurement of UV amplitude 24
2.4 Experiment detail 25
2.5 Summary 26
Chapter 3 Machining characteristics of ultrasonic assisted internal grinding of SiC ceramics 27
3.1 Experiment conditions 27
3.2 Grinding forces 28
3.2 Form accuracy and surface roughness 29
3.4 Work-surface integrity 30
3.5 Grinding wheel wear 32
3.6 Subsurface damage 34
3.7 Summary 36
Reference 37
Chapter 4 Grinding force model and force reduction mechanism of UAIG of SiC ceramics 39
4.1 Introduction 39
4.2 Model development approach 40
4. 3 Model development details 41
4.3.1 Undeformed chip cross-sectional area 42
4.3.2 The undeformed chip length 43
4.3.3 The force model 45
4.4. Grinding force reduction mechanism in UAIG 48
4.5 Grinding forces predictions and model verification 51
4.5.1 Experimental determination of parameters k and k_1 51
4.5.2 Grinding forces predictions and model verification 52
Reference 57
Chapter 5 Material removal behavior in ultrasonic-assisted scratching of SiC ceramics with a single diamond tool 59
5.1 Introduction 59
5.2 Operation principle and kinematic characteristics of UAS 60

5.2.1 Operation principle....60
5.2.2 Kinematic characteristics....62
5.3 Experimental details....65
5.3.1 Experimental setup and procedure....65
5.4 Experimental results and discussions....68
5.4.1 SEM observation of scratching grooves....68
5.4.2 Cross-sectional profiles and depths/widths of grooves....73
5.4.3 Scratching forces....80
5.4.4 Ductile-brittle transition mechanism....81
5.4.5 Cutting efficiency and nature of material removal....86
5.5. Simulation details....88
5.5.1 Simulation Model Development....89
5.6 Simulation results and discussion....90
5.6.1 Cutting force....90
5.6.2 Material removal process....92
5.6.3 Scratching-induced stress....96
5.7 Summary....98
Reference....100
Chapter 6 Approaches to high accuracy internal grinding of SiC ceramics....103
6.1 Internal grinding of SiC ceramics in ductile mode....103
6.2. Grinding efficiency....107
6.3 High accuracy internal grinding of SiC ceramics....108
6.3.1 Surface roughness....109
6.3.2 Roundness and cylindricity....112
6.3.3 Straightness....115
6.4 Summary....118
Reference....118
Chapter 7 Conclusion and future recommendation....121
7.1 Conclusion....121
7.2 Future recommendation....123
Acknowledgements....125
Accomplishments....127

Abstract

Poor machinability of hard-to-machine materials limits their applications in industries. Ultrasonic assisted grinding (UAG), a hybrid machining process combining material-removal mechanisms of diamond grinding and ultrasonic machining, is one cost-effective machining method for these materials. This study focuses on internal grinding of silicon carbide (SiC) ceramics with the assistance of ultrasonic. The motivations for this study were outlined first. Following the processing principal of ultrasonic assisted internal grinding (UAIG), the UAIG experiment apparatus were constructed. With the constructed experiment rig, experiments on machining characteristics were performed. The experiment results evidence that grinding force in UAIG are significantly reduced compared with those in conventional internal grinding (CIG); the greater improvement of the form accuracy and surface quality are achieved in UAIG compared with those in CIG; grinding wheel wear are alleviated in UAIG compared to that in CIG.

Grinding force is an important issue in grinding process. In order to optimize grinding parameters to achieve high product quality and productivity, a grinding force model for UAIG of SiC ceramics is developed. Effects of grinding parameters (workpiece rotational speed, wheel infeed rate, wheel rotational speed, ultrasonic vibration (UV) amplitude, and the oscillation frequency), on grinding force are predicted. In addition, the grinding force reduction mechanism in UAIG is explored. The experiment results show that grinding force reduction is attributed to the formation of the smaller the undeformed chip cross sectional area.

To deeply investigate the material removal mechanism in ultrasonic assisted internal grinding of SiC ceramics, the ultrasonic assisted scratching (UAS) tests were performed on SiC ceramics with a self-designed ultrasonic unit. Besides, a validated simulation model is developed to further investigate material removal mechanism in UAS. The obtained results evidence that: the scratching groove formed appears straight in the CS process while it is sinusoidal in the UAS process; the UV in the direction that vertical to work-surface strongly contributes to the material removal,

whereas the UV in the direction that parallel to work-surface only results in variation of the cutting trace and hardly contributes to the material removal in the UAS process; the cutting ability of the tool was significantly improved by the assistance of the UV; the impact and cutting action at the tool tip on the machining surface are the main factors contributing to the material removal.

The last part of this study is to extend the method so as to open a door to potential industrial applications. The results show that critical depth of cut in UAIG is deeper than that CIG, meaning that ductile mode grinding is easily achieved in UAIG; high accuracy can be achieved by UAIG.

All in all, this study confirms that UAIG is a highly effective processing method for SiC ceramics. The technology has the potential to being further extend to other materials.

Chapter 1 Introduction

1.1 Silicon carbide (SiC) Ceramics

Ceramic materials play an influential role in the progress of many fields of modern technologies, such as communication and information technology, energy and environmental technology, transportation and production technology, as well as the life sciences [1]. Especially, Silicon carbide (SiC) is an important non-oxide ceramic which has deserves much attention [2].

The properties of ceramic materials are dependent on the characteristics of the microstructure, which in turn is influenced by the characteristics and manufacturing process (raw material properties, additive properties, molding conditions, sintering conditions, etc.) of the material [3]. Fig. 1.1 shows microstructures of SiC ceramics which were produced by sintering method. Due to uniform microstructure free of abnormal grain growth, SiC ceramics is possible to have an extremely stable quality. Table 1 shows the material properties of SiC ceramics used for this study. It is known that SiC ceramics has exclusive properties such as high hardness and strength, chemical and thermal stability, etc. All of these qualities make SiC ceramics a perfect candidate for high power, high temperature electronic devices as well as abrasion and cutting applications [3].

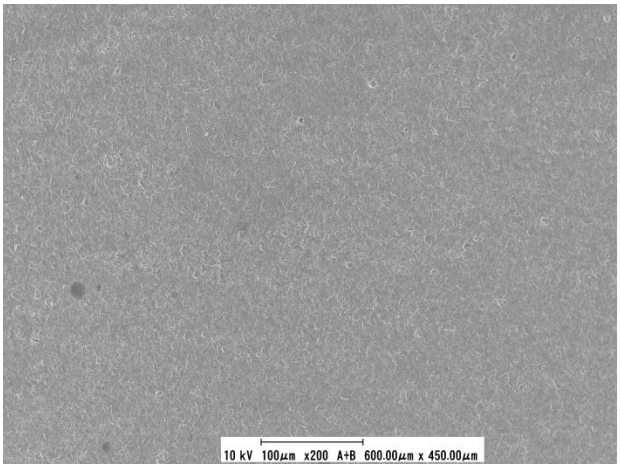

Fig. 1.1 SEM image of microstructure of SiC ceramics used for this study.

Table 1.1 Silicon Carbide Ceramics Properties (Obtained from JAPAN FINE CERAMICS CO., LTD.)

Mechanical	Density	g/cm^3	3.1
	Porosity	%	0
	Flexural Strength	MPa	490
	Elastic Modulus	GPa	430
	Poisson's Ratio	—	0.16
	Compressive Strength	MPa	3900
	Hardness	Kg/mm^2	2800
	Fracture Toughness K_{IC}	$MPa•m^{1/2}$	4.6
Thermal	Thermal Conductivity	W/m•°K	158
	Coefficient of Thermal Expansion	10^{-6}/℃	4.0
	Specific Heat	J/Kg•°K	750

In recent years, the demands for high precision and efficient fabrication of aspherical lens used for X-ray telescopes, digital cameras etc. have been rapidly increased with the development of IT industry. In generally, the aspherical lenses are produced by using internal shape mold with a press molding method [4]. As shown in Fig.1.2, in the aspherical lens manufacturing process, the mold is used in severe environment like high temperature and high pressure, therefore, the mold sleeves should have high-temperature characteristic and high wear resistance. Ceramics, especially, silicon carbide materials (SiC) exhibit good material properties, which are superior to those of other materials, these properties make SiC become a perfect material for molding dies used for hot-press molding of glass lenses [5].

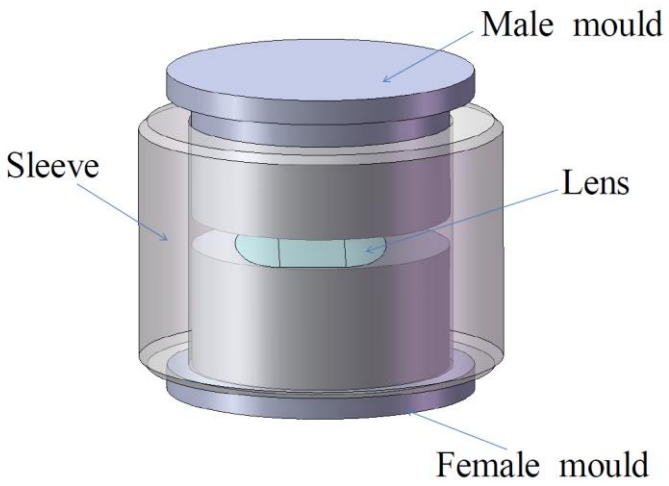

Fig.1.2 Illustration for aspherical lens manufacturing.

1.2 Ultrasonic assisted internal grinding (UAIG)

1.2.1 Internal grinding

In aspherical lens manufacturing, as a step to obtain the mold with high quality and long working life, it is strongly demanded to precisely machine the internal cylindrical surface of the sleeve. Meanwhile, as SiC ceramics is a typical hard-brittle and difficult-to-machine material, conventionally internal grinding with diamond grinding wheel is performed for machining the internal surfaces of SiC ceramics sleeve to obtain high finish accuracy.

Depending on the type of workpiece holding, internal grinding can be divided into chucking type and centerless type (Fig. 1.3 and 1.4) [6]. Chucking type can also be classified as (a) both the workpiece and the grinding rotating type (Fig. 1.3(a)) (b) planetary type (Fig. 1.3(b)). In planetary type, the workpiece is held by chuck and doesn't rotate, whereas the grinding wheel rotates at rotational speed and dose a planetary motion respective to the workpiece in the grinding process. Centerless internal grinding type can be divided into (a) roll supported grinding type (Fig. 1.4(a)) (b) shoe supported grinding type (Fig. 1.4(b)).

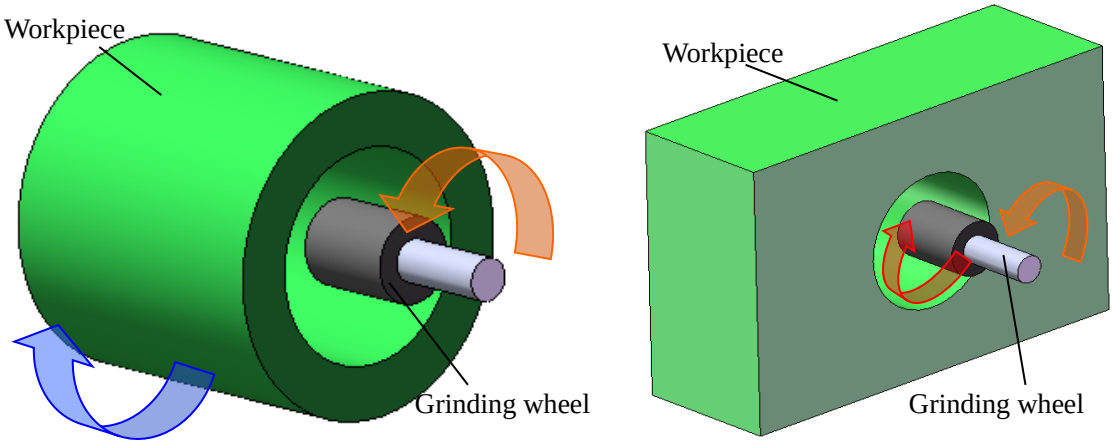

(a)Workpiece and wheel rotating type (b) Planetary type

Fig. 1.3 Chucking internal grinding

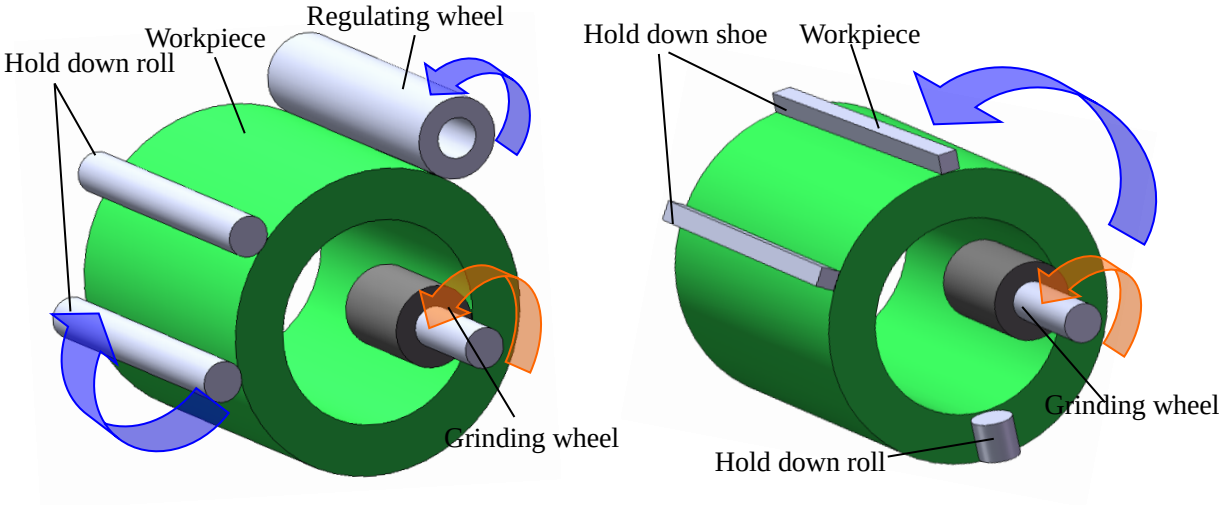

(a)Roll supported type (b) Shoe supported type

Fig. 1.4 Centerless internal grinding

Until now, much attention has been paid to internal grinding. The related studies mainly focus on the machining characteristics, optimization of the internal grinding parameters, grinding mechanism, and high efficient internal grinding method. Kakuda et al. found that formation error occurring from continuous operation in internal grinding is due to the function of the respective relative positions of the center of the workpiece and the grinding wheel spindle and, also, of the diamond cutting edge [7, 8]. Teraya et al. experimentally investigated the influence of the grinding parameter on the grinding accuracy [9]. The results showed that surface roughness

and roundness becomes bad when grinding wheel changes direction in traverse grinding, owing to the impact of the grinding wheel on the workpiece. In their later study [10], they investigated the influence of the grinding parameter on formation accuracy. Yamamoto et al. studied the dynamic behavior of spindle in internal grinding and found that the spindle in operation process has two surpassed frequencies, one is caused by unbalanced weight of the spindle and the other one is due to unsymmetrical bending rigidity of the spindle resulting from the existence of screw holes for fastening up the wheel shaft [11].

To optimize the internal grinding parameters, Nakajima Toshikatsu et al. determined oscillation conditions for optimizing surface roughness in internal grinding and concluded that the improvement mechanism of surface roughness is attributed to the crossing phenomenon of grinding paths; the existence of the restricted interference phenomenon results in the rougher the surface roughness of workpiece; [12, 13]. Tsukamoto et al. investigated the optimal geometrical accuracy in internal oscillation grinding of deep straight holes [14]. To elucidate internal grinding mechanism, Nakajima Toshikatsu et al. investigated behavior of thermal deformations of wheel and workpiece and form generation mechanism in internal grinding process. The results showed that the workpiece surface expands with the thermal deformation in the opposite direction of wheel surface in the internal plunge grinding; the ground workpiece profile becomes an extremely concave profile due to the thermal deformation of wheel [15]. In their later study, they analyzed taper generation mechanism in deep hole oscillation internal grinding and found that the taper error of workpiece can be significantly improved with the surface roughness in the retraction grinding method; the extending of spark-out grinding time has an influential effect on the taper generation in the retraction grinding, owing to the stiffness of the grinding wheel shaft and workpiece spindle [16] Zhou Li-qun et al. investigated the thermal deformation in internal grinding by FEM method [17]. The results found that the thermal deformation of the ground cirque is basically symmetrical in a diamond shape, but the deformations of the inner circle and the outer circle are not uniform, and the inner circle thermal deformation may be negative or

positive.

Meanwhile, research attempts have been devoted to improve internal grinding efficiency. J. MARKUL and B. SŁOWISKI gived an analysis of the effectiveness of the grinding at higher peripheral speeds and higher hardness of grinding wheels in internal grinding [18]. To defeat some problems of internal grinding such as poor enrichment of coolant lubricant, deflection of grinding tool and the resulting inaccuracy, low material removal and high heat generation because of long contact length, T. Tawakoli et al. proposed a new kinematic [19]. The experimental result showed that this method can enhance the cutting speed and reduce contact surface between the grinding wheel and workpiece compared to conventional internal grinding. Qian Jun et al. [20, 21] and Kaifei Zhang et al. [22] introduced electrolytic in-process dressing (ELID) into internal grinding. Their experimental results showed that mirror surface grinding is achievable on an ordinary grinder with ELID.

However, although much attention has been paid to internal grinding, there are still some disadvantages in conventional internal grinding (CIG) [6]: an ultra-high speed grinding spindle with rotational speed up to 200 thousand rpm should be installed on the internal grinder, leading to an inevitable huge cost; as the spindle rotates at an ultra-high speed, the bearings will easily get heated and the spindle will easily generate vibration, resulting in difficulty in obtaining high finishing accuracy; the contact arc between grinding wheel and workpiece is longer than that in cylindrical or surface grinding, easily resulting in heavy loading of the wheel; coarse grits wheel should be employed to prevent the wheel from loading but a high quality finishing surface is difficult to get.

Consequently, a new grinding method is required for the high precision and efficient processing of internal cylindrical surfaces of SiC ceramic components.

1.2.2 Ultrasonic assisted internal grinding (UAIG)

Ultrasonic-assisted grinding (UAG), a hybrid machining process combining

grinding and ultrasonic vibration (UV), can enhance grinding efficiency and improve work-surface quality owing to its decreased grinding forces and reduced wheel wear compared with CG [23-25]. Thus, UAG is considered to be a promising technique for ceramics grinding. Different types of UAG techniques, e.g., one-dimensional UAG (1D-UAG), two-dimensional UAG (2D-UAG), and elliptical-UAG (EUAG), have been proposed. In 1D-UAG, the UV is usually applied to the grinding wheel in either the vertical direction or parallel to the work surface. The former is called VUAG (vertical UAG), and the latter is called AUAG (axial UAG) [26]. VUAG is characterized by a much lower grinding force and higher material removal rate (MRR) while maintaining slightly increased wheel wear and surface roughness [27]; the AUAG benefits the grinding process, significantly, by decreasing the thermal load and improving the surface quality [28]. To combine the merits of both VUAG and AUAG, Liang and Wu proposed the EUAG technique [26, 29] and their experimental investigations involving monocrystal sapphire with a resin bond diamond wheel showed that the grinding forces and the work-surface roughness can be decreased by 30% and 20%, respectively, compared to CG. To further improve the work-surface quality, Yan and Zhao developed the 2D-UAG technique [30, 31]. In this method, the UV is simultaneously applied to the workpiece from two directions; one is in the same direction as that of the wheel peripheral speed and the other is along the wheel axis. The experimental results involving nano-ZrO_2 ceramics indicated that the quality of the work surface attained is even better than that obtained from AUAG [30]. However, in either EUAG or 2D-UAG, the UV must be simultaneously generated in two directions, resulting in complicated machining equipment structures. This further increases the equipment expense and multiplies the difficulty in equipment maintenance. Consequently, in practical UAG, the predominant approach is types of 1D-UAG, i.e., AUAG or VUAG rather than 2D-UAG and EUAG.

Utilizing the advantages of the 1D-UAG methods, research attempts have been devoted to the application of both AUAG and VUAG to hard and brittle materials. The results showed that the work surface quality can be greatly improved with a slight decrease in grinding force in the AUAG of the Al_2O_3 ceramic workpiece [32]

compared to CG; the grinding force can also be significantly reduced. Particularly, Mult et al. found that utilizing VUAG resulted in a slight increase in wheel wear due to the grinding wheel striking the machined workpiece [27]. To elucidate the material removal mechanism in the 1D-UAG methods, some studies focused on the change pattern and grinding force reduction in AUAG [33-35] by using a combination of numerical simulation and experimentation. Lee and Chan found that the increased vibration amplitude resulted in an increased MRR in AUAG due to the increased energy imparted to the material [35]. Zhang et al. thought the average cutting velocity in AUAG was higher than that in CG, which is a main factor contributing to the reduction of force [33]. Additionally, Farhadi et al. believed that the elimination of the sliding and plowing region along the cutting path during VUAG was the reason for force reduction, as determined by the numerical simulation investigation [34].

On the other hand, 1D-UAG methods has been introduced into internal grinding. Kumabe [36, 37] performed ultrasonic assisted internal grinding (UAIG) of metal materials such as aluminum, copper and steel. The obtained results showed that the grinding efficiency was improved and grinding forces were reduced for the sake of the presence of UV. Wu et al. [38] found that the normal and tangential forces in UAIG of stainless steel were smaller by 65% and 70%, respectively, and the surface roughness was smaller by 20% than those in CIG. In M. Fujimoto et al.'s work [39], the machining characteristics of the UAIG of tungsten were experimentally compared with those of the CIG, showing that the normal and tangential grinding forces and the surface roughness in UAIG were smaller by 11%, 41%, and 53%, respectively, than those in CIG. This study confirms that UAIG is a highly effective processing method.

1.3 Objective of the study

Although there has been several studies focused on UAIG, most of them involved metal materials and little attention has been paid to the hard-brittle materials, especially ceramics. Further, the previous studies only revealed the fundamental

characteristics of UAIG, e.g. the effect of UV on the grinding forces, surface roughness and form accuracy, but the material removal behavior, a key to understand the performance of UAIG process, has not yet been explored sufficiently.

In this study, toward the development of an alternative machining method for the internal grinding of SiC ceramics, the UAIG technique is applied to the internal grinding of SiC ceramics. For this purpose, an experimental rig was constructed by installing an ultrasonic spindle onto a CNC internal grinder and experimental investigations on the machining characteristics of SiC ceramics workpiece were performed on the constructed rig. As grinding force plays an influential role in work-surface finish in grinding process, a model is necessary for optimizing input variables to achieve high product quality and productivity. However, to the best of our knowledge, there are few reports on modeling grinding force in ultrasonic assisted internal grinding (UAIG). Thus, a theoretical model was presented to predict the grinding force in UAIG of SiC ceramics in this study. Generally, UAIG is considered as one type of UAG techniques. Although UAG has been extensively employed in manufacturing industries for processing hard and brittle materials, its potential has not been sufficiently developed because the material removal mechanism in UAG has not been elucidated. Therefore, the material removal mechanism in the UAG of silicon carbide (SiC) ceramics has been explored by investigating the material removal behaviors in ultrasonic-assisted scratching (UAS) of SiC ceramics.

1.4 Thesis organization

This thesis is divided into 7 chapters. The outline of thesis organization is shown in Fig. 1.5.

In chapter 1, silicon carbide (SiC) ceramics and internal grinding were briefly introduced. Prevailing technologies, i.e., ultrasonic assisted grinding and ultrasonic assisted internal grinding is outlined.

In chapter 2, the principal of UAIG is in the foremost place and followed by the introduction of UAIG experimental rig. At last, experimental condition under which

the experiments were performed are listed.

In chapter 3, investigations on the machining characteristics of SiC ceramics workpiece are performed on the constructed rig. CIG tests involving the same workpiece are also carried out on the same experimental rig for comparison. The effects of the UV on the grinding forces, the surface roughness, the form accuracy, and grinding wheel wear are revealed. Meanwhile, the topographic features of work-surfaces and the subsurface damages are observed as well to clarify the material removal behavior.

In chapter 4, a theoretical model is presented to predict the grinding force in UAIG of SiC ceramics. This model stems from undeformed chip length resulting from the relative motion between the grinding wheel and the workpiece. After analyzing the cutting action of an active individual grain, normal and tangential force models for the UAIG of SiC ceramics are developed. Using the developed model, the influence of many grinding parameters on grinding force is predicted. Finally, the grinding force reduction mechanism is explored.

In chapter 5, to deeply investigate the material removal mechanism in UAG of hard and brittle materials, the ultrasonic assisted scratching (UAS) tests are performed on SiC ceramics with a self-designed ultrasonic unit. Besides, a validated simulation model is developed to further investigate the differences between UAS and conventional scratching (CS). The combination of experimental tests and simulation will provide key insights into the single diamond tool scratch process that neither of the methods could provide on its own.

In chapter 6, experiment investigation of UAIG of SiC ceramics from an industrial view is performed.

In chapter 7, conclusions, and contributions of this research is presented. It also provided recommendations for further work in this direction.

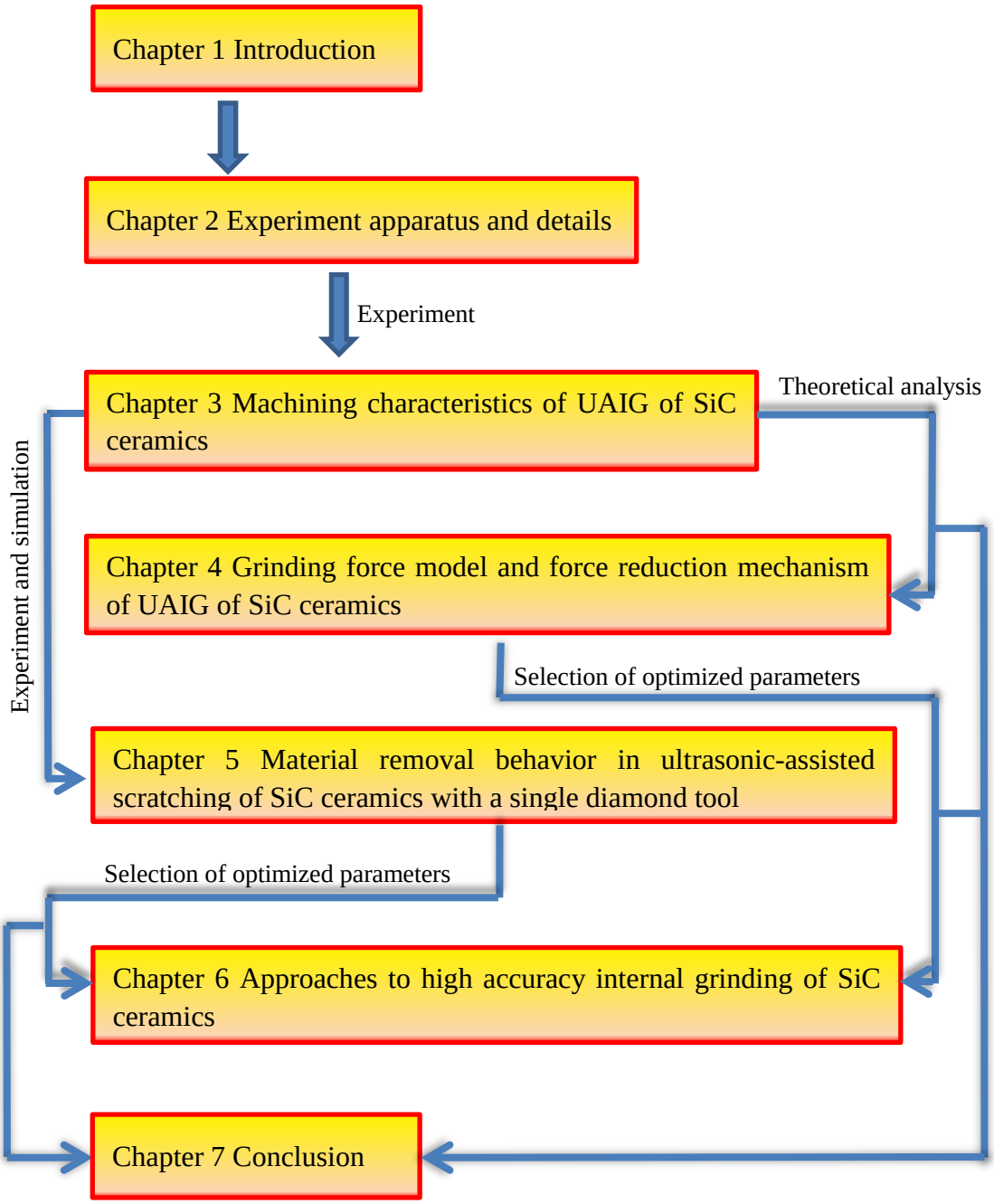

Fig. 1.5 Outline of thesis organization

Reference

[1] Greil, P. Advanced engineering ceramics. *Advanced materials* **2002**, *14* (10), 709.

[2] Harris, G. L., Properties of silicon carbide, Iet, 1995.

[3] Somiya, S. ; Inomata, Y., Silicon Carbide Ceramics-1: Fundamental and Solid Reaction, Springer, 1991.

[4] Namba, Y. ; Shimomura, T. ; Fushiki, A. ; Beaucamp, A. ; Inasaki, I. ; Kunieda, H. ; Ogasaka, Y. ; Yamashita, K. Ultra-precision polishing of electroless nickel molding dies for shorter wavelength applications. *CIRP Annals-Manufacturing Technology* **2008**, *57* (1), 337-340.

[5] Hall, C. ; Tricard, M. ; Murakoshi, H. ; Yamamoto, Y. ; Kuriyama, K. ; Yoko, H., New mold manufacturing techniques, in: Optics & Photonics 2005, International Society for Optics and Photonics, 2005, pp. 58680V-58680V-58610.

[6] Nomura, M., Study of ultrasonic vibration assisted internal grinding of small holes, Doctoral Dissertation, Tohoku University. (In Japanese).

[7] 角田馨, 内面研削盤における自動寸法制御機構の工作制度に及ぼす影響 : 第 1 報 自動定寸による研削. *精密機械* **1960**, *26* (305), 318-322.

[8] 角田馨, 内面研削盤における自動寸法制御機構の工作制度に及ぼす影響 : 第 2 報 自動範測による研削. *精密機械* **1960**, *26* (305), 323-327.

[9] 寺谷忠郎; 中尾隆一; 昌俊日浦. 内面研削盤の研削精度向上に関する研究. *精密機械* **1963**, *29* (347), 913-921.

[10] 寺谷忠郎, 内面研削の形状精度について. *精密機械* **1973**, *39* (460), 461-466.

[11] 山本明 ; 中村示; 三平恵一, 軸付き砥石を用いた内面研削における砥石軸の挙動. *精密機械* **1979**, *45* (530), 168-173.

[12] 西村健; 稲崎一郎; 山本直樹. 内面研削サイクルの最適化に関する研究. *日本機械学會論文集. C 編* **1989**, *55* (515), 1808-1813.

[13] 中島利勝; 塚本真也; 寺岡忠典; 小野祐一郎, 内面研削加工の表面粗さから考察した最適オシレーション条件決定法. *精密工学会誌* **1999**, *65* (4), 604-609.

[14] 塚本真也; 大橋一仁; 吉原啓太; 吉田哲弘; 中島利勝, 内面研削の深穴オシレーション加工における最適形状制御法の開発. *精密工学会誌論文集* **2004**, *70* (2), 263-268.

[15] 中島利勝; 塚本真也; 池上直久, 内面研削における砥石と工作物の熱変形挙動から考察した形状創成機構の研究. *精密工学会誌* **1995**, *61* (1), 127-131.

[16] 中島利勝; 塚本真也; 小合勇; 崔信堅, 深穴内面オシレーション研削におけるテーパ形成機構の解明とその改善策の提案. *精密工学会誌* **2001**, *67* (2), 289-294.

[17] Li-qun, Z. ; Yu-ping, L. ; Zhi-gang, C. Thermal deformation simulation for an internal grinding cirque by finite element method. *Int J Adv Manuf Technol* **2009**, *43* (5-6), 455-461.

[18] Markul, J. ; SŁOwiŃSki, B. Efficiency improvement in internal grinding. *Archives of Civil and Mechanical Engineering* **2006**, *6* (2), 77-86.

[19] Tawakoli, T. ; Rasifard, A. ; Rabiey, M. High-efficiency internal cylindrical grinding with a new kinematic. *International Journal of Machine Tools and Manufacture* **2007**, *47* (5), 729-733.

[20] Qian, J. ; Ohmori, H. ; Lin, W. Internal mirror grinding with a metal/metal–resin bonded abrasive wheel. *International Journal of Machine Tools and Manufacture* **2001**, *41* (2), 193-208.

[21] Qian, J. ; Li, W. ; Ohmori, H. Precision internal grinding with a metal-bonded diamond grinding wheel. *Journal of Materials Processing Technology* **2000**, *105* (1), 80-86.

[22] Zhang, K. ; Ren, C. ; Yang, L. ; Li, Q. ; Jin, X. Precision internal grinding of bearing steel based on the state control of oxide layer with electrolytic in-process dressing. *Journal of Materials Processing Technology* **2012**, *212* (7), 1611-1621.

[23] Peng, Y. ; Liang, Z. ; Wu, Y. ; Guo, Y. ; Wang, C. Characteristics of chip generation by vertical elliptic ultrasonic vibration-assisted grinding of brittle materials. *Int. J. Adv. Manuf. Technol.* **2012**, *62* (5-8), 563-568.

[24] Peng, Y. ; Wu, Y. B. ; Liang, Z. Q. ; Guo, Y. B. ; Lin, X. An experimental study of ultrasonic vibration-assisted grinding of polysilicon using two-dimensional vertical workpiece vibration. *Int. J. Adv. Manuf. Technol.* **2011**, *54* (9-12), 941-947.

[25] Qu, W. ; Wang, K. ; Miler, M. H. ; Huang, Y. ; Chandra, A. Using vibration-assisted grinding to reduce subsurface damage. *Precis. Eng.* **2000**, *24* (4), 329-337.

[26] Liang, Z. ; Wu, Y. ; Wang, X. ; Zhao, W. A new two-dimensional ultrasonic

assisted grinding (2D-UAG) method and its fundamental performance in monocrystal silicon machining. *Int. J. Mach. Tools Manuf.* **2010**, *50* (8), 728-736.

[27] Mult, H. ; Spur, G. ; Holl, S. Ultrasonic assisted grinding of ceramics. *J. Mater. Process. Technol.* **1996**, *62* (4), 6.

[28] Denkena, B. ; Friemuth, T. ; Reichstein, M. ; Tönshoff, H. Potentials of different process kinematics in micro grinding. *CIRP Annals-Manufacturing Technology* **2003**, *52* (1), 463-466.

[29] Liang, Z. ; Wang, X. ; Wu, Y. ; Xie, L. ; Liu, Z. ; Zhao, W. An investigation on wear mechanism of resin-bonded diamond wheel in Elliptical Ultrasonic Assisted Grinding (EUAG) of monocrystal sapphire. *J. Mater. Process. Technol.* **2012**, *212* (4), 868-876.

[30] Yanyan, Y. ; Bo, Z. ; Junli, L. Ultraprecision surface finishing of nano-ZrO2 ceramics using two-dimensional ultrasonic assisted grinding. *Int. J. Adv. Manuf. Technol.* **2009**, *43* (5-6), 462-467.

[31] Gao, G. F. ; Zhao, B. ; Xiang, D. H. ; Kong, Q. H. Research on the surface characteristics in ultrasonic grinding nano-zirconia ceramics. *J. Mater. Process. Technol.* **2009**, *209* (1), 32-37.

[32] ZHENG, J. x. ; XU, J. w. Experimental Research on the Ground Surface Quality of Creep Feed Ultrasonic Grinding Ceramics (Al_2O_3). *Chin. J. Aeronaut.* **2006**, *19* (4), 359-365.

[33] Klecka, M. ; Subhash, G. Grain size dependence of scratch-induced damage in alumina ceramics. *Wear* **2008**, *265* (5-6), 612-619.

[34] Farhadi, A. ; Abdullah, A. ; Zarkoob, J. ; Pak, A. Analytical and Numerical Simulation of Ultrasonic Assisted Grinding. *ASME 2010 10th Biennial Conference on Engineering Systems Design and Analysis* **2010**, *4*, 763-768.

[35] Lee, T. ; Chan, C. Mechanism of the ultrasonic machining of ceramic composites. *J. Mater. Process. Technol.* **1997**, *71* (2), 195-201.

[36] Kumabe, J. Study on Ultrasonic Internal Grinding by Using the Longitudinally Vibrated Grinding Wheel : 1st Report, Traverse Ultrasonic Cutting. *Transactions of*

the Japan Society of Mechanical Engineers **1961**, *27* (181), 1404-1411.

[37] Kumabe, J. ; Ito, Y. Study on Ultrasonic Internal Grinding by Using the Longitudinally Vibrated Grinding Wheel : 2nd Report, The Outline of the Effects. *Transactions of the Japan Society of Mechanical Engineers* **1961**, *27* (181), 1412-1418.

[38] Wu, Y. ; Nomura, M. ; Kato, M. ; Tachibana, T. Fundamental Investigation of Internal Ultrasonic Vibration Assisted Grinding of Small Holes. *Proceedings of International Conference on Leading Edge Manufacturing in 21st century : LEM21* **2003**, *2003*, 145-150.

[39] Fujimoto, M. ; Wu, Y. ; Cao, J., High Precision Ultrasonically Assisted Internal Grinding (UAIG) of Difficult-to-machining Materials using Metal Bonded Diamond Wheels, in: The 6th International Conference on Leading Edge Manufacturing in 21st Century, 2011.

This page intentionally left blank.

Chapter 2 Experiment apparatus and details

This chapter mainly focuses on the UAIG apparatus. First, the principle of UAIG is described. Then, in order to realize the processing principle of UAIG in practice, an experimental rig is constructed. The UAIG apparatus will be introduced. Before UAIG tests, the UV amplitude of the grinding wheel should be measured. Thereby, the measurement method of UV amplitude and results are presented. At last, the detailed experiment conditions are also listed out along with machining characteristics evaluation method.

2.1 Principal of UAIG

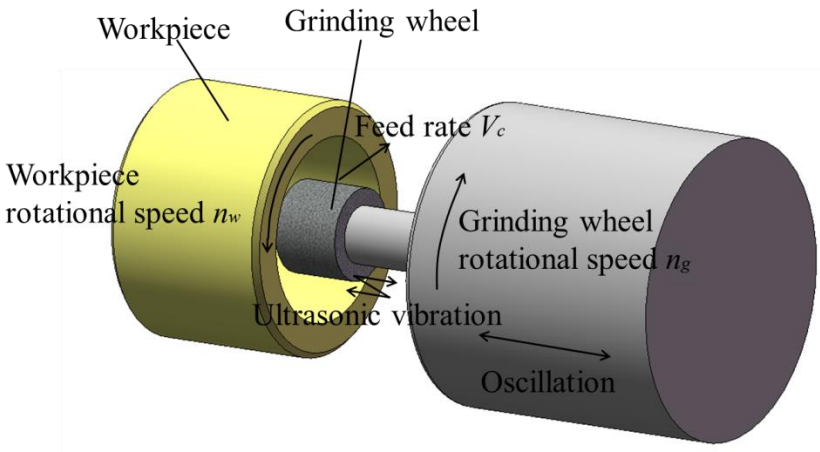

Fig. 2.1 Schematic illustration of the principle for UAIG

Fig. 2.1 shows the schematic illustration the principle of ultrasonic assisted internal grinding (UAIG). During internal grinding operations, the metal bonded diamond grinding wheel rotating at a rotational speed of n_g and ultrasonic vibration adding along its axis (frequency f, amplitude A), is fed in the workpiece radial direction at an infeed rate of V_c. Thus, the material of the workpiece rotating at a rotational speed of n_w is removed by the cutting action of the wheel. In addition, an oscillation motion is given to the grinding wheel along its axis to improve the finishing surface.

It is well known that the finishing accuracy is significantly affected by the truing

accuracy of the grinding wheel. In conventional grinding, the truing accuracy is hindered when using a rotary GC wheel dresser because the structure of the grinding wheel shaft leads to a low stiffness, therefore, it is easy to be deformed by the truing force [7]. In order to overcome such disadvantages, the ultrasonic assisted truing and dressing method was proposed, the principle is as shown in Fig. 2.2.

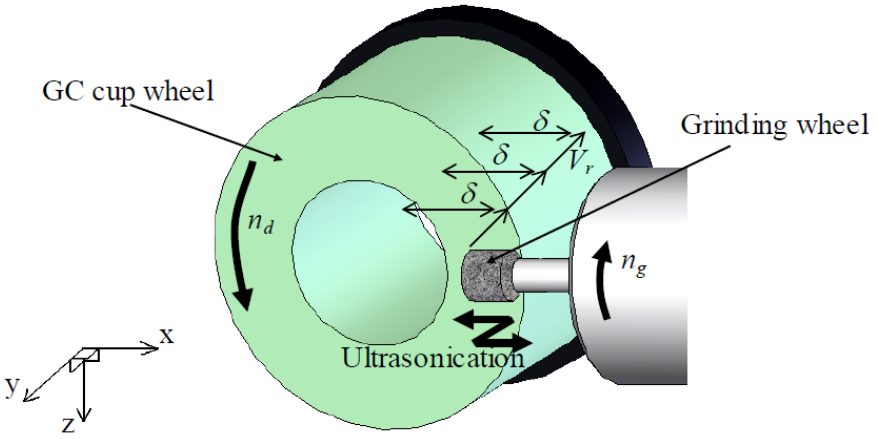

Fig. 2.2 Schematic illustration of the ultrasonic assisted truing and dressing

As shown in Fig. 2.2, during truing and dressing operations, the GC cup wheel rotating at a speed of n_d, reciprocates along the grinding wheel axis (x-direction) at a speed V_r, and is fed toward the grinding wheel in its radial direction (y-axis) at a feed rate of δ per reciprocation cycle. Ultrasonic vibration (frequency f, amplitude A) is added along the x-axis and rotation around the x-axis at a speed of n_g.

2.2 Experiment apparatus

2.2.1. Ultrasonic spindle

Fig. 2.3 shows the ultrasonic spindle used for UAIG (URT40 by Takesho Co., Ltd.). This spindle incorporated a rotary spindle with resonance frequency of 40kHz. The maximum rotational speed of the spindle is 8000rpm. The rotational speed of the spindle and vibration amplitude of the grinding wheel are controlled by the control

panel as shown in Fig. 2.4

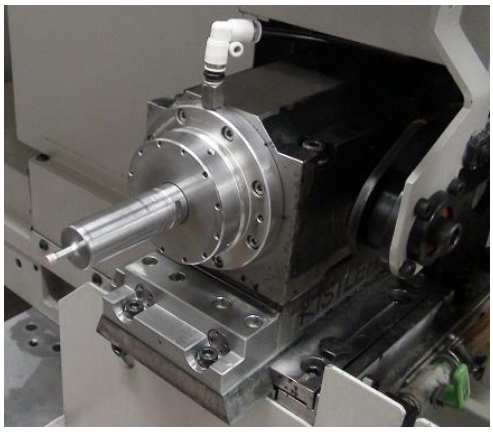

Fig. 2.3 Ultrasonic spindle

Fig. 2.4 Ultrasonic spindle controller

2.2.2 Grinding wheel

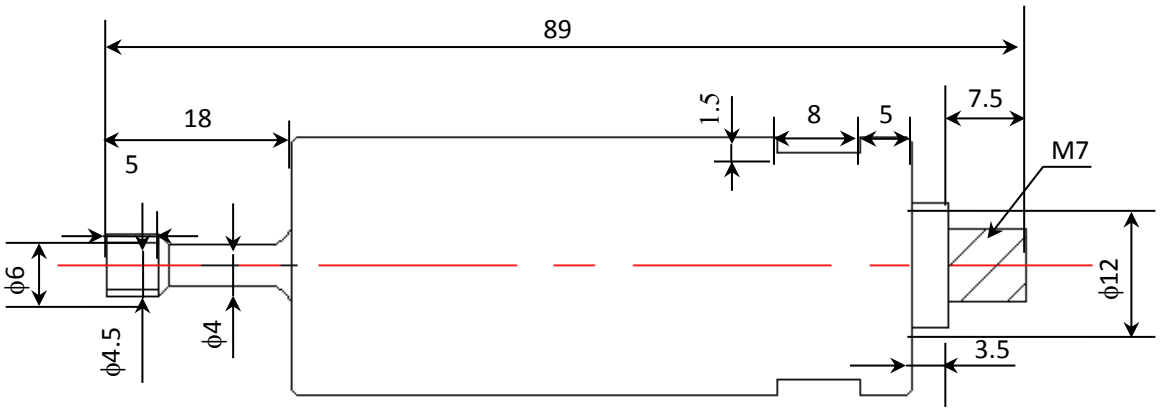

(a) Structure of grinding wheel

(b) Grinding wheel

Fig. 2.5 Grinding wheel for UAIG

Fig. 2.5 shows the grinding wheel used for UAIG tests. The diameter of the grinding wheel is ϕ6mm, length is 5mm. Grinding wheel is metal bond diamond wheel with mesh size #140～5000, concentration 100, and grade P.

2.2.2 Workpiece

Fig. 2.6 shows workpiece used for UAIG tests. The material is SiC ceramics and the material properties are shown in table 1.1. Dimensional size is ϕ12 (inner)×ϕ22 (outer)×t13 mm.

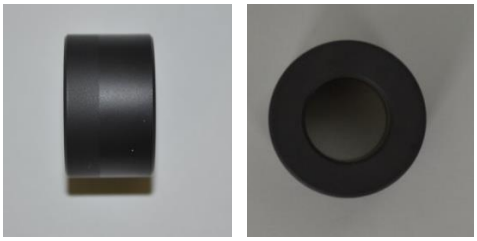

Fig. 2.6 Workpiece used for UAIG tests

2.2.3 Experiment setup

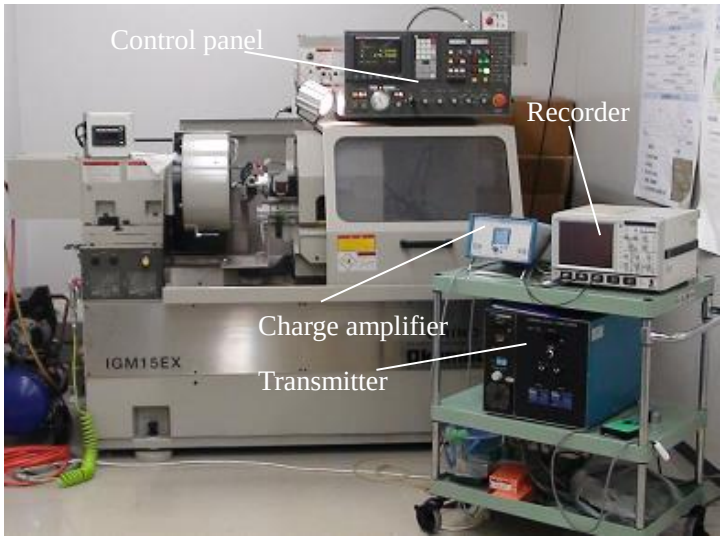

(a) Internal grinder

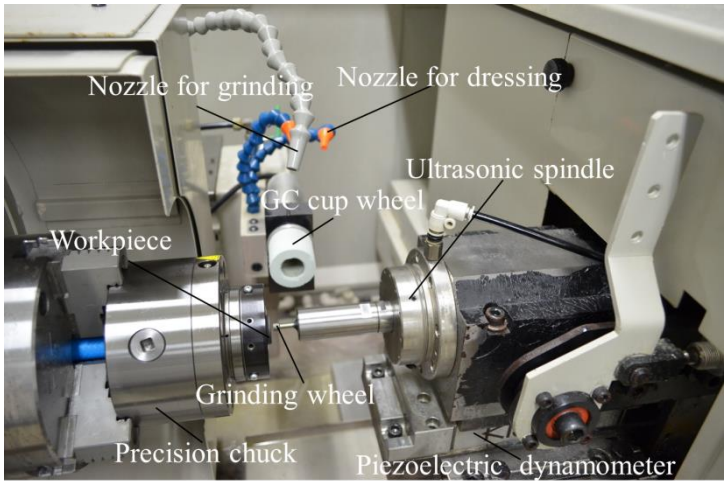

(b) Experimental setup detail

Fig. 2.7 Experimental setup of UAIG

In order to realize the processing principle of UAIG in practice, an experimental rig (Fig. 2.7) was constructed by installing a commercially available ultrasonic spindle (URT40 by Takesho Co., Ltd.), of which a grinding wheel is added onto the end face, on a commercially available CNC internal grinder (GRIND-X IGM15EX by Okamoto Machine Tool Works Co., Ltd., Fig. 2.7(a)) attached with a GC cup wheel dresser. In addition, a 3-components piezoelectric dynamometer (9256A by Kistler Instrument Corporation) was inserted between the spindle and the worktable and used for the

measurement of grinding forces. The coolant was supplied with a system composed of a nozzle, a pump and a tank.

The workpiece infeed rate of V_c, rotational speed of n_w, and oscillation motion speed are controlled by internal grinder via the control panel. The specifications of internal grinder are shown in table 2.1.

Table 2.1 Specifications of internal grinder

Ultrasonic spindle	Frequency *f* (kHz)	40
	Applied voltage (%)	30～100
	Rotational speed (rpm)	0~8000
Work chuck	Method of support work	A trio of clicks
	Rotational speed (rpm)	100~850
Table feed	Minimum amount (μm)	0.1
	Feed speed (mm/min)	0.1~10000

2.3 Measurement of UV amplitude

Fig. 2.8 UV amplitude measurement method

Before UAIG tests, it is necessary to confirm the performance of the ultrasonic spindle. Fig. 2.8 shows the UV amplitude measurement method. Laser Doppler vibrometers (LV-1610 by Ono Sokki Co., Ltd.) was used for measuring the UV amplitude of the grinding wheel. Grinding wheel was screw into the end surface of

the UV spindle. Laser light strikes on the center of the end surface of the grinding wheel. Thus, the UV amplitude in the grinding wheel axial direction can be measured.

Table 2.2 Measured UV amplitude when applied voltage=30%

	SD270 P100M	SD400 P100M	SD600 P100M	SD1000 P100M	SD3000 P100M
Measured amplitude *A* (peak-valley) (μm)	1.8	1.9	1.8	1.8	2.0
Measured frequency *f* (kHz)	40.32	39.68	40.81	39.21	39.84

Table 2-3. Measured UV amplitude when applied voltage=60%

	SD270 P100M	SD400 P100M	SD600 P100M	SD1000 P100M	SD3000 P100M
Measured amplitude *A* (peak-valley) (μm)	2.9	3.1	2.8	2.8	3.2
Measured frequency *f* (kHz)	40.65	39.84	40.16	39.21	39.68

Table 2-4. Measured UV amplitude when applied voltage=100%

	SD270 P100M	SD400 P100M	SD600 P100M	SD1000 P100M	SD3000 P100M
Measured amplitude *A* (peak-valley) (μm)	4.2	4.4	4.0	4.1	3.9
Measured frequency *f* (kHz)	40.16	39.68	40.00	39.21	39.86

Table 2.2-2.3 show the measured UV amplitude when applied voltage=30%, 60%, and 100%, respectively. It is found that the UV amplitude increases with the increasing of applied voltage.

2.4 Experiment detail

Actual UAIG operations of SiC ceramic workpieces were conducted on the constructed rig under the processing parameters as shown in Table 2.2 to elucidate the grinding characteristics. There are 5 kinds of grinding wheel are used for UAIG tests, they are SD270 P100M, SD400P100M, SD600P100M, SD1000 P100M, and SD3000

P100M, respectively. Prior to the grinding operations, the truing/dressing of grinding wheel was performed with the GC cup wheel dresser. The cylindricity and roundness of the workpiece ground were measured using a roundness measuring instrument (Rondcom55A by Tokyo Seimitsu Co., Ltd). The surface roughness of the workpieces were evaluated with a surface profiler (Form Talysurf Intra by Taylor Hobson Inc.). The topographies of work-surface and grinding wheel, the chips and the subsurface damages were observed by using a SEM (ERA-8900S by Elionix Co., Ltd.).

Table 2.2 Processing parameters

Ultrasonic Vibration	Frequency f=40 kHz; Amplitude A=0, 4.0μm	
Grinding wheel	SD270 P100M, SD400P100M, SD600P100M, SD1000 P100M, SD3000 P100M.	
	Oscillation motion	Stroke: 8mm
		Speed: 0.1m/min
	Rotational speed n_g (r/min)	4000,5000, 6000
	Feed rate V_c (μm/min)	5, 10, 15, 20
	Stock removal (μm)	50
Workpiece	SiC ceramics ϕ12 (inner)×ϕ22 (outer)×t13 mm	
	Rotational speed n_w (r/min)	100, 200, 300
Coolant	Solution type, 1.6% dilution	

2.5 Summary

This chapter details the related experiment rig that was employed in this study. The principal of UAIG is in the foremost place and followed by the introduction of UAIG experimental rig. After that, the UV amplitude was measured. The UV amplitude basically scales with regard to applied voltage. At last, experimental condition, under which the experiments were performed, was listed. All those are described in the chapter is preparatory but fundamental work for the following chapter.

Chapter 3 Machining characteristics of ultrasonic assisted internal grinding of SiC ceramics

In this chapter, investigations on the machining characteristics of SiC ceramics workpiece were performed on the constructed rig. CIG tests involving the same workpiece were also carried out on the same experimental rig for comparison. The effects of the UV on the grinding forces, the surface roughness and the form accuracy, i.e., roundness and cylindricity, were revealed. Meanwhile, the topographic features of work-surfaces and the subsurface damages were observed as well to clarify the material removal behavior. In addition, considering that grinding efficiency and work-surface quality are, to some extent, determined by grinding wheel performance [1-3], the grinding wheel wear was also experimentally studied.

3.1 Experiment conditions

Table 3.1 Processing parameters

Ultrasonic Vibration	Frequency f=40 kHz; Amplitude A=0, 4.0μm	
Grinding wheel	SD400P100M ϕ6×t5 mm	
	Oscillation motion	Stroke: 8mm
		Speed: 0.1m/min
	Rotational speed n_g (r/min)	4000
	Feed rate V_c (μm/min)	5, 10, 15, 20
	Stock removal (μm)	50
Workpiece	SiC ceramics ϕ12 (inner)×ϕ22 (outer)×t13 mm	
	Rotational speed n_w (r/min)	300
Coolant	Solution type, 1.6% dilution	

Actual UAIG operations of SiC ceramic workpieces were conducted on the constructed rig under the processing parameters as shown in Table 3.1 to elucidate the fundamental grinding characteristics. Prior to the grinding operations, the truing/dressing of grinding wheel was performed with the GC cup wheel dresser.

3.2 Grinding forces

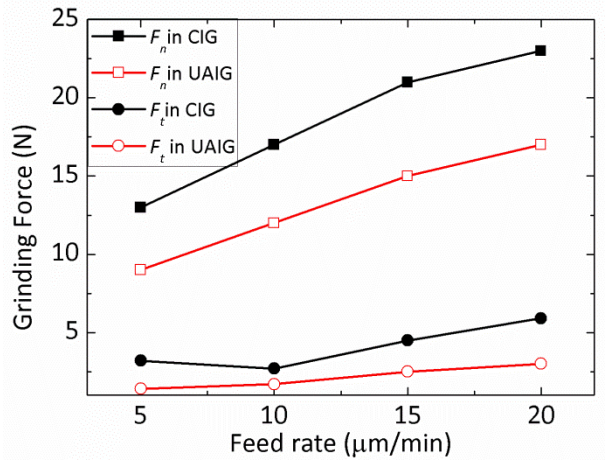

Fig. 3.1 Grinding forces vs. feed rate V_c in CIG and UAIG

The effect of the feed rate V_c on the grinding forces in CIG and UAIG are shown in Fig. 3.1. It can be figured out that both the normal force F_n and the tangential force F_t either in CIG or in UAIG increase monotonously with the increasing of the feed rate V_c. It is in particular interesting to note that either the F_n or the F_t in UAIG are much smaller than those in CIG; concretely, the F_n and the F_t in UAIG are smaller by 30.7% and 56.25% at V_c=5μm/min, 29.4% and 37.0% at V_c=10μm/min, 28.6% and 44.4% at V_c=15μm/min, and 26.0% and 49.1% at V_c=20μm/min, respectively, than those in CIG. This is the valuable information for the application of UAIG technique to the internal grinding of SiC ceramics. The grinding force reduction mechanism will be discussed in chapter 4.

3.2 Form accuracy and surface roughness

Fig. 3.2 shows the comparison of the workpiece form accuracy, i.e., roundness E_r and cylindricity E_c, before and after CIG and UAIG at V_c=10μm/min (other parameters were as in table 1). It can be found from the figure that the roundness E_r in CIG is decreased from the initial value of E_r=4.6μm to the final one of E_r=1.5μm by 67.4% whereas in UAIG from E_r=5μm to E_r=0.7μm by 86%, indicating that the better roundness can be attained by UAIG and the improvement of roundness is greater compared with those in CIG. Shifting the attention to the cylindricity E_c, it is figured out that not only the final value of E_c =1.4μm in UAIG is much smaller than that of E_c=4.4μm in CIG but also the decrease rate of E_c in UAIG is significantly larger than that in CIG, i.e., 86% in UAIG against 56% in CIG. The surface roughness R_a in UAIG is also compared with that in CIG at V_c=10μm/min as shown in Fig. 3.3. Obviously, the value of R_a after UAIG is smaller than that after CIG; concretely, the surface roughness R_a in CIG is decreased from the initial value of 149nm to 35nm, i.e., a 76.5% decrease, whereas in UAIG from 146nm to 22nm, i.e., a 84.9% decrease, meaning that the surface quality improvement in UAIG is greater compared with that in CIG. The improvement of form accuracy and surface quality in UAIG can be considered to be the contribution of the grinding forces reduction owing to the presence of the UV [4].

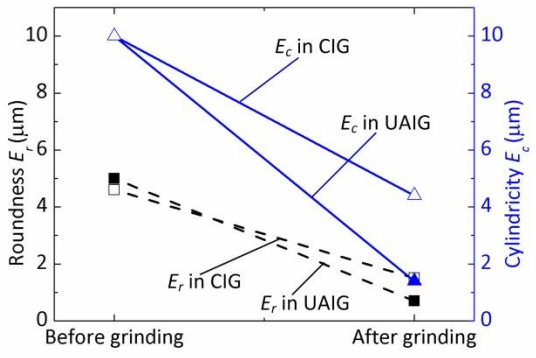

Fig. 3.2 Form accuracy in CIG and UAIG

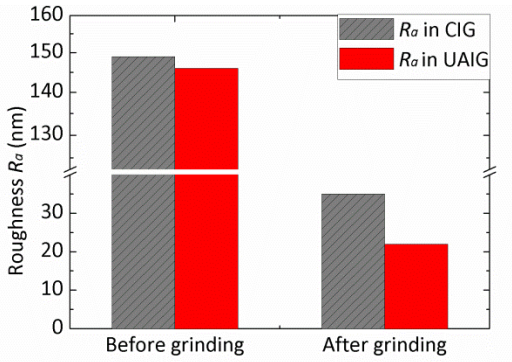

Fig. 3.3 Surface roughness in CIG and UAIG

3.4 Work-surface integrity

To further investigate the work-surface integrity and explore the improvement mechanism of work-surface quality, the topographic features of the work-surfaces finished by CIG and UIAG were observed with SEM. Figs. 3.4 and 3.5 exhibit the SEM images of the work-surfaces achieved in CIG and UAIG, respectively, at f= 40kHz, A=4μm, SD400P100M, n_g= 4000rpm, and V_c=10μm/min. As shown in Fig. 3.4(a), the grinding marks in CIG can be distinctly seen along the grinding direction, and many grinding cracks are also observed on the same surface (Fig. 3.4(b)). By contrast, both the grinding marks and the grinding cracks are hardly observed on the work-surface finished by UAIG (Fig. 3.5).

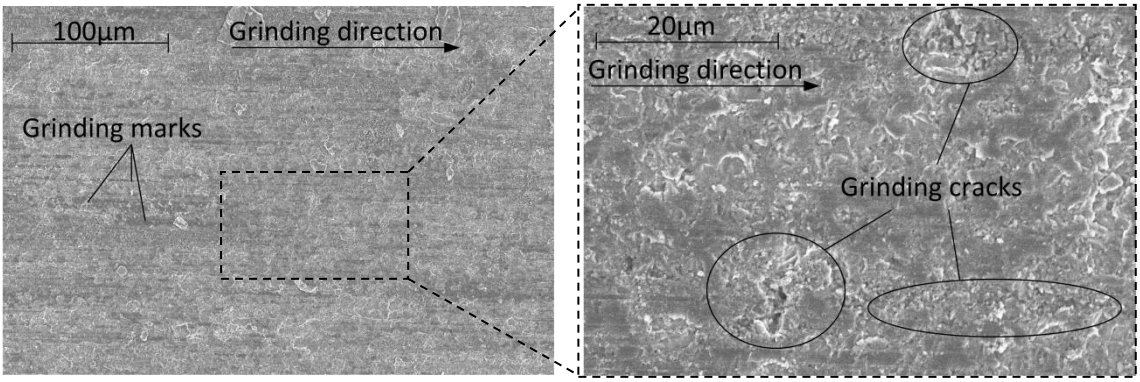

(a) Morphology of work-surface (b) Enlarged view of work-surface

Fig. 3.4 SEM images of work-surface by CIG

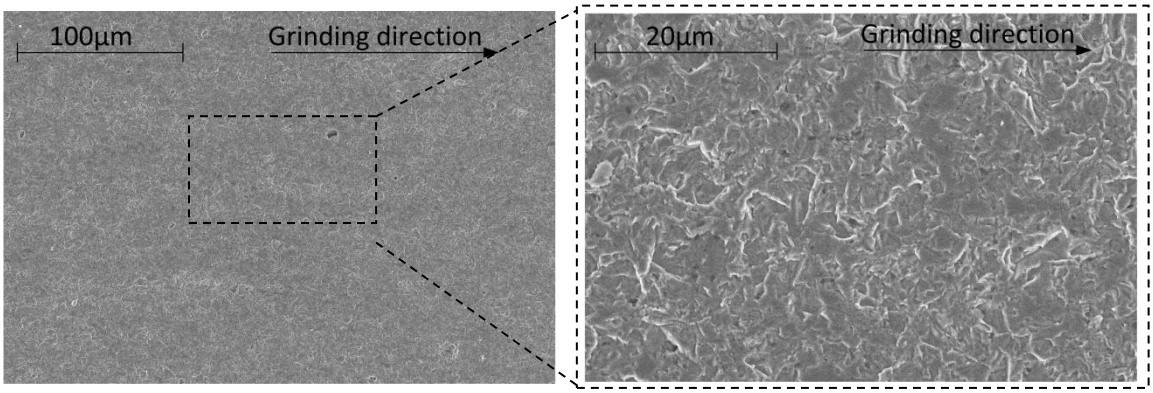

(a) Morphology of work-surface (b) Enlarged view of work-surface

Fig. 3.5 SEM images of work-surface by UAIG

Normally, the macroscopic results from the grinding process are composed of microscopic effects of individual abrasive grains engaging in cutting actions [5]. The grain-workpiece interactions in CIG and UAIG are schematically given in Figs. 3.6(a) and (b), respectively. In UAIG, the UV is added on the grinding wheel, and the abrasive grain on the grinding wheel will engage in a sinusoid movement. By contrast, the cutting direction of the abrasive grain is always along grinding speed direction in CIG as shown in Fig. 3.6(a). Therefore, the reason why grinding marks are hardly generated in UAIG is that the paths of different grains are interworked to form a knitted wool structure in the work-surface due to sinusoidal grain motion path (Fig. 3.6(b)), leading to the higher surface quality. In addition, the reason why grinding cracks almost did not occur in UAIG is probably that the normal grinding force in UAIG is significantly lower compared with that in CIG [6].

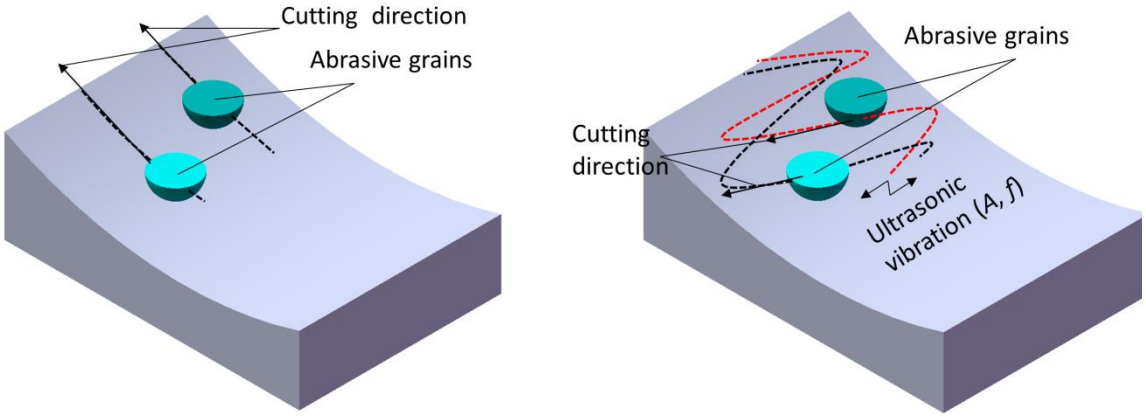

(a) CIG (b) UAIG

Fig. 3.6 Schematic illustration of grain-workpiece interaction in CIG and UAIG

3.5 Grinding wheel wear

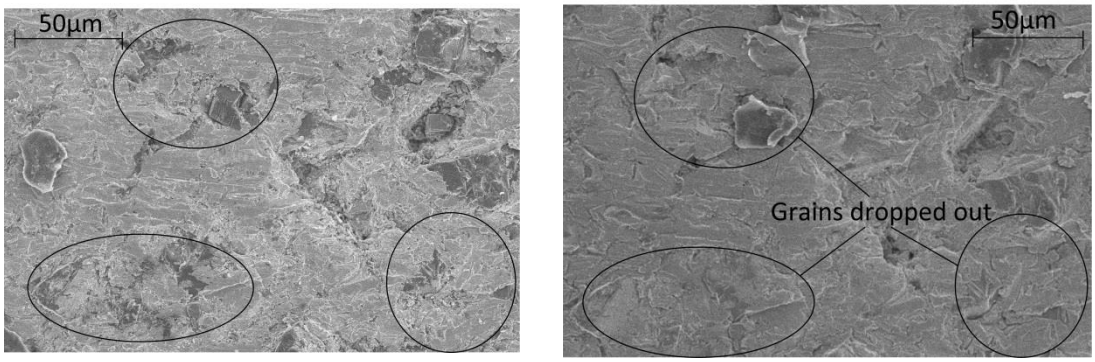

(a) Grinding wheel topographic features after truing/dressing

(b) Grinding wheel topographic features after CIG

Fig. 3.7 SEM images of grinding wheel topographic features after truing and after CIG

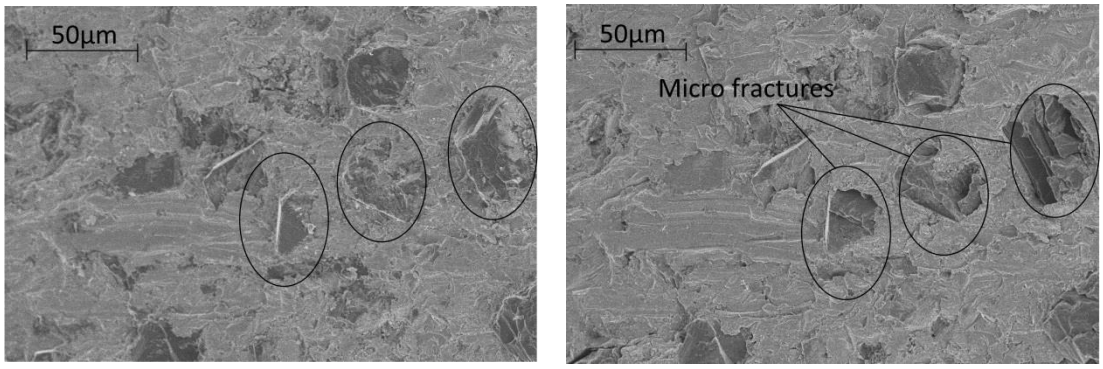

(a) Grinding wheel topographic features after truing/dressing

(b) Grinding wheel topographic features after UAIG

Fig. 3.8 SEM images of grinding wheel topographic features after turing/dressing and after UAIG

To investigate the grinding wheel wear in CIG and UAIG, the SEM observation of grinding wheel topographic features were carried out. Figs. 3.7(a) and (b) present the SEM images of the grinding wheel after truing/dressing and after CIG at f= 40kHz, A=4μm, SD400P100M, n_g= 4000rpm, and V_c=10μm/min, respectively. Most cutting edges disappear after the CIG even if abundant cutting edges are created after

dressing/truing. This suggests that the active abrasive grains drop out dramatically during CIG. By contrast, most of the cutting edges remain on the wheel working surface well even after UAIG (Compare Fig. 3.8(a) with Fig. 3.8(b)). The densities of cutting edges C_s on the wheel working surfaces after truing/dressing and after CIG and UAIG are compared in Fig. 3.9. It can be seen that although either in CIG or in UAIG, the C_s decreases, the decrease rate of 37.7% in CIG is much higher than that of 13.3% in UAIG.

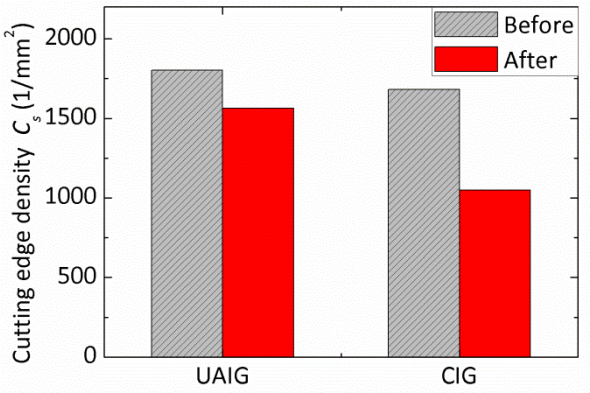

Fig. 3.9 Abrasive grain cutting edge density in CIG and UAIG

Comparing the topographic feature of the grinding wheel working surface in CIG (Fig. 3.7) with that in UAIG (Fig. 3.8) reveals that the wheel wear in CIG is caused dominantly by the pullout of grains whilst in UAIG mainly by the micro-fracture as well as the slight grain pullout. Liang et al. [7] reported that the grain pullout and fracture hardly occured in UAG for the sake of the low grinding force, whereas in CG the severe fracture and pullout of grains occured due to the larger grinding forces. This suggests that compared with CIG the grinding forces in UAIG is smaller and thus most of the cutting edges remain on the wheel working surface well, resulting in higher cutting edge density in UAIG. The higher cutting edge density has a positive effect on the improvement of surface roughness.

3.6 Subsurface damage

In most cases, the ground ceramics suffers strength degradation from the machining-induced subsurface damage [8]. Thus, in order to assess the subsurface damage, the end faces of two workpieces were carefully polished so that the defects, e.g., cracks and fractures, on the initial end face no longer exist on the final end faces after polishing, and then one of the polished workpiece was ground by CIG and the other by UAIG at f= 40kHz, A=4μm, SD400P100M, ng= 4000rpm, and V_c=20μm/min and stock removal=200μm, followed by the SEM observation of the end faces.

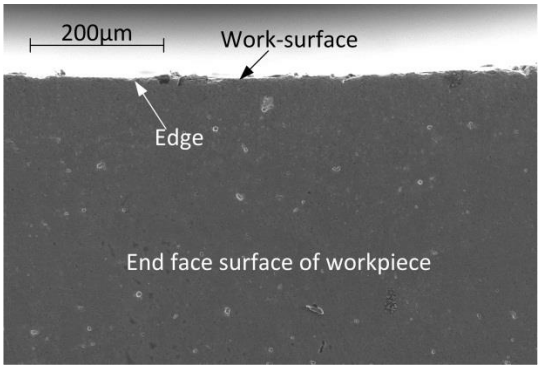

(a) Workpiece end face after polishing

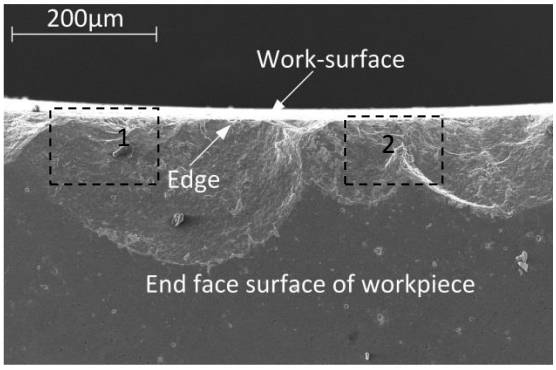

(b) The workpiece end face after CIG

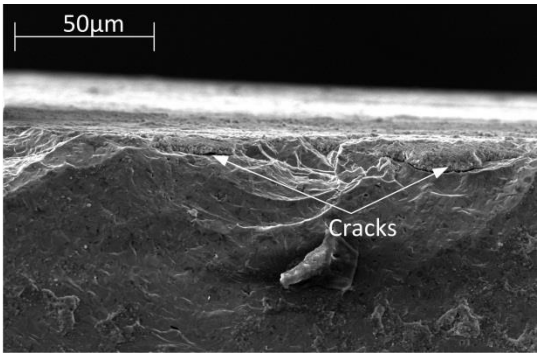

(c) Enlarged view of area 1

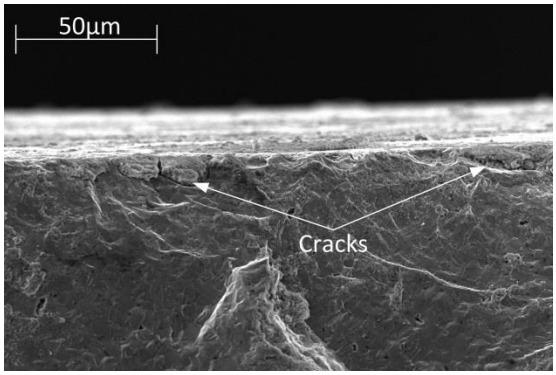

(d) Enlarged view of area 2

Fig. 3.10 SEM images of the workpiece end face after polishing and CIG

Figs. 3.10(a) and (b) show the SEM images of the workpiece end face after polishing and after CIG, respectively; the enlarged views of the areas 1 and 2 (Fig. 3.10(b)) are as in Figs. 3.10(c) and (d), respectively. It is obvious from the comparison of Figs.

3.10(a) and (b) that continuous brittle fractures occur along the edge on the end face, and the depth of the deepest facture reaches 201μm after CIG. It is also found from Figs. 3.10(c) and (d) that there are micro-cracks underneath the work-surface. By contrast, as shown in Fig. 3.11, similar to that in CIG, the brittle fractures occur along the edge on the end face as well in UAIG, however, the fractures are not continuous, and the depth of the deepest facture is measured to be 167μm, a value which is smaller by 17% than that in CIG (Fig. 3.11(b)). In addition, it is found from Figs. 3.11(c) and (d) that no micro-cracks can be observed underneath the work-surface in UAIG.

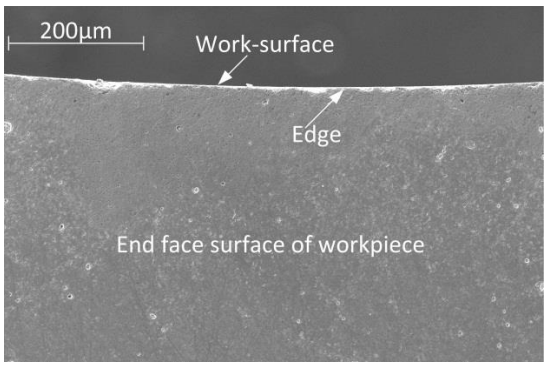

(a) Workpiece end face after polishing

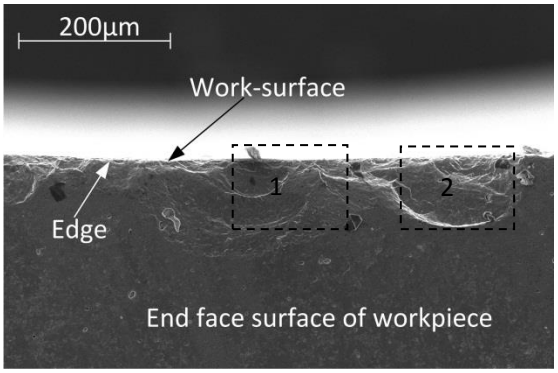

(b) The workpiece end face after UAIG

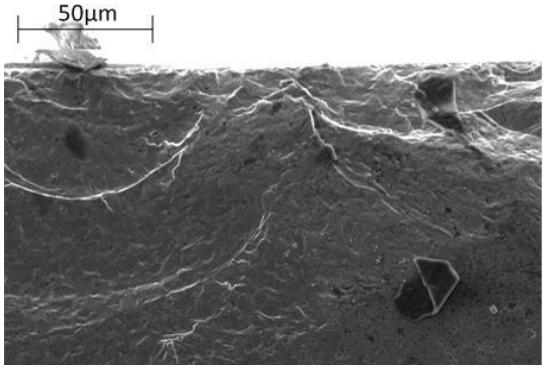

(c) Enlarged view of area 1

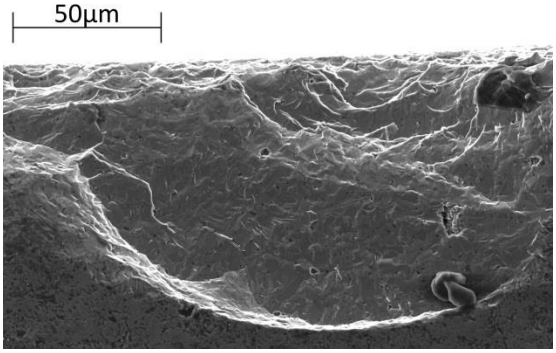

(d) Enlarged view of area 2

Fig. 3.11 SEM images of the workpiece end face after polishing and UAIG

Previous study found that the cracks generation strongly depended on the normal force level [9]. The main reason why the damage is alleviated in UAIG is attributed to the reduction of the grinding force as mentioned in section 3.1. Furthermore, the hardness of the work-surfaces after CIG and UAIG were measured with a micro

hardness tester (HM124 VALPAK2000 by Akashi Co., Ltd) as shown in Fig. 3.12. It is evident that the work-surface obtained by UAIG is harder than that by CIG. Previous study found that increased hardness can effectively restrain the presence and growth of cracks [10]. This can be considered as the other factor leading to the alleviation of subsurface damage in UAIG.

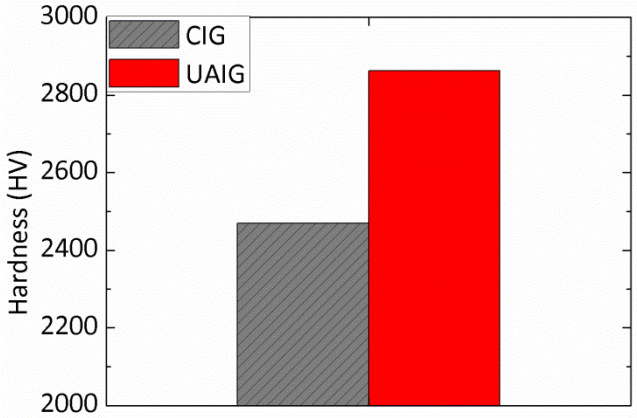

Fig. 3.12 Vickers hardness of the workpieces ground by UAIG and CIG

3.7 Summary

In the present work, an ultrasonic assisted internal grinding technique was proposed for the internal grinding of SiC ceramics and the fundamental machining characteristics were experimentally elucidated. The following conclusions can be drawn:

(1) The normal and tangential grinding force in UAIG are significantly reduced compared with those in CIG. This is the valuable information for the application of UAIG technique to the internal grinding of SiC ceramics.

(2) The greater improvement of the form accuracy are achieved in UAIG compared with those in CIG, i.e., in CIG, the roundness and cylindricity of workpiece are improved by 67.4% and 56%, respectively, after grinding, whereas in UAIG by 86% for both the roundness and cylindricity;

(3) The roughness R_a in UAIG are significantly smaller than those in CIG, meaning the presence of the UV improves the surface roughness significantly. Furthermore, the grinding marks and the grinding cracks occurring on the work-surface can be restrained considerably by the presence of the UV.

(4) Abrasive grain protrusions are observed sufficiently in UAIG. The pullout of grain is considered as the main wheel wear mechanism in CIG while the micro-fracture as well as the slight grain pullout are the dominant mechanisms in UAIG.

(5) Observation of subsurface damage shows the fracture depth is decreased by 17% and cracks are alleviated, owing to the reduction of force and the increase of the hardness of the ground workpiece in UAIG.

Reference

[1] Hassui, A. ; Diniz, A. E. ; Oliveira, J. F. G. ; Felipe, J. ; Gomes, J. J. F. Experimental evaluation on grinding wheel wear through vibration and acoustic emission. *Wear* **1998**, *217* (1), 7-14.

[2] Gopal, A. V. ; Rao, P. V. Modeling of grinding of silicon carbide with diamond wheels. *Mineral Processing and Extractive Metallurgy Review* **2002**, *23* (1), 51-63.

[3] Zhong, Z. Grinding of Toroidal and Cylindrical Surfaces on SiC Using Diamond Grinding Wheels. *Materials and Manufacturing Processes* **1997**, *12* (6), 1049-1062.

[4] Fujimoto, M. ; Wu, Y. ; Cao, J., High Precision Ultrasonically Assisted Internal Grinding (UAIG) of Difficult-to-machining Materials using Metal Bonded Diamond Wheels, in: The 6th International Conference on Leading Edge Manufacturing in 21st Century, 2011.

[5] Anderson, D. ; Warkentin, A. ; Bauer, R. Experimental and numerical investigations of single abrasive-grain cutting. *International Journal of Machine Tools and Manufacture* **2011**, *51* (12), 898-910.

[6] Mult, H. ; Spur, G. ; Holl, S. Ultrasonic assisted grinding of ceramics. *Journal of Materials Processing Technology* **1996**, *62* (4), 287-293.

[7] Spur, G. ; Holl, S.-E. Ultrasonic assisted grinding of ceramics. *Journal of Materials Processing Technology* **1996**, *62* (4), 287-293.

[8] Malkin, S. ; Ritter, J. Grinding mechanisms and strength degradation for ceramics. *Journal of Engineering for Industry (Transactions of the ASME (American Society of Mechanical Engineers), Series B);(USA)* **1989**, *111* (2).

[9] Gua, W. ; Yao, Z. ; Liang, X. Material removal of optical glass BK7 during single and double scratch tests. *Wear* **2011**, *270* (3-4), 241-246.

[10] Zhang, C. ; Feng, P. ; Zhang, J. Ultrasonic vibration-assisted scratch-induced characteristics of C-plane sapphire with a spherical indenter. *International Journal of Machine Tools and Manufacture* **2013**, *64*, 38-48.

Chapter 4 Grinding force model and force reduction mechanism of UAIG of SiC ceramics

As grinding force plays an influential role in work-surface finish in grinding process, a model is necessary for optimizing input variables to achieve high product quality and productivity. However, to the best of our knowledge, there are few reports on modeling grinding force in ultrasonic assisted internal grinding (UAIG). In this chapter, a theoretical model is presented to predict the grinding force in UAIG of SiC ceramics. This model stems from undeformed chip length resulting from the relative motion between the grinding wheel and the workpiece. After analyzing the cutting action of an active individual grain, normal and tangential force models for the UAIG of SiC ceramics are developed. Using the developed model, the influence of many principal input variables, namely the workpiece rotational speed n_w, the wheel infeed rate V_c, the wheel rotational speed n_g, the UV amplitude A_u, and the oscillation frequency f_o, on grinding force is predicted.

4.1 Introduction

In general, the grinding force plays an important role in grinding process as it not only has a direct influence on the wheel wear, grinding accuracy, grinding temperature and surface integrity but also strongly affects the material removal mechanism [1]. As for the influence of the UV on the grinding force, until now many studies have been concentrated on discussing the grinding force in UAG, and several grinding force models have been developed for UAG. Nomura et al. [2] developed a grinding force model for UAG by analyzing the grinding wheel-workpiece contact length and discussing the underformed chip cross-sectional area. Shimada et al. [3] also developed a force model for UAG by discussing the underformed chip cross-sectional area after analyzing the relative velocity between the grain and the workpiece. Qin et al. [4] proposed a grinding force model for the UAG of titanium and subsequently revealed that the tool is not in continuous contact with the workpiece and the

interaction between a diamond grain and the workpiece is considered as a penetration process, followed by establishing the relationship between the grinding force and the input variables.

Although some grinding force models for UAG were established so far as mentioned above, no publication is available on grinding force model for UAIG. In this study, in order to help understanding the material removal mechanism and optimizing the input variables (the workpiece rotational speed n_w, the wheel infeed rate V_c, the wheel rotational speed n_g, the UV amplitude A_u and the oscillation frequency f_o, etc.) in the UAIG of SiC ceramics, a grinding force model to predict relations between grinding force and input variables is developed after analyzing the relative motion between the grinding wheel and the workpiece. In addition, expressions for the normal and tangential grinding forces in UAIG are established by analyzing the cutting process of an active individual abrasive grain participating in grinding. In this study, at first, the model development approach is described in details. Afterwards, using the developed model, influences of the input variables on the grinding force are predicted. Finally, predicted results are compared with experimentally obtained ones to confirm the validity of the developed model.

4.2 Model development approach

Table 4.1 Input variables in UAIG process

Grinding wheel variables	Workpiece variables	UV variables	Grinding process parameters
Wheel width, b Wheel radius, R_g Wheel rotational speed, n_g	Workpiece radius, R_w Workpiece rotational speed, n_g	Amplitude, A_u Frequency, f_u	Infeed rate, V_c Depth of cut, a_e Oscillation stroke A_o Oscillation frequency f_o

As a combination of grinding and UV, there are a number of input variables in UAIG process as shown in Table 4.1. Usually, the macroscopic results are composed of the microscopic effects, especially, the cutting action in grinding is the summation

of the microscopic effects of all individual abrasive grains. Many grinding force models were established for surface grinding by analyzing an active individual abrasive grain that participates in cutting and summing up the effects of all active abrasive particles [5, 6]. A similar approach is also used in the present work to develop the force model for UAIG. As shown in Fig. 4.1, the model development steps are as following:

(1) Establish a relationship between input variables and undeformed chip cross-sectional area A_{cs}.

(2) Calculate the undeformed chip length $L_{c\text{-}UAIG}$ by considering the relative motion between the grinding wheel and the workpiece in UAIG.

(3) Analyze the cutting process of an active individual abrasive grain participating in grinding action and establish the tangential force and normal force model, f_t and f_n, for an individual abrasive grain.

(4) Establish the grinding force model, i.e., the tangential force and normal force model, $F_{n\text{-}UAIG}$ and $F_{t\text{-}UAIG}$, for UAIG process by aggregating the effects of all active abrasive grains.

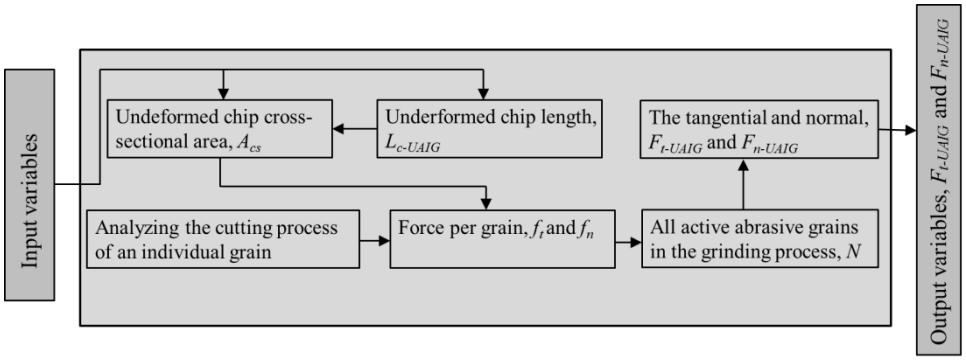

Fig. 4.1 Development process of the grinding force model for UAIG.

4. 3 Model development details

The complete description of grinding process is very difficult due to the complex cutting behavior of abrasive grains. Thus, prior to developing the model in details the major assumptions and simplifications are given as following:

(1) All abrasive grains on grinding wheel are rigid.

(2) Abrasive grains located on the grinding wheel surface have the same height, and all of them take part in cutting in the grinding process.

(3) Elastic/heat deflection between the grinding wheel and the workpiece and uneven distribution of the grains on the peripheral surface of the wheel are ignored.

4.3.1 Undeformed chip cross-sectional area

In grinding, the total volume of the chips formed per unit time, V_{chip}, is the ensemble of the volumes formed by all individual active grains in the grinding zone per unit time. Consequently, the V_{chip} can be calculated from the average cross-sectional area A_{cs} and length L_c of the undeformed chip and the number of active cutting grains in the grinding zone per unit time N_d as following:

$$V_{chip} = N_d A_{cs} L_c \tag{1}$$

Letting the active cutting edge density, the grinding width and the grinding wheel peripheral speed be c_d, b and V_g, respectively, gives

$$N_d = c_d b V_g . \tag{2}$$

On the other hand, the removed material per unit time, W_m, by the wheel can be written as:

$$W_m = 2\pi a_e R_w b n_w \tag{3}$$

where a_e, R_w, n_w are the wheel depth of cut, the workpiece internal radius and the workpiece rotational speed, respectively.

In internal grinding, the V_{chip} is supposed to be equal to the W_{m}, resulting in a relationship as expressed below:

$$N_d A_{cs} L_c = 2\pi a_e R_w b n_w \tag{4}$$

Substituting Eq. (2) into Eq. (4) followed by rearranging yields the average undeformed chip cross-sectional area A_{cs} as below:

$$A_{cs} = 2\pi a_e R_w n_w / c_d V_g L_c = a_e R_w n_w / c_d R_g n_g L_c \tag{5}$$

where R_{g} and n_g are the radius and rotational speed of the grinding wheel, respectively.

4.3.2 The undeformed chip length

Fig. 4.2 shows the geometrical arrangement between the grinding wheel and the workpiece and the relative motion of the grinding wheel to the workpiece during UAIG. The symbols a, R_{w0} stand for the distance between the centers of the workpiece and the grinding wheel at grinding start point and the initial radius of workpiece before grinding, respectively. Let a xyz-coordinate system be fixed on the workpiece; the x-axis is along the grinding wheel infeed direction, the y-axis is perpendicular to the wheel infeed direction, and the z-axis is along the workpiece axis. The origin point o is fixed at the center of the workpiece. It can be seen from the figure that in the UAIG, the grinding wheel has five different relative motions to the workpiece, i.e., a infeed motion in x-axis at the infeed rate of V_c, a rotation around its own axis at the speed of n_g, a revolution motion around z-axis at the speed of n_w, an UV in z-axis at the frequency of f_u and the amplitude of A_u, and an oscillation in z-axis at the frequency of f_o and the stroke of A_o. It can be figured out that owing to the spiral relative motion of the wheel to the workpiece caused by the simultaneous presence of the wheel infeed motion and the workpiece rotation motion (i.e., the wheel revolution motion around z-axis), the profile of the workpiece internal surface would be shaped to be spiral as shown in Fig. 4.2(a).

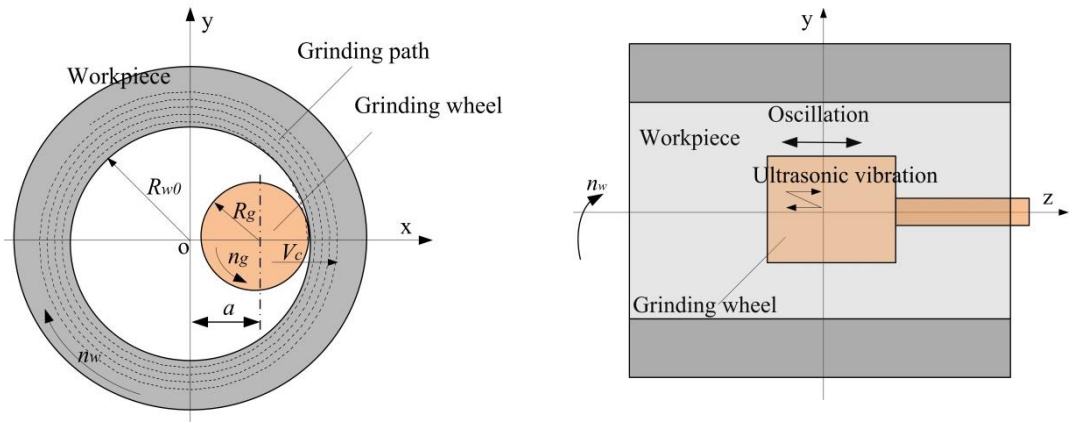

(a) yz-plane (b) xy-plane

Fig. 4.2 Geometrical arrangement between grinding wheel and workpiece.

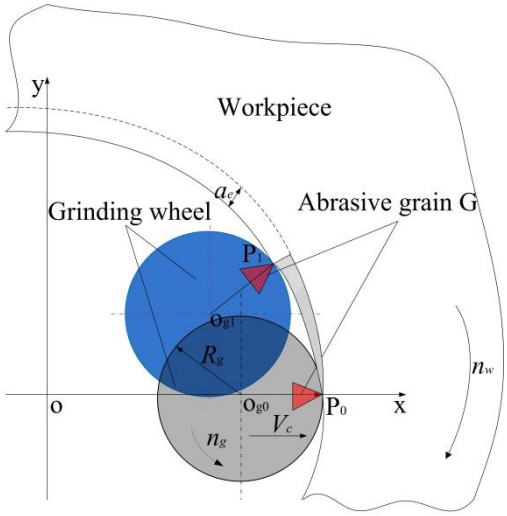

Fig. 4.3 Relative motion between the grinding wheel and the workpiece.

Under the presence of the five relative motions, the instantaneous geometrical relationship between the workpiece and the grinding wheel at grinding time t_0, i.e., after grinding for time t_0 is supposed to be as shown in Fig. 4.3. At this moment, the *xy*-coordinates of the grinding wheel center o_{g0} are $x_0=a+V_ct_0$, $y_0=0$. Then after the grinding is further performed for time Δt ($=t_1-t_0$), the grinding wheel center moves to point o_{g1} at time t_1 and its *xy*-coordinates at this moment become $x_1=a+V_ct_1-(a+V_ct_0)\cos(2\pi n_w(t_1-t_0))$, $y_1=(a+V_ct_0)\sin(2\pi n_w(t_1-t_0))$, resulting in an equation expressing the wheel circumference profile at time t_1 as follow.

$$[x-a-V_ct_1+(a+V_ct_0)\cos(2\pi n_w(t_1-t_0))]^2+[y-(a+V_ct_0)\sin(2\pi n_w(t_1-t_0)]^2=R_g^2 \quad (6)$$

In the meantime, the spiral work internal surface can be expressed with following equation.

$$\begin{aligned} x&=R_w(t)\cos(2\pi n_w t)\\ y&=R_w(t)\sin(2\pi n_w t)\end{aligned} \quad (7)$$

where $R_w(t)=R_{w0}+V_ct$.

By replacing time *t* in Eq. (7) with time t_1 and substituting Eq. (7) into Eq. (6), the Eq. (6) can be rewritten as:

$$[(R_{w0}+V_ct_1)\cos(2\pi n_wt_1)-a-V_ct_1+(a+V_ct_0)\cos(2\pi n_w(t_1-t_0))]^2+[(R_{w0}+V_ct_1)\sin(2\pi n_wt_1)-(a+V_ct_0)\sin(2\pi n_w(t_1-t_0)]^2=R_g^2 \quad (8)$$

Subsequently the value of $\Delta t=t_1-t_0$ that is the time period during which the abrasive grain G takes part in the cutting action at point P_0 at time t_0 and gets out of the action

at point P_1 at time t_1 (Fig. 4.3) can be obtained from Eq. (8) once the input variables a, R_{w0}, n_w, n_g, V_c, A_u, f_u, A_o, f_o, and t_0 have already been determined. For instance, at a=3mm, R_{w0}=6mm, n_w=300rpm, n_g=4000rpm, V_c=10μm/min, A_u=4μm, f_u=40kHz, A_o=4mm, f_o=0.625Hz and t_0=75s, the value of t_1 can be obtained to be 75.0057s by solving the Eq. (8) in numerical calculation technique using a commercial software, Matlab; subsequently, $\Delta t=t_1-t_0$=0.0057s.

As the abrasive grain G is at the point P_0 ($x=a+R_g+V_ct_0$, $y=0$, $z=0$) at time t_0 when it takes part in the cutting action, then at time t ($t_0 \le t \le t_1$) its coordinates are obtained as Eq. (9) from the geometrical relationship shown in Fig. 4.3.

$$\begin{cases} x = a + V_c t + R_g \cos(2\pi n_g (t - t_0)) \\ y = (a + V_c t)\cos(2\pi n_w (t - t_0)) + R_g \sin(2\pi n_g (t - t_0)) \\ z = A_u \sin(2\pi f_u (t - t_0)) + A_o \sin(2\pi f_o (t - t_0)) \end{cases} \tag{9}$$

Differentiating Eq. (9) with respect to t, gives

$$\begin{cases} dx = [V_c - 2\pi R_g n_g \sin(2\pi n_g (t - t_0))]dt \\ dy = V_c \cos(2\pi n_w (t - t_0)) - 2\pi n_w (a + V_c t)\sin(2\pi n_w (t - t_0)) + 2\pi n_g R_g \cos(2\pi n_g (t - t_0)) \\ dz = 2\pi [A_u f_u \cos(2\pi f_u (t - t_0)) + A_o f_o \cos(2\pi f_o (t - t_0))]dt \end{cases} \tag{10}$$

Subsequently, the undeformed chip length in UAIG $L_{c\text{-}UAIG}$ can be determined by the following equation.

$$\begin{aligned} L_{c-UAIG} &= \int_{t_0}^{t_0+\Delta t} \sqrt{dx^2 + dy^2 + dz^2}\, dt \\ &= \int_{t_0}^{t_0+\Delta t} \sqrt{\begin{aligned} &\left[V_c - 2\pi R_g n_g \sin(2\pi n_g (t - t_0))\right]^2 \\ &+ \left[V_c \cos(2\pi n_w (t - t_0)) - 2\pi n_w (a + V_c t)\sin(2\pi n_w (t - t_0)) + 2\pi n_g R_g \cos(2\pi n_g (t - t_0))\right]^2 \\ &+ 4\pi^2 \left[A_u f_u \cos(2\pi f_u (t - t_0)) + A_o f_o \cos(2\pi f_o (t - t_0))\right]^2 \end{aligned}} dt \end{aligned} \tag{11}$$

The CIG process can be considered as a special case of UAIG process when A_u=0. Thus, the undeformed chip length in CIG $L_{c\text{-}CIG}$ can be obtained by substituting A_u=0 into Eq. (11).

4.3.3 The force model

Fig. 4.4(a) shows a simplified cutting force model for a single abrasive grain in UAIG. According to [6], the tangential and normal cutting forces, f_t and f_n, acting on the grain can be determined as the function of the undeformed chip cross-sectional

area A_{cs}, i.e.,

$$f_n = kA_{cs} \tag{12}$$

$$f_t = k_1 kA_{cs} \tag{13}$$

Where k is the chip thickness coefficient, and k_1 is the ratio of the tangential force to the normal force.

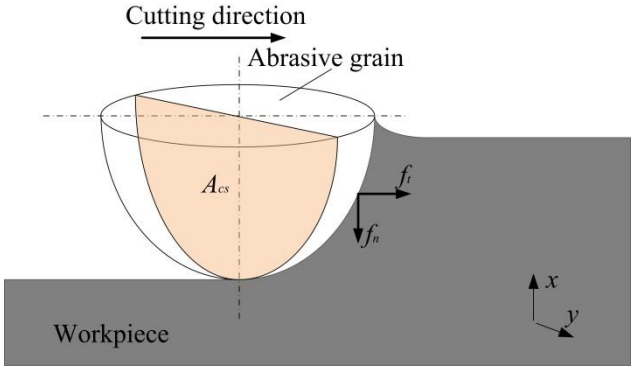

(a) Forces on the grain

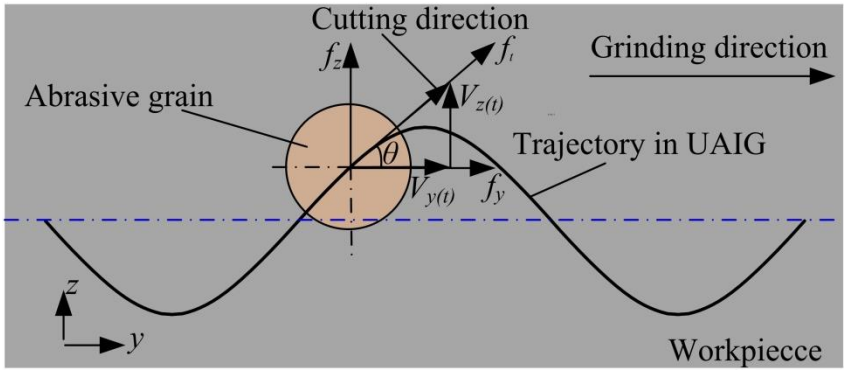

(b) Cutting trace and force direction variation

Fig. 4.4 Simplified cutting force model for a single abrasive grain in UAIG.

As the ultrasonic vibration period is extremely small compared with the oscillation period, sinusoidal cutting traces of abrasive grains can be hence approximately generated on the work-surface in UAIG as shown in Fig. 4.4(b). This means that the direction of the tangential force f_t varies in a sinusoidal pattern and the f_t can be separated into two components along y- and z-axes, respectively, i.e., f_y and f_z (Fig. 4.4(b)), as following:

$$\begin{cases} f_y = f_t \cos\theta \\ f_z = f_t \sin\theta \end{cases} \tag{14}$$

where θ is the engagement angle and given by:

$$\theta = \tan^{-1}(V_z(t)/V_y(t)) = \tan^{-1}(dz/dy) \tag{15}$$

where $V_y(t)$ and $V_z(t)$ are velocities in y- and z-axes, respectively, which can be obtained by Eq. (10). Subsequently the θ can be determined by substituting Eq. (10) into Eq. (15). For instance, under the input variables of n_w=300rpm, n_g=4000rpm, V_c=10μm/min, A_u=4μm, f_u=40kHz, A_o=4mm, f_o=0.625Hz, and in one UV period, the θ would be in the range of [-50.2 °, 50.2 °] according to Eq. (15).

It is deduced from Eqs. (14) and (15) that the force f_z periodically changes in z-direction within the certain range of θ, resulting in the mean force f_z in one UV period being almost zero. Therefore, hereafter only the forces in x- and y-directions, i.e., tangential and normal forces, are considered.

As mentioned above, the forces in x- and y-directions are fluctuating periodically. It is helpful for dealing with the fluctuating forces to introduce the average value of the fluctuating one. In addition, the resultant grinding forces acting on the grinding wheel are the sum of the forces acting on all active grains within the grinding zone. Following the calculation method of the average force [7], the average value of the normal force and the tangential force, $F_{n\text{-}UAIG}$ and $F_{t\text{-}UAIG}$, during the time period Δt(= t_1-t_0) in UAIG, can be written as:

$$\begin{cases} F_{t-UAIG} = N\dfrac{1}{\Delta t}\displaystyle\int_{t_0}^{t_0+\Delta t} f_y dt = Nk_1 kA_{cs}\dfrac{1}{\Delta t}\int_{t_0}^{t_0+\Delta t}\cos\theta dt \\ F_{n-UAIG} = N\dfrac{1}{\Delta t}\displaystyle\int_{t_0}^{t_0+\Delta t} f_x dt = NkA_{cs} \end{cases} \tag{16}$$

where N is the total number of active cutting edges in grinding zone and can be obtained with Eq. (17) [1]:

$$N = c_d b l_c \tag{17}$$

where l_c is the grinding wheel-workpiece contact length which can be determined with Eq. (18) ([6]):

$$l_c = \sqrt{\frac{2R_g a_e}{1 - R_g / R_w(t)}} \tag{18}$$

By substituting Eqs. (5), (12-15), (17), (18) into Eq. (16), the normal force and the tangential force, $F_{n\text{-}UAIG}$ and $F_{t\text{-}UAIG}$, at time t_0, can be written as:

$$\begin{cases} F_{t-UAIG} = k_1 k \sqrt{\dfrac{2R_g a_e}{1-R_g/(R_{w0}+V_c t_0)}} \dfrac{b(R_{w0}+V_c t_0)a_e n_w}{R_g n_g L_{c-UAIG}} \dfrac{1}{\Delta t}\int_{t_0}^{t_0+\Delta t} \cos\theta dt \\ F_{n-UAIG} = k \sqrt{\dfrac{2R_g a_e}{1-R_g/(R_{w0}+V_c t_0)}} \dfrac{b(R_{w0}+V_c t_0)a_e n_w}{R_g n_g L_{c-UAIG}} \end{cases} \tag{19}$$

where $L_{c\text{-}UAIG}$ can be obtained by Eq. (11). As mentioned above, the CIG process is a special case of UAIG process with A_u=0, hence θ=0 °. Thus, the tangential force $F_{t\text{-}CIG}$ and the normal force $F_{n\text{-}CIG}$ in CIG can be obtained by substituting A_u=0 and θ=0 into Eq. (19).

4.4. Grinding force reduction mechanism in UAIG

Table 4.2 Experiment condition

Ultrasonic Vibration	Frequency f=40 kHz; A=0μm, 2μm, 4μm	
Grinding wheel	SD400P100M,φ6×t5 mm	
	Oscillation motion	Stroke: 10mm
		Speed: 0.1m/min
	Feed rate V_c	10μm/min,
	Stock removal	25μm
	Rotational speed	4000rpm
Workpiece	Rotational speed	300rpm
	SiC ceramics φ12(inner)×φ22(outer)×t13 mm	
Coolant	Solution type, 1.6%dilution	

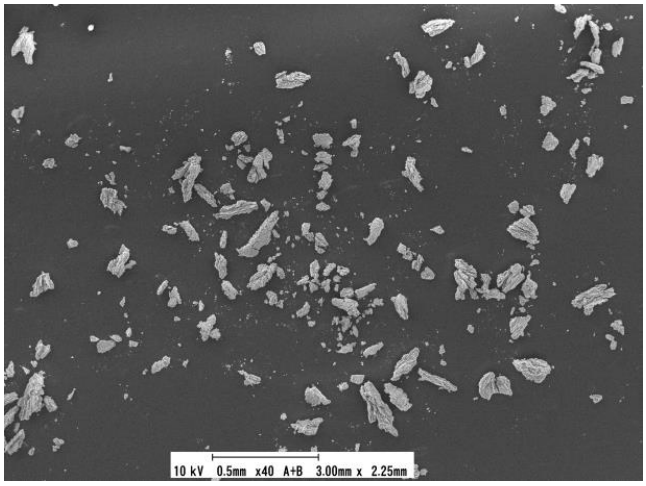

(a) A=0μm

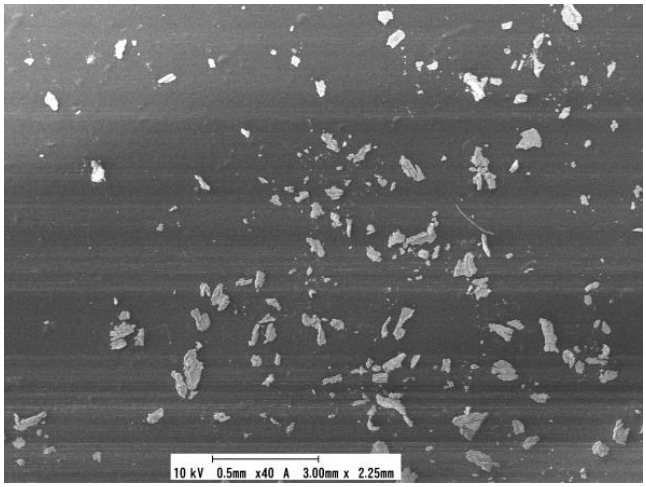

(b) A=2μm

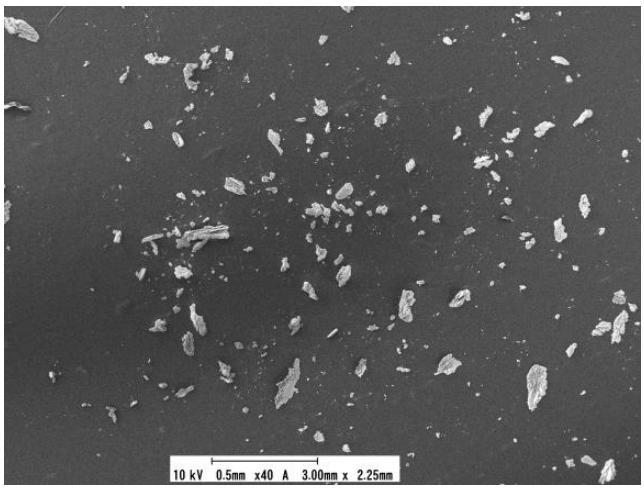

(c) *A*=4μm

Fig. 4.5 SEM images of chips formed in CIG and UAIG

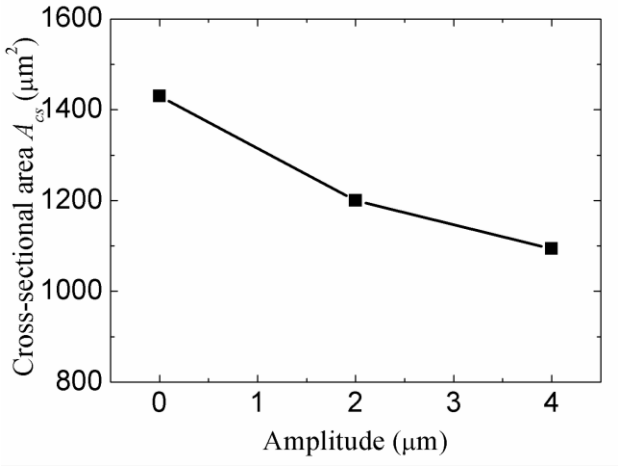

Fig. 4.6 Cross-scetional area A_{cs} vs. amplitude A

It is inferred from Eq. (16) that the larger cross-sectional area Acs is, the larger the grinding forces become. The reason why the grinding forces in UAIG are reduced compared to CIG may also be ascribed to the smaller chip cross-sectional area in UAIG compared with that in CIG. If this reason holds, the sizes of chip cross-sectional area formed in UAIG ought to be smaller than those in CIG. In order to confirm this issue, the chips formed both in CIG and in UAIG of SiC ceramics were gathered and examined by SEM under the condition as shown in Table 4.2. Fig. 4.5 shows the SEM images of chips formed in CIG and UAIG. Fig. 4.6 shows variation of the cross-sectional area of the chips formed in CIG and UAIG measured by 3D-SEM. It is found that the mean cross-sectional area of the chips decreases with the increasing of amplitude *A*. This phenomenon was also found under other grinding parameters. This means that the undeformed chip cross sectional area in UAIG is smaller than that in CIG, eventually confirming the above mentioned reason.

4.5 Grinding forces predictions and model verification

4.5.1 Experimental determination of parameters *k* and k_1

According to Eq. (19), it is essential to determine the actual values of the chip thickness coefficient, *k*, and the ratio of the tangential force to the normal force, k_1, to predict the grinding forces quantitatively. Although the *k* and k_1 are independent of the input variables and hence their values can be determined by only one round of grinding test under a certain set of input variables in principle, 5 rounds of grinding tests were performed under different sets of input variables as shown in Table 4.3 and the average of 5 data obtained either for the *k* or for the k_1 was adopted to indicate the *k* or the k_1 in order to avoid the deviation due to the input variables. In the current work, the other input variables are kept constant at f_u=40 kHz, A_o=4mm, f_o=0.625Hz, R_{w0}=6mm, R_g=3mm, a_e=0.1μm, *b*=5mm, and radial stock removal of 25μm.

Table 4.3 Experimental conditions for obtaining *k* and k_1

Test No.	n_g (rpm)	n_w (rpm)	A_u(μm)	V_c (μm/min)
1	4000	300	4	10
2	4000	200	4	10
3	5000	300	4	10
4	4000	300	3	10
5	4000	300	4	15

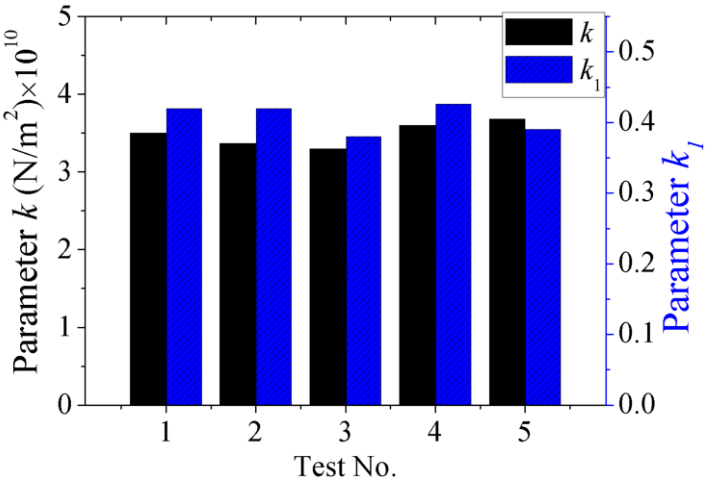

Fig. 4.7 Value of *k* and k_1 obtained in all of the tests

In each test, the corresponding grinding forces, $F_{n\text{-}UAIG}$ and $F_{t\text{-}UAIG}$, were obtained. Substituting the obtained values of $F_{n\text{-}UAIG}$ and $F_{t\text{-}UAIG}$ and all input variables (t_0 =75s) into Eq. (19) followed by re-ranging yielded the values of k and k_1. Fig. 4.7 shows the values of k and k_1 obtained in all of the tests. It can be figured out that there are not strong correlations between the input variables and the values of k and k_1, and the average values of k and k_1 were 3.49×10^{10}(N/m^2) and 0.413, respectively. Consequently, in the present work, the grinding forces in UAIG and CIG at time t_0 can be expressed with Eqs. (20) and (21), respectively, by substituting k=3.49×10^{10}(N/m^2) and k_1=0.413 into Eq. (19).

$$\begin{cases} F_{t-UAIG} = 1.44\times10^{10}\sqrt{\dfrac{2R_g a_e}{1-R_g/(R_{w0}+V_c t_0)}}\dfrac{b(R_{w0}+V_c t_0)a_e n_w}{R_g n_g L_{c-UAIG}}\dfrac{1}{\Delta t}\int_{t_0}^{t_0+\Delta t}\cos\theta dt \\ F_{n-UAIG} = 3.49\times10^{10}\sqrt{\dfrac{2R_g a_e}{1-R_g/(R_{w0}+V_c t_0)}}\dfrac{b(R_{w0}+V_c t_0)a_e n_w}{R_g n_g L_{c-UAIG}} \end{cases} \tag{20}$$

$$\begin{cases} F_{t-CIG} = 1.44\times10^{10}\sqrt{\dfrac{2R_g a_e}{1-R_g/(R_{w0}+V_c t_0)}}\dfrac{b(R_{w0}+V_c t_0)a_e n_w}{R_g n_g L_{c-CIG}} \\ F_{n-CIG} = 3.49\times10^{10}\sqrt{\dfrac{2R_g a_e}{1-R_g/(R_{w0}+V_c t_0)}}\dfrac{b(R_{w0}+V_c t_0)a_e n_w}{R_g n_g L_{c-CIG}} \end{cases} \tag{21}$$

4.5.2 Grinding forces predictions and model verification

To verify the grinding force model, CIG and UAIG tests under the input variables of n_w=300rpm, n_g=4000rpm, V_c=10μm/min, A_u=0/4μm, f_u=40kHz, A_o=4mm, and f_o=0.625Hz were performed and the forces prediction was also carried out under the same input variables using Eqs.(20) and (21) for comparison. The experimentally obtained and predicted variations of the grinding forces during grinding are plotted in Fig. 4.8 (the subscripts -*P* and -*E* stand for the predicted force and the experimental one, respectively). Comparing the predicted forces with the experimental ones shows that although there are somewhat quantitative differences between them which is probably caused by the lack of the inclusion of some input variables, e.g., coolant, wheel loading, etc. in the development of grinding force model, the variation tendencies and the quantitative values of the predicted forces agree reasonably with those of the experimental ones, both in CIG and in UAIG process. This fact validated

the developed force model. It is also found from Fig. 4.8 that the grinding forces increase with the increasing of the grinding time t_0 both in CIG and UAIG within the tested grinding period in the current grinding conditions.

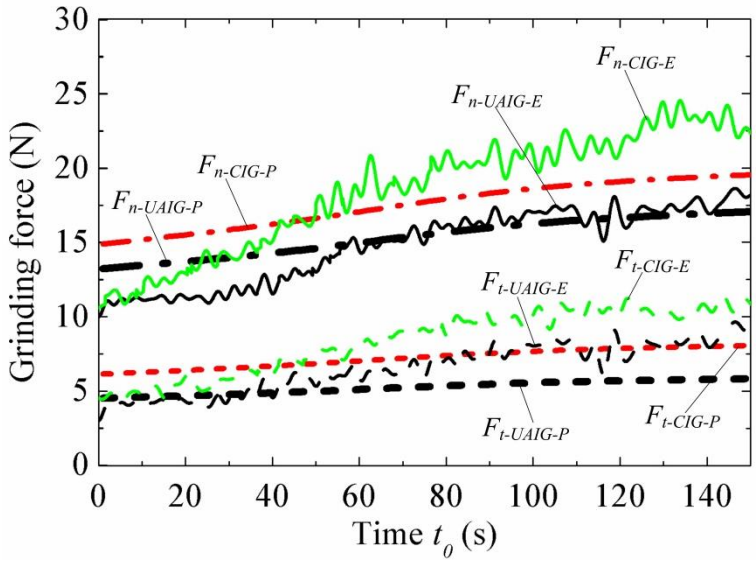

Fig. 4.8 Grinding forces versus time t_0 in UAIG and CIG tests.

Subsequently, to explore the influences of the input variables on the grinding forces, CIG and UAIG tests were performed under different input variables and the grinding forces at t_0 =75s were picked up. As a result, Fig. 4.9 shows the influences of the input variables V_c, n_g, n_w, A_u, f_o on the grinding forces in UAIG and CIG predicted using Eqs. (20) and (21) and obtained experimentally. Obviously, the variation tendencies and the quantitative values of the predicted forces also agree well with those of the experimental ones, regardless of the input variables either in CIG or in UAIG. It is also found from Fig. 4.9 that the grinding forces increase with the increasing of n_w and V_c, but decrease with the increasing of n_g, A_u and f_o; the influences of n_g, n_w and V_c are strong, whereas that of A_u and f_o are significantly weak. Furthermore, it is noticed that the forces in UAIG are significantly smaller than those in CIG, meaning the presence of the UV affects the grinding forces significantly. It is inferred from Eqs. (20) and (21) that the shorter the undeformed chip length $L_{c\text{-}UAIGt}$ or $L_{c\text{-}CIG}$ is, the larger the grinding forces become. The undeformed chip lengths $L_{c\text{-}UAIG}$ in UAIG and $L_{c\text{-}CIG}$ in CIG were calculated with Eq. (11) for various input variables as shown in Fig. 4.10. It is evident that the values of $L_{c\text{-}UAIG}$ in UAIG are larger than those of $L_{c\text{-}CIG}$ regardless of the input variables, indicating the reason why the grinding forces in

UAIG are smaller than those in CIG can also be ascribed to the longer undeformed chip lengths in UAIG.

To evaluate the effect of UV on the grinding forces, force reduction rates were defined as $\eta_n=(1- F_{n\text{-}UAIG}/F_{n\text{-}CIG})\times100$ (%) and $\eta_t=(1- F_{t\text{-}UAIG}/F_{t\text{-}CIG})\times100$ (%) for normal and tangential forces, respectively. The values of η_n and η_t were obtained for different input variables using Eqs.(20) and (21) as shown in the same figure with the undeformed chip length, i.e., Fig. 4.10. Evidently, the η_n and η_t decrease with the increasing of n_g, n_w and V_c, whereas increase with the increasing of A_u and f_o. In the other words, the effect of UV on the grinding force reduction can be enhanced with the decreasing of n_g, n_w and V_c, but increasing of A_u and f_o.

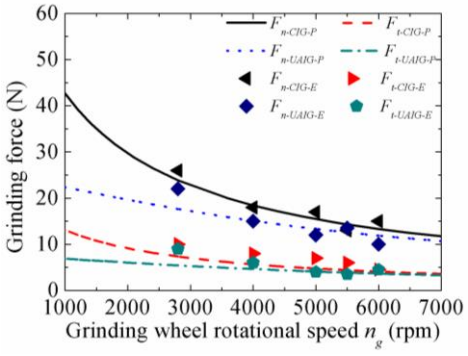

(a) Influence of grinding wheel rotational speed n_g (n_w=300rpm, V_c=10μm/min, A_u=4μm, f_o=0.625Hz)

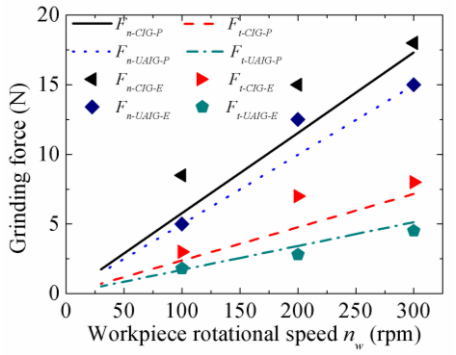

(b) Influence of workpiece rotational speed n_w (n_g=4000rpm, V_c=10μm/min, A_u=4μm, f_o=0.625Hz)

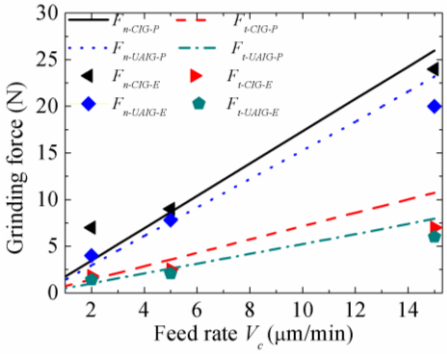

(c) Influence of feed rate V_c (n_g=4000rpm, n_w=300rpm, A_u=4μm, f_o=0.625Hz)

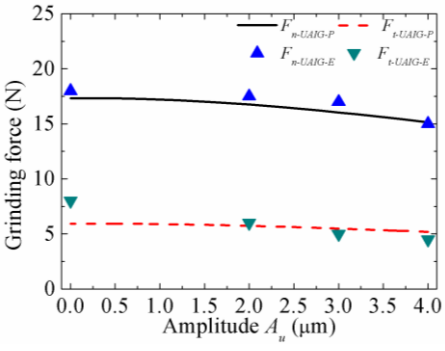

(d) Influence of UV amplitude A_u (n_g=4000rpm, n_w=300rpm, V_c=10μm/min, f_o=0.625Hz)

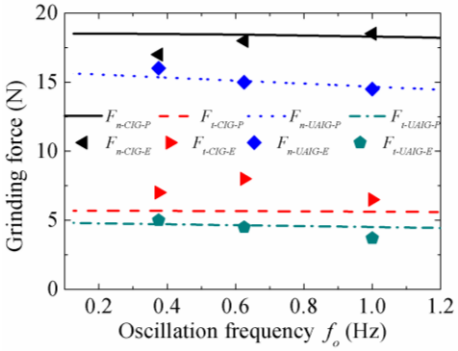

(e) Influence of oscillation frequency

(n_g=4000rpm, n_w=300rpm, A_u=4μm, V_c=10μm/min)

Fig. 4.9 Relations between grinding forces and process parameters

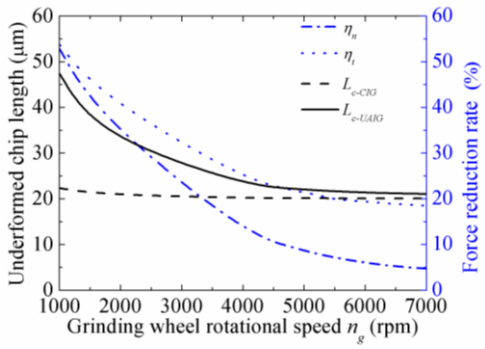

(a) Influence of grinding wheel rotational speed n_g.

(n_w=300rpm, V_c=10μm/min, A_u=4μm, f_o=0.625Hz)

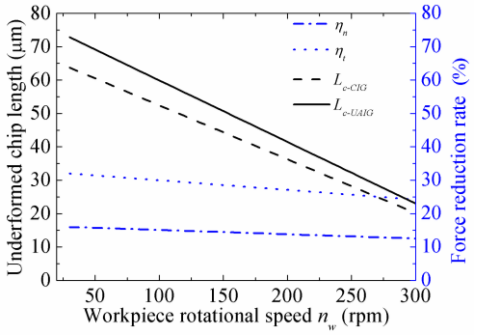

(b) Influence of workpiece rotational speed n_w.

(n_g=4000rpm, V_c=10μm/min, A_u=4μm, f_o=0.625Hz)

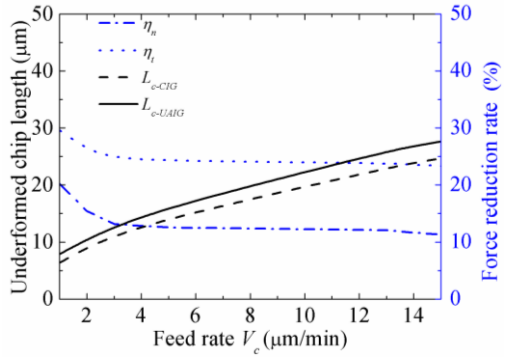

(c) Influence of feed rate V_c

(n_g=4000rpm, n_w=300rpm, A_u=4μm, f_o=0.625Hz)

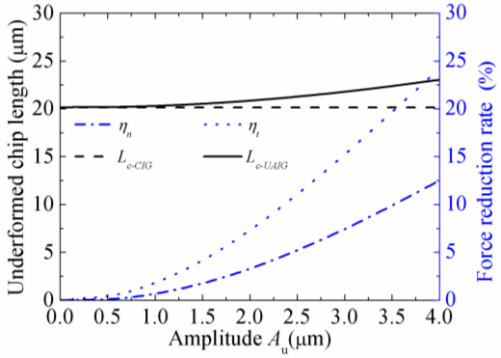

(d) Influence of UV amplitude A_u

(n_g=4000rpm, n_w=300rpm, V_c=10μm/min, f_o=0.625Hz)

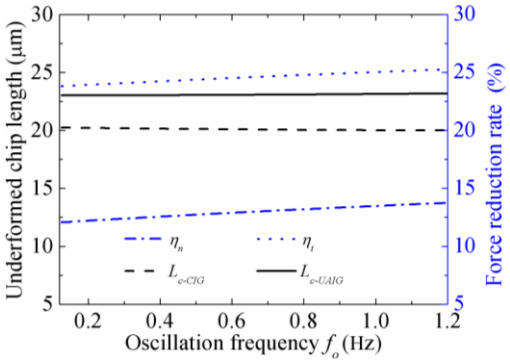

(e) Influence of oscillation frequency f_o

(n_g=4000rpm, n_w=300rpm, A_u=4μm, V_c=10μm/min)

Fig. 4.10 Comparison between the underformed chip length and the force reduction rate for different process parameters.

4.6. Conclusion

In this study, a grinding force model for UAIG of SiC ceramics has been developed. The model incorporates input variables of the grinding process and the UV. Comparing the forces predicted using the developed model with the experimental ones shows that the variation tendencies and the quantitative values of the predicted forces agreed reasonably with those of the experimental ones. Relationships between the input variables and the grinding forces in UAIG can be concluded as following:

(1) The grinding forces increase in the grinding process. Furthermore, the grinding forces are reduced in the UAIG compared to CIG, which is attributed to the formation of the smaller the undeformed chip cross sectional area.

(2) The grinding forces increase with the increasing of n_w and V_c, whereas decrease with the increasing of n_g, A_u and f_o; the influence of n_g, n_w and V_c on grinding force are much pronounced, whereas that of A_u and f_o are not very noticeable.

(3) The force reduction of UV can be enhanced either by decreasing n_g, n_w and V_c or increasing A_u and f_o.

This model can be reliably used for predicting the grinding forces in UAIG of SiC ceramics. It also can be severed as a useful springboard for development of more sophisticated UV assisted cutting force models.

Reference

[1] Agarwal, S. ; Rao, P. V. Predictive modeling of force and power based on a new analytical undeformed chip thickness model in ceramic grinding. *International Journal of Machine Tools and Manufacture* **2013**, *65*, 68-78.

[2] Nomura, M. ; Wu, Y. ; Kato, M. ; Tachibana, T. ; Kuriyagawa, T. Study of internal ultrasonic vibration assisted grinding of small bore : Mechanism of grinding force reduction due to ultrasonic vibration. *Journal of the Japan Society for Abrasive Technology* **2005**, *49* (12), 691-696.

[3] Shimada, K. ; Tateishi, T. ; Yoshihara, N. ; Yan, J. ; Kuriyagawa, T. Ultrasonic-assisted micro-grinding with electroplated diamond wheels. *Journal of the Japan Society for Abrasive Technology* **2009**, *53* (1), 45-48.

[4] Qin, N. ; Pei, Z. ; Treadwell, C. ; Guo, D. Physics-based predictive cutting force model in ultrasonic-vibration-assisted grinding for titanium drilling. *Journal of manufacturing science and engineering* **2009**, *131* (4), 041001.

[5] Li, K. ; Liao, W. Modelling of ceramic grinding processes Part I. Number of cutting points and grinding forces per grit. *Journal of materials processing technology* **1997**, *65* (1), 1-10.

[6] Syoji, K., Grinding manufacturing, Yokendo Press, 2004.

[7] Arfken, G., University physics, Access Online via Elsevier, 1984.

This page intentionally left blank.

Chapter 5 Material removal behavior in ultrasonic-assisted scratching of SiC ceramics with a single diamond tool

Generally, UAIG is considered as one type of UAG techniques. Although ultrasonic-assisted grinding (UAG) has been extensively employed in manufacturing industries for processing hard and brittle materials, its potential has not been sufficiently developed because the material removal mechanism in UAG has not been elucidated. In this chapter, to deeply investigate the material removal mechanism in UAG of hard and brittle materials, the ultrasonic assisted scratching (UAS) tests are performed on SiC ceramics with a self-designed ultrasonic unit. Besides, a validated simulation model is developed to further investigate material removal mechanism tin UAS. The combination of experimental tests and simulation will provide key insights into the single diamond tool scratch process that neither of the methods could provide on its own.

5.1 Introduction

Although many studies focusing on applying UAG methods to hard and brittle materials have been reported, the UAG material removal mechanism, in particular for SiC ceramics, has not yet been sufficiently explored. Normally, the macroscopic results from the grinding process are composed of microscopic effects of individual abrasive grains engaging in cutting actions [1]. Single-grain scratching tests, using an idealized tool, have been commonly used to investigate the behavior of material removal in abrasive machining. The material deformation/fracture patterns arising from the surface morphologies of the scratch provide primary information for determining material removal behavior [2-5]. In the current work, therefore, an

ultrasonic-assisted scratching (UAS) test was performed on SiC ceramics with an in-house-produced ultrasonic unit to investigate the material removal behavior of the UAG on this kind of hard and brittle material. The differences between the material removal characteristics in UAS and conventional scratching (CS) without UV were investigated to provide a comprehensive understanding of the material removal mechanism in the UAG of SiC ceramics. This article describes the design of the tests, the construction of the experimental setup, and experimental investigations of material removal characteristics in UAS and CS, accompanied by detailed discussions.

5.2 Operation principle and kinematic characteristics of UAS

5.2.1 Operation principle

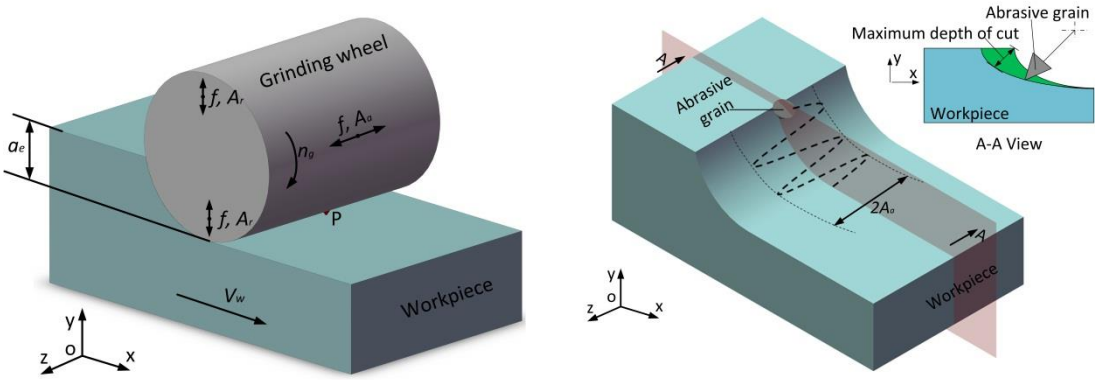

(a) Processing principle (b) Motion trajectory of an abrasive grain on workpiece

Fig. 5.1 Schematic diagram of the UAG.

Figs. 5.1 (a) and (b) show the schematic illustrations of the processing principle of UAG and the motion trajectory of an abrasive grain on the workpiece due to the UAG, respectively. The UV is dominantly applied to the grinding wheel in its own axial direction, i.e., the *z*-axis, at a frequency f and an amplitude A_a; however, due to the L

(longitudinal)-R (radial) crosstalk effect, another UV is, in practice, simultaneously generated in the radial direction at the same frequency f but with a much smaller amplitude A_r. Therefore, this kind of UAG is just the combination of AUAG and VUAG. Once a cut wheel depth a_e is set between the wheel and the workpiece, the wheel then is rotated at a speed n_g followed by a feed motion of the workpiece along the x-axis at a feed rate of V_w, the UAG operation is performed. In the UAG processes, the motion trajectory of an arbitrary abrasive grain, p, generated on the work surface is represented by a spatial spiral line, as shown in Fig. 5.1(b).

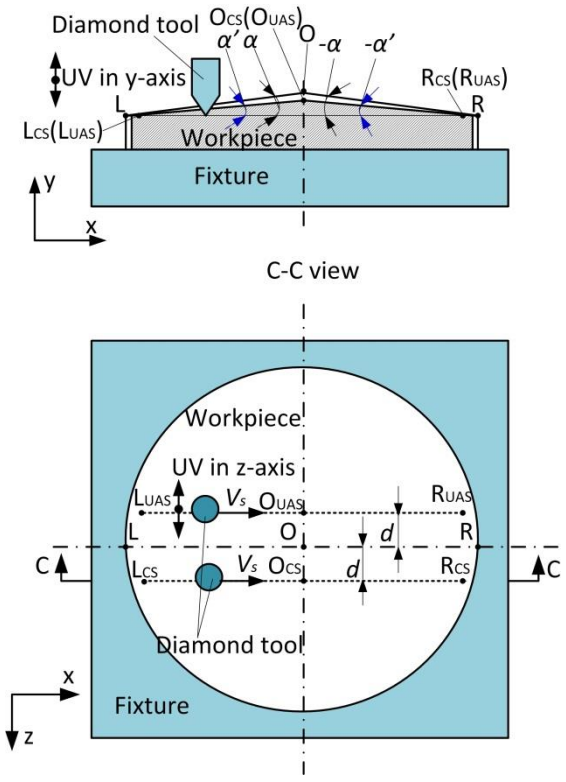

Fig. 5.2 Schematic diagram of ultrasonic assisted scratching (UAS).

To explore the material removal mechanism in this kind of UAG process, a UAS test using a single diamond tool was designed and performed. Fig. 5.2 schematically illustrates the operation principle of the UAS test. The diamond tool is moved right along the line $L_{UAS}O_{UAS}R_{UAS,}$ which is parallel to the disc-shaped workpiece diameter LOR at a distance d at a speed V_s. Considering that the wheel is ultrasonically vibrated in its axial and radial directions simultaneously in UAG, the diamond tool is

also ultrasonically vibrated in two directions, i.e., the *y*- and *z*-axes, simultaneously, at the same frequency *f* but different amplitudes A_y and A_z in the UAS test. In addition, as observed in Fig. 1(b), in the UAG the grain depth of cut, initially, is zero when the abrasive grain starts its cutting action and gradually increases to reach its peak value (maximum depth of cut), eventually the depth reaches zero again once the grain leaves the workpiece; the workpiece used in the UAS test was pre-shaped by polishing into a conic mountain with an elevation angle α. Thus, the tilt angles of the lines $L_{UAS}O_{UAS}$ and $O_{UAS}R_{UAS}$ are α' and $-\alpha$', respectively, leading to the gradual increase and then decrease in the mean tool depth of cut during UAS. This means that the mean tool depth of cut increases from zero at L_{UAS} to maximum value at O_{UAS}, which decreases to zero again at R_{UAS}. For comparison, a CS test without UV was also performed by moving the tool along the line $L_{CS}O_{CS}R_{CS}$ on the same workpiece at the same speed V_s used in UAS. The line $L_{CS}O_{CS}R_{CS}$ is parallel to the workpiece diameter LOR at a distance *d*, which is the same as $L_{UAS}O_{UAS}R_{UAS}$.

5.2.2 Kinematic characteristics

Essentially, the cutting action in the scratching process is a physical interaction between the tool and the workpiece. Therefore, it is crucial to clarify the kinematic characteristics of the tool in the UAS test to thoroughly understand the material removal behaviors in the UAS process.

Let the *xyz*-coordinate system (Fig. 5.1) be fixed on the workpiece and its origin be at the scratching start point in the UAS test (the point L_{UAS} in Fig. 5.2), thus the *xyz*-coordinates of the cutting point of the ultrasonically vibrating tool at time *t* can be expressed by Eq. (1) when assuming the initial *xyz*-coordinates of the tool cutting point are (0, 0, 0) at time $t = 0$.

$$\begin{cases} x(t) = V_s t \\ y(t) = A_y \sin(2\pi f t) \\ z(t) = A_z \sin(2\pi f t) \end{cases} \tag{1}$$

The velocities of the tool in the *x*-, *y*- and *z*-directions at time *t*, $V_x(t)$, $V_y(t)$ and $V_z(t)$, respectively, can hence be expressed by Eq. (2) by differentiating Eq. (1) with respect to time *t*.

$$\begin{cases} V_x(t) = V_s \\ V_y(t) = 2A_y\pi f\cos(2\pi ft) \\ V_z(t) = 2A_z\pi f\cos(2\pi ft) \end{cases} \tag{2}$$

For instance, the variations of the displacement and velocity of tool in one UV period *T* in *y*- and *z*-directions under the condition of V_s=0.5m/s, *f*=14.3kHz (*T*=69.9μs), A_y=0.125μm, and A_z=0.6μm are obtained using Eqs. (1) and (2) as shown in Fig. 5.3. Due to the UV in *y*-direction, as shown in Fig. 5.3(a), the tool moves upward (from 0 to 17.5μs and from 52.5 to 69.9μs) and downward (from 17.5 to 52.5μs) alternatively in the cutting process, leading to the depth of cut in UAS varying periodically and its maximum value being greater than that in CS. Turing to *z*-direction as shown in Fig. 5.3(b), the sinusoidal cutting trace of the tool is generated owing to the UV of the tool. Moreover, due to the sinusoidal variations of the velocities in *y*- and *z*- directions, the impact effects of the tool on the workpiece are generated [6].

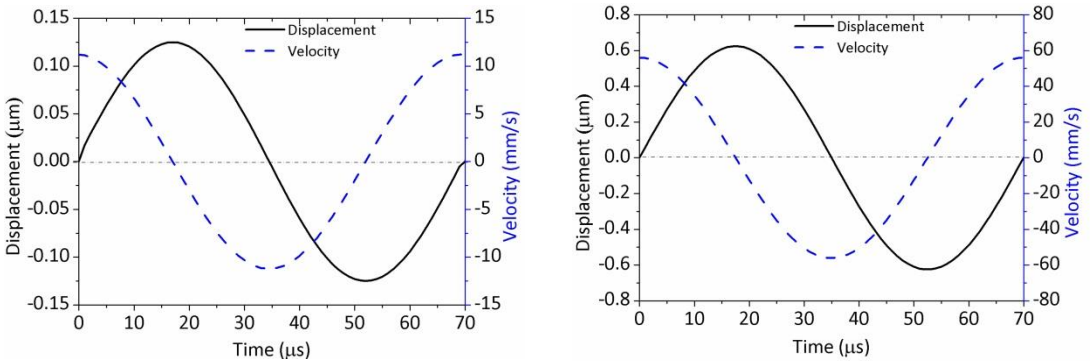

(a) *y*-direction (b) *z*-direction

Fig. 5.3 Kinematic characteristics of the tool in the UAS process

In the UAS process, due to the simultaneous application of the UV in the *y*-direction (frequency *f*, amplitude A_y) and the tool's linear motion in the *x*-direction (speed V_s), the nominal tool depth of cut, *h*(*t*), at time *t* can be expressed as:

$$h(t)=\begin{cases} V_s \tan\alpha' \cdot t - A_y \sin(2\pi ft) & V_s \tan\alpha' \cdot t - A_y \sin(2\pi ft) \geq 0 \\ 0 & V_s \tan\alpha' \cdot t - A_y \sin(2\pi ft) < 0 \end{cases} \quad (3)$$

In Eq. (3), $h(t) = 0$ means the cutting action does not occur. Thus, in the UAS process, there are two scratching modes with different contact situations between the tool and the workpiece (Fig. 5.4(a)): one is intermittent scratching where the condition $V_s \tan\alpha' \cdot t \leq A_y$ is met, and the other is continuous scratching where the condition $V_s \tan\alpha' \cdot t > A_y$ is met.

Shifting the attention to the tool trajectories in the *xz*-plane (Fig. 5.4(b)), due to the simultaneous application of the UV in the *z*-direction (frequency *f*, amplitude A_z) and the tool's linear motion in the *x*-direction, the nominal width of the groove, $w(t)$, at time *t* can be expressed as:

$$w(t)=\begin{cases} 2r(t) + A_z \sin(2\pi ft) & V_s \tan\alpha' \cdot t - A_y \sin(2\pi ft) \geq 0 \\ 0 & V_s \tan\alpha' \cdot t - A_y \sin(2\pi ft) < 0 \end{cases} \quad (4)$$

where $r(t)$ is the major radius of the elliptic plane generated when the tool and the workpiece intersect at time *t* (Fig. 5.4(b)). In the current work, as the angle α' is extremely small, the elliptic intersecting plane can be assumed to be a circular plane with a radius of *r(t)* and it can be obtained from the geometric arrangement between the tool and the workpiece, as shown in Fig. 5.4(a) and as represented below:

$$r(t)=\begin{cases} \sqrt{R^2 - [R - (V_s \tan\alpha' \cdot t - A_y \sin(2\pi ft))]^2} & V_s \tan\alpha' \cdot t - A_y \sin(2\pi ft) \geq 0 \\ 0 & V_s \tan\alpha' \cdot t - A_y \sin(2\pi ft) < 0 \end{cases} \quad (5)$$

where *R* is the nose radius of the diamond tool.

The CS process can be considered as a special case of the UAS process where $A_y = 0$ and $A_z = 0$. Thus, there are no relative motions between the tool and the workpiece in *y*- and *z*-directions, and the nominal width of the groove, $w(t)_{-CS}$, in the CS process can be written as:

$$w(t)_{-CS} = 2\sqrt{R^2 - [R - (V_s \tan\alpha' \cdot t)]^2} \quad (6)$$

Eqs. (4)–(6) could yield the nominal groove widths in the CS and UAS processes.

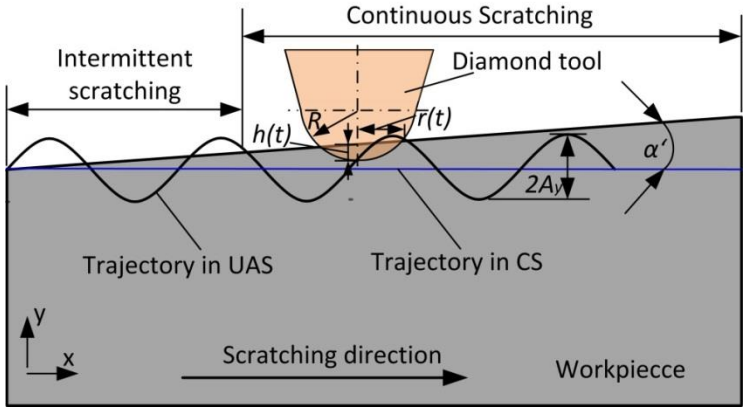

(a) in *xy*-plane

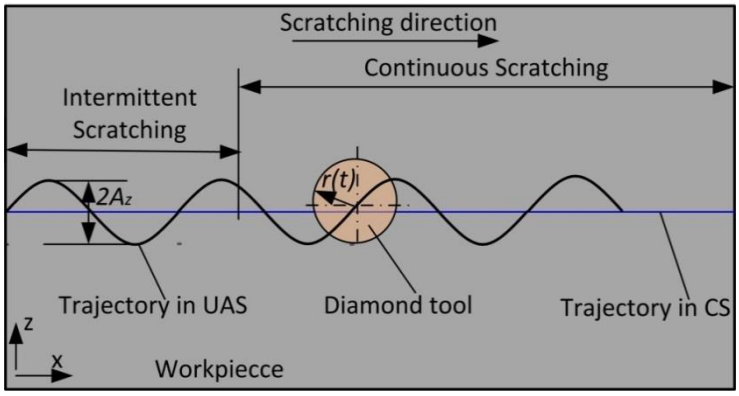

(b) in *xz*-plane

Fig. 5.4 Schematic illustration of the tool trajectories produced in UAS and CS.

5.3 Experimental details

5.3.1 Experimental setup and procedure

Based on the operation principle of UAS, an experimental setup was constructed for scratching tests that is schematically illustrated in Fig. 5.5. An in-house-produced ultrasonic unit, which had a cone-shaped single diamond tool with a vertical angle of 80 ° and a nose radius of 15 μm attached to its lower end face, was installed on the wheel head of an existing NC (Numerical Control) surface grinder (SGT-315RPA by Nagase Integrex Co., Ltd.). A disc-shaped SiC ceramic workpiece (ϕ30 mm × t5 mm) with a surface roughness of 10 nmRa and elevation angle α = 0.018 ° was held on the worktable via a 3D dynamometer (9256A by Kistler Co., Ltd.). The ultrasonic unit

was constructed by bonding a PZT (piezoelectric ceramic) device onto a metal (SUS304) elastic body. A wave function generator (WF1944 by NF Corporation) and two power amplifiers (4010 by NF Corporation) were employed to generate two AC voltage phases that were applied to the PZT to make the diamond tool ultrasonically vibrate in two directions, i.e., the *y*- and *z*-axes, simultaneously. The vibration amplitudes of the tool were measured with two laser Doppler vibrometers (LV-1610 by Ono Sokki Co., Ltd.) for the respective UVs in the *y*- and *z*-axes; the UV amplitudes (peak-valley) were 1.2 μm in the *z*-axis and 0.25 μm in *y*-axis under an AC voltage with a frequency f = 14.3 kHz and an amplitude V_{p-p} = 50 V.

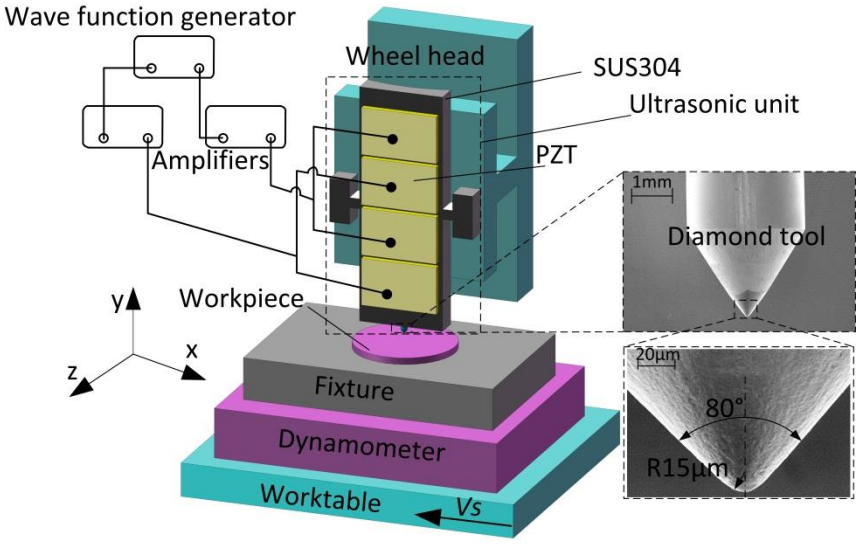

Fig. 5.5 Schematic diagram of experimental setup.

For scratching tests, the scratching speeds, V_s, in either CS or UAS were actually obtained by moving the worktable left along the *x*-axis at a given speed of V_s = 0.5 m/s while keeping the tool stationary. The elevation angle of α = 0.018 ° resulted in α' = 0.015 ° in the case of d = 2.5 mm and the distance from point O to the straight line LR = 4 μm (Fig. 5.2). To understand the material removal mechanism in CS and UAS for SiC ceramics, the behaviors of the material deformation/fracture and the scratching forces were investigated. The former was performed by observing the grooves formed on the work surface with a SEM (ERA-8900S by ELIONIX Co.,

Ltd.), and the latter was conducted by measuring the *x*-, *y*-, and *z*-components of scratching forces with the 3D dynamometer. Before SEM observation, the workpiece was carefully cleaned with an ultrasonic cleaner (US-2 by NSD Co., Ltd.) until the chips that formed during the scratching process were completely removed from the work surface.

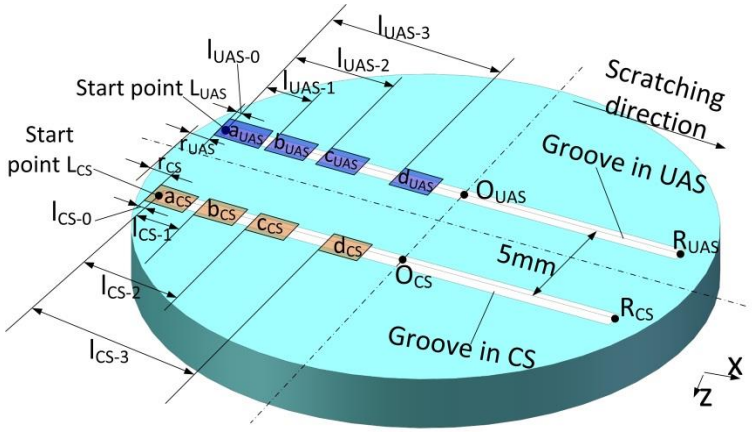

Fig. 5.6 Schematic diagram of the observation regions along the grooves formed in CS and UAS tests.

Due to the tilt of the work surface at angle α' (Fig. 5.2), the mean tool depth of cut varies gradually during CS (or UAS) from point L_{CS} (or L_{UAS}) to point O_{CS} (or O_{UAS}) and further to point R_{CS} (or R_{UAS}); thus, in the first half (from L_{CS} (or L_{UAS}) to O_{CS} (or O_{UAS})) the grooves were formed by different material removal modes, i.e., plastic deformation, ductile removal or brittle fracture. To compare the scratching forces and the material removal behaviors in different removal modes, four distinct regions along each groove were selected for SEM observations and force studies. Fig. 5.6 depicts the locations of the selected regions where a_{CS}, b_{CS}, $c_{CS,}$ and d_{CS} denote the plastic deformation, ductile removal, ductile–brittle hybrid removal, and brittle fracture regions, respectively, for the CS test; the left ends of these regions are at distances of r_{CS}, $r_{CS}+l_{CS-0}+l_{CS-1}$, $r_{CS}+l_{CS-0}+l_{CS-2}$, and $r_{CS}+l_{CS-0}+l_{CS-3}$ from the rim of the workpiece, respectively. The corresponding regions in the UAS test are denoted with a_{UAS}, b_{UAS}, c_{UAS}, and d_{UAS}, and they are at distances of r_{UAS}, $r_{UAS}+l_{CS-0}+l_{UAS-1}$, $r_{UAS}+l_{CS-0}+l_{UAS-2}$,

and $r_{UAS}+l_{CS-0}+l_{UAS-3}$, respectively, from the rim of the workpiece.

5.4 Experimental results and discussions

5.4.1 SEM observation of scratching grooves

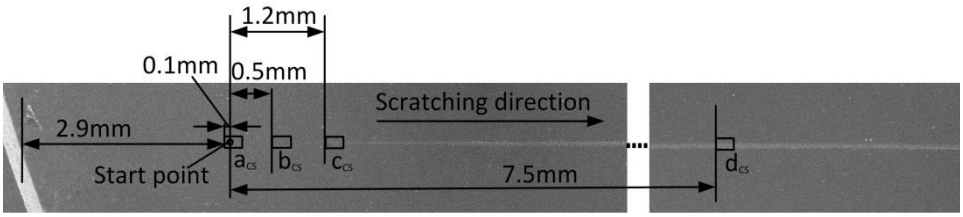

(a) Along line $L_{CS}O_{CS}$ (as shown in Fig.5.6) in CS

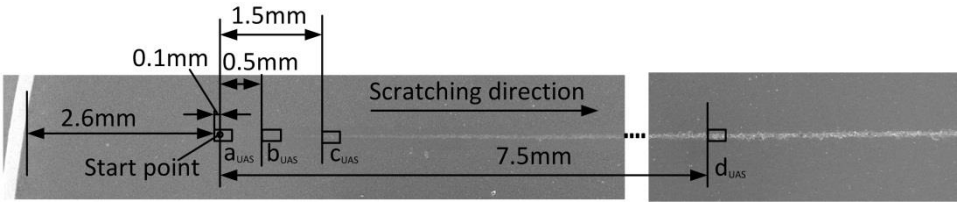

(b) Along line $L_{UAS}O_{UAS}$ (as shown in Fig.5.6) in UAS

Fig. 5.7 Macroscopic SEM images of the grooves generated along line $L_{CS}O_{CS}$ in CS and line $L_{UAS}O_{UAS}$.

Firstly, to determine the locations of the regions, SEM observation was carried out on the workpiece after scratching with and without UV. Figs. 5.7(a) and (b) show the macroscopic SEM images of the grooves generated along line $L_{CS}O_{CS}$ in the CS test and along line $L_{UAS}O_{UAS}$ in the UAS test, respectively; thus, indicating that the values of r_{CS}, r_{UAS}, l_{CS-1}, l_{CS-2}, l_{CS-3}, l_{UAS-1}, l_{UAS-2}, and l_{UAS-3} can be determined to be r_{CS} = 2.9 mm, r_{UAS} = 2.6 mm, $l_{CS-0} = l_{UAS-0}$ = 0.1 mm, $l_{CS-1} = l_{UAS-1}$ = 0.5 mm, l_{CS-2} = 1.2 mm, l_{UAS-2} = 1.5 mm, and $l_{CS-3} = l_{UAS-3}$ = 7.5 mm, respectively.

Next, microscopic SEM images were obtained for all the groove regions generated from the CS and UAS tests to distinguish the differences between the material removal behaviors in CS and UAS in detail. Figs. 5.8(a)–(d) show the microscopic

SEM images in different regions of the groove formed in the CS test. The figures show that a straight groove was obtained from CS, in which different material deformation/fracture behaviors occurred along the scratching trace. In region a_{CS} (Fig. 5.8(a)), the groove started to form at the start point and its surface was smooth (see the close-up), indicating that the groove was predominantly formed due to the plastic deformation and/or ductile removal mode owing to insufficient compressive stress and shear stress to induce cracks [7]. As tool depth of the cut increases, a deeper and wider groove was achieved in region b_{CS} (Fig. 5.8(b)) compared to region a_{CS}; the groove surface is smooth, suggesting the material removal behavior in this region is plastic deformation and/or ductile removal. However, as observed in Fig. 5.8(c), obvious macro-brittle fractures and cracks were generated at the position closest to the far right of region c_{CS}, indicating that a ductile–brittle transition occurred in this region and the critical depth of cut can be determined by measuring the groove depth at position C, which is at the front left area of the macro-brittle fractures. As the tool depth of cut further increases, macro-fractures and macro-cracks successively occurred in region d_{CS} over the entire groove, as shown in Fig. 5.8(d), indicating the material has been removed with a brittle removal mode due to the cooperative action of the high compressive stress and shear stress [8].

By contrast, as observed in Figs. 5.9(a)–(d), the material removal behaviors in UAS differ from those in CS. Fig. 5.9(a) indicates that the groove first appeared at the start point in region a_{UAS}; however, the groove is intermittent and comprises a series of local scratches. It is also observed that the groove surface was smooth, indicating that the scratching mode was predominantly ductile; the groove in region b_{UAS} (Fig. 5.9(b)) was comprised of a string of local scratches similar to that in region a_{UAS}, but the scratches were deeper and wider compared to region a_{UAS}. The generation of the intermittent grooves is supposedly due to the intermittent penetration of the tool into the workpiece under the presence of UV as mentioned in section 2.2. In addition, the local scratches that had smooth surfaces indicate that the plastic deformation and/or ductile removal mode occurred in this region. As the tool reaches region c_{UAS}, the groove becomes continuous, as shown in Fig. 5.9(c), because the tool depth of cut is

larger than the UV amplitude in the *y*-direction. Therefore, the UAS process can generally be separated into two scratching modes: intermittent and continuous scratching. It is also found from Fig. 5.9(c) that the first macro-brittle fracture appeared at the far right of region c_{UAS} and the groove depth at position C is equal to the critical depth of cut, meaning that a ductile–brittle transition occurred in this region. As the tool moves further into region d_{UAS} (Fig. 5.9(d)), many macro-brittle fractures and cracks can be observed in the groove, suggesting that the brittle fracture mode was the main material removal behavior in this region. Compared to CS process results, it is found that the UAS process results in large-scale material removal from the lateral sides of the groove (appearing as serrations), i.e., lateral brittle fractures and cracks, as shown in Fig. 5.9(d). Furthermore, the profile of the groove indicates that the scratching trace of tool appears sinusoidal when ultrasonic vibration is applied.

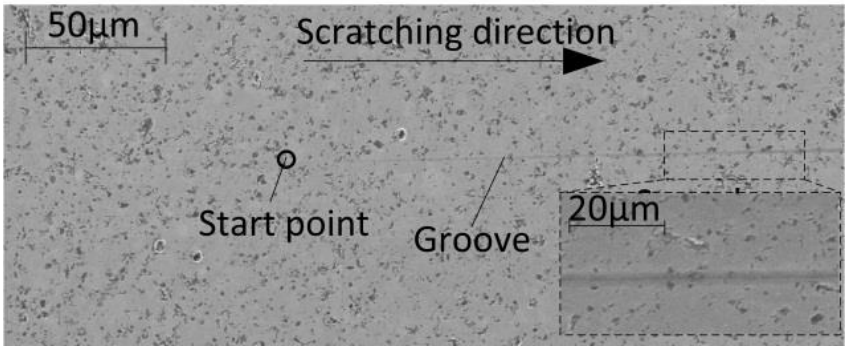

(a) Region a_{CS}

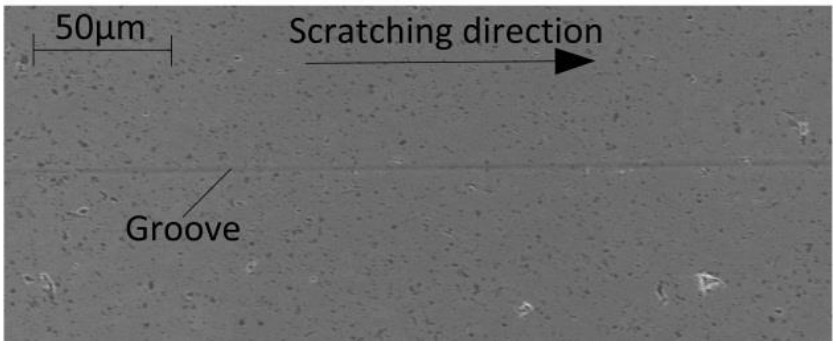

(b) Region b_{CS}

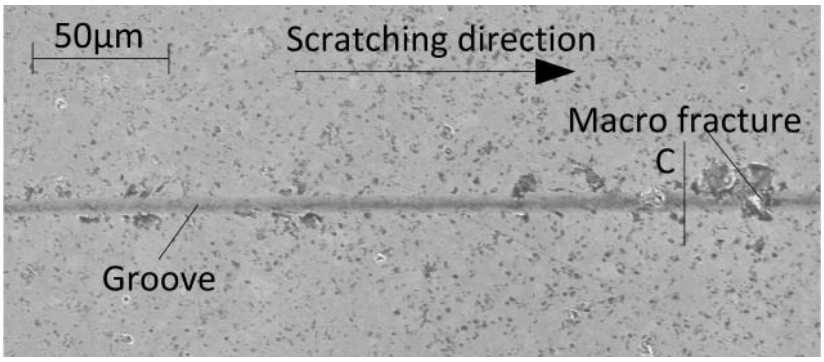

(c) Region c_{CS}

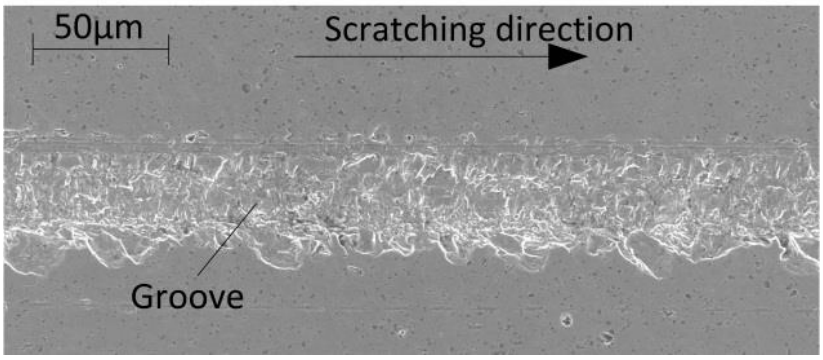

(d) Region d_{CS}

Fig. 5.8 SEM images in different regions of the grooves formed in the CS.

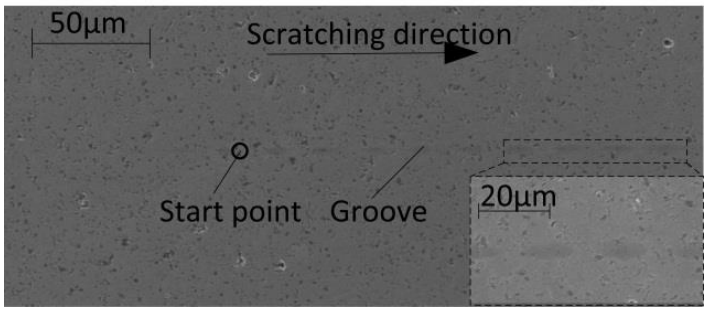

(a) Region a_{UAS}

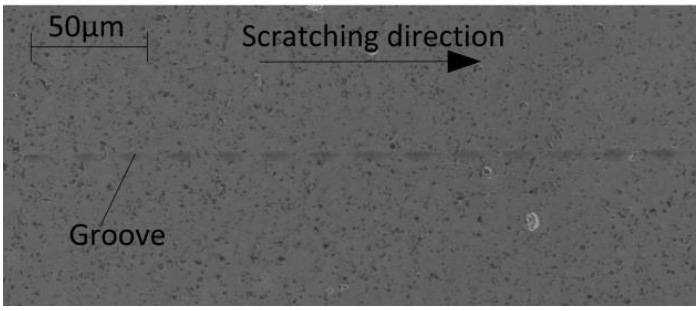

(b) Region b_{UAS}

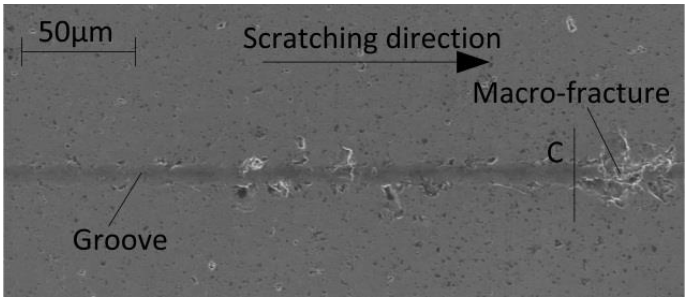

(c) Region c_{UAS}

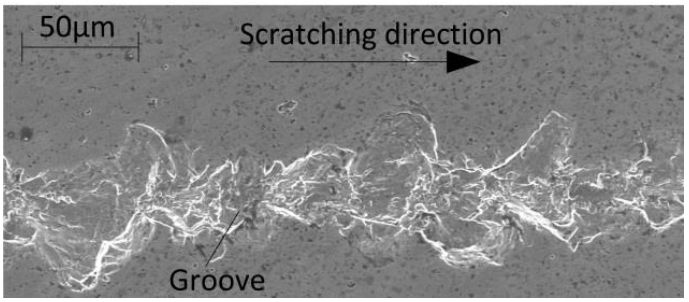

(d) Region d_{UAS}

Fig. 5.9 SEM images in different regions of the grooves formed in the UAS.

5.4.2 Cross-sectional profiles and depths/widths of grooves

To quantitatively investigate the material removal behaviors in CS and UAS, the cross-sectional profiles and the depths/widths of the grooves at different locations with different removal modes, i.e., ductile (regions b_{CS} and b_{UAS}), ductile–brittle transition (regions c_{CS} and c_{UAS}), and brittle (regions d_{CS} and d_{UAS}) modes were obtained with the 3D function of the SEM.

Fig. 5.10 shows the 3D-SEM images, the cross-sectional profiles, and the depths/widths at different locations in different regions of the groove obtained in the CS test. It can be seen from Fig. 5.10(a) that in region b_{CS} the groove was formed with single V-shaped cross-sectional profiles at all the four locations selected. Comparing the cross-sectional profiles of the V-shaped groove and the cone-shaped tool used (Fig. 3) reveals that the work material suffered plastic deformation and/or ductile removal as mentioned in section 3.2.1. However, in region c_{CS} as shown in Fig. 5.10(b), the groove was generated either by plastic deformation and/or ductile removal at locations 1–4 or by brittle fractures just after location 4, confirming that a ductile–brittle transition occurred in this region. The groove depth of about 0.08 μm at location 4 can hence be determined as the critical depth of cut. As the tool depth of cut further increases, the groove cross-sectional profile (Fig. 5.10(c)) became more jagged rather than having a single V-shape (Fig. 5.10(b)) in region d_{CS} due to the occurrence of macro-fractures and macro-cracks over the entire region. Shifting the attention to the depth/width of the groove, it can be found that these values tend to increase as the tool depth of cut increases along the scratching direction.

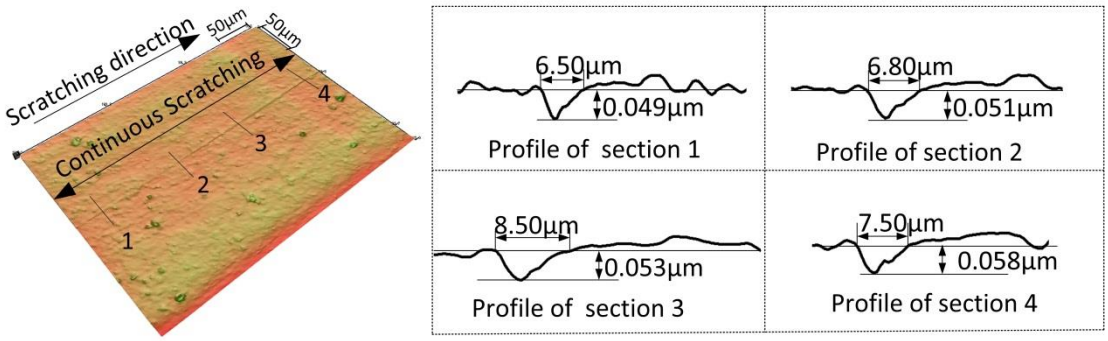

(a) Region b_{CS}

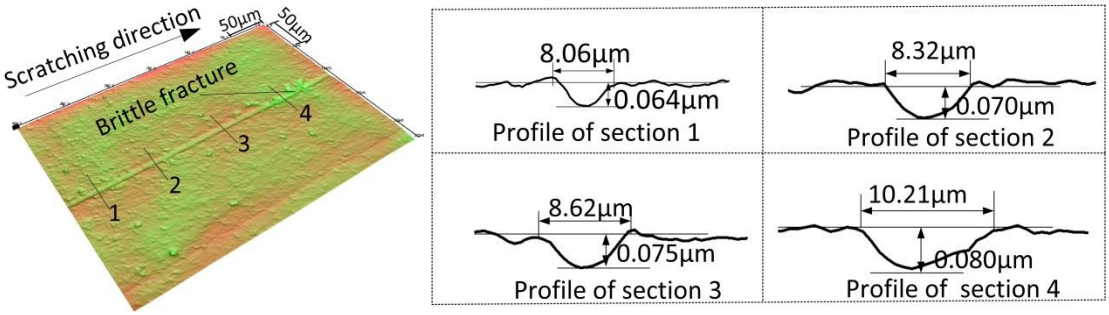

(b) Region c_{CS}

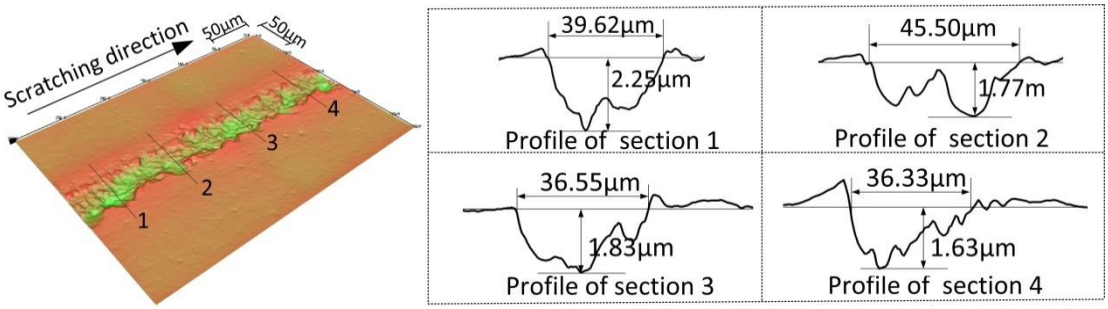

(c) Region d_{CS}

Fig. 5.10 3D-SEM images and cross sectional profiles of the groove formed in the CS test.

For contrast, the 3D-SEM images, the cross-sectional profiles, and the depths/widths at different locations in different regions of the groove obtained in the UAS test are shown in Fig. 5.11. It is observed from Fig. 5.11(a) that, in region b_{UAS}, all the local scratches that comprise the groove (Fig. 5.11(b) is also referred) have similar V-shaped cross-sectional profiles formed due to the plastic deformation and/or ductile removal of material. As the tool is moved in the scratching direction to reach

region c_{UAS}, it can be seen from Fig. 5.11(b) that a macro brittle fracture started to occur soon just behind location 4 and a groove depth of about 0.125 μm at location 4 can be determined to be the critical depth of cut for the ductile–brittle transition. It is noteworthy that the critical depth of cut increased by around 56.25% from 0.08 μm in the CS test to 0.125 μm in the UAS test.

Further in region d_{UAS}, macro-brittle fractures and macro-cracks were formed over the entire region due to the significantly increased tool depth of cut, and thus the groove cross-sectional profiles in this region became jagged (Fig. 5.11(c)). In addition, the lateral cracks and ridges are periodically formed over the entire region. Concretely, there are two lateral cracks in the lateral side of the groove and one ridge in the bottom of the groove in one UV period. Similar to the tendency in the CS process, it is also found from Figs. 5.11(a)–(c) that the groove depth/width increases as the tool is moved in the scratching direction for the UAS process.

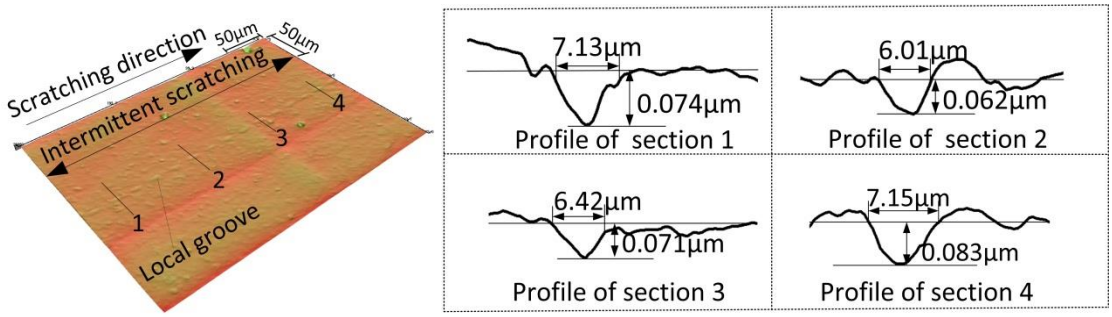

(a) Region b_{UAS}

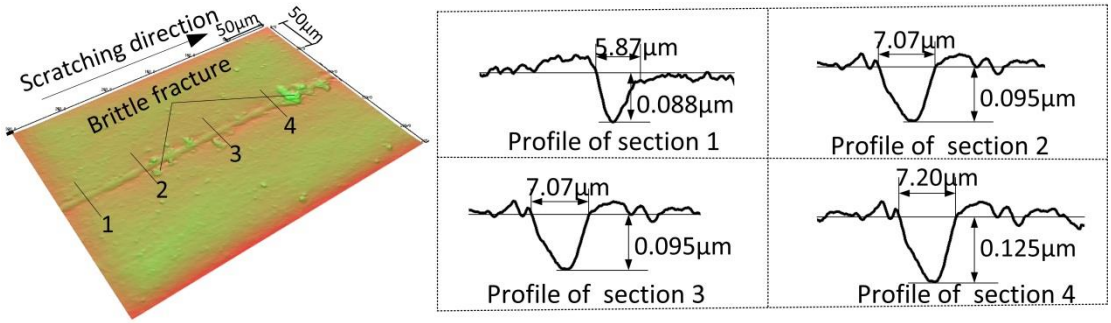

(b) Region c_{UAS}

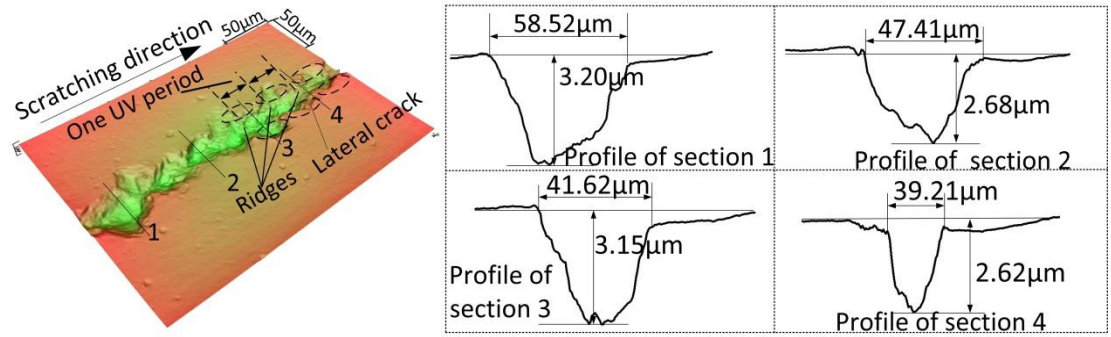

(c) Region d_{UAS}

Fig. 5.11 3D-SEM images and cross sectional profiles of the groove formed in the UAS test.

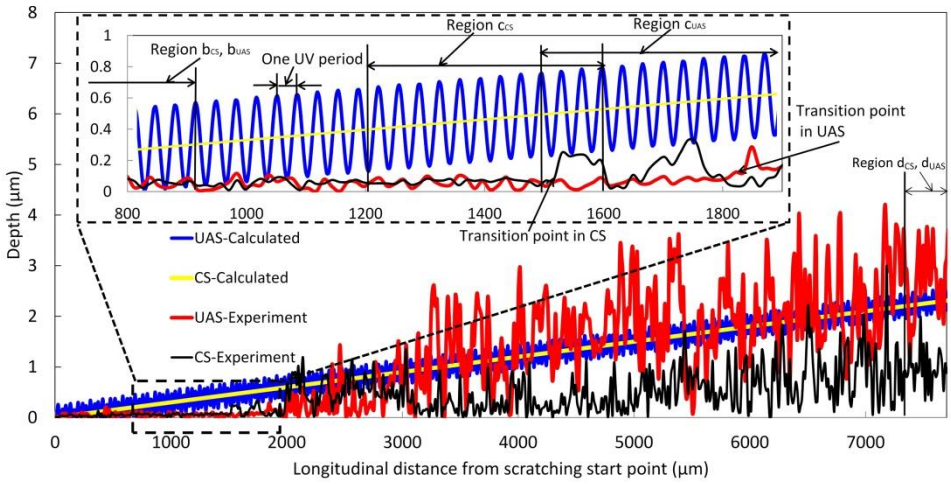

(a) Groove depth

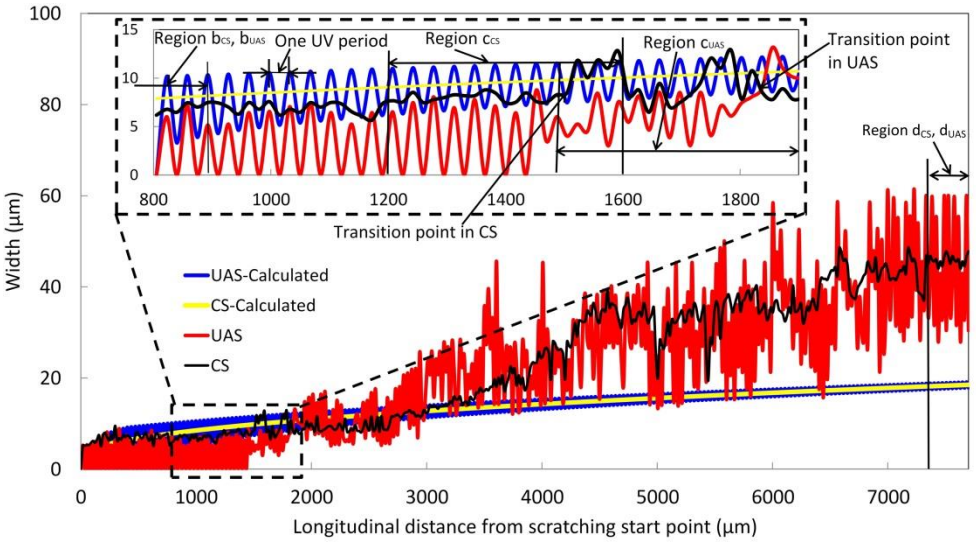

(b) Groove width

Fig. 5.12 Variations of the depth and width of the grooves

The variations of the depth and width of the groove during UAS were compared with those during CS based on Figs. 5.12 (a) and (b), respectively. It is evident from the figures that either the depths or the widths tend to gradually increase during both the CS and the UAS due to the gradual increase in the nominal tool depth of cut (Fig. 5.2). However, it is also observed that the fluctuations in the depth and width in the UAS process are greater compared to the CS process. This phenomenon is considered to be caused by the simultaneous tool UVs in the *y* (depth) and *z* (width) directions. In particular, it is interesting to note that although the mean value of the groove width in the UAS process is smaller than that in CS for the beginning groove region where the

intermittent scratching mode occurred (see the close-up within Fig. 5.12(b)), little difference between the mean values of groove widths in the CS and the UAS processes can be observed in the rest region of the groove where the continuous scratching mode occurred. Further, the difference between the mean values of the groove depths in CS and UAS continue to increase because the groove depth in CS remains shallow over the entire length of the groove, indicating that the cutting ability of the tool was significantly improved by the UV assistance. Thus, it is concluded that the UV in *y*-direction strongly contributes to the material removal in the UAS process. Although cracks are formed on the lateral side of the groove, the UV in *z*-direction only results in the variation of the cutting trace (i.e., approximately sinusoidal cutting trace) and hardly contributes to the material removal.

In addition, the theoretical depth and width of the grooves calculated with Eqs. (3)-(6) are compared with experimental ones in UAS and CS as shown in Figs. 5.12 (a) and (b), respectively. It is found that in CS the experimental depth is smaller than the theoretical value. This is ascribed to the influence of the deflection caused by the inadequate stiffness of the experimental setup. By contrast, although the experimental depth is smaller than theoretical depth in ductile region, the mean value of the experimental depth is close to the mean value of theoretical depth in brittle region in UAS. This means that the stiffness of the experimental setup is improved by the assistance of UV. Further, the fluctuation of experimental depth is found to be greater than the theoretical one. This is probably because of that in the calculation of the theoretical depth with Eq. (3) only the geometrical relationship between the tool and the workpiece was considered and the influence of the kinematic characteristics of the tool on the material removal was ignored. Comparing the theoretical and experimental values of width shows that the theoretical width is larger than experimental one in ductile region and is smaller than experimental one in brittle region both in UAS and CS processes. The insufficiency of stiffness of the experimental setup caused the experimental width to be smaller than the theoretical width in ductile region in UAS and CS processes, and the tool wear in scratching process caused the experimental

width to be larger than the theoretical width in brittle region in UAS and CS processes.

From the variations of the velocities (Fig. 5.3), it is found that there are two variation phases in one UV period: one is velocity increment phase (from 17.5 to 35μs and from 52.5 to 69.9μs), the other is velocity decrement phase (from 0 to 17.5μs and from 35 to 52.5μs). In the increment phase, the tool moves from the vertex to the equilibrium position of the sinusoidal trajectory as the velocity increases from zero to maximum absolute value (11mm/s in the *y*-direction and 54mm/s in *z*-direction), leading to the kinetic energy of the tool reaching its maximum value. On the contrary, in the decrement phase, the velocity decreases from maximum absolute value to zero in *y*- and *z*-directions, and hence the tool impacts on the workpiece with high kinetic energy. Upon impact of the tool on the workpiece, the crack or the material removal occurs at the point of impact [9-11], resulting in the expansion of the ductile removal/brittle fracture zone in the UAS process. The expansion of the deformation/fracture area is the main factor that induces deeper grooves and forms the lateral cracks compared to CS, eventually leading to the more materials being removed, i.e., the cutting ability of the tool was improved in the UAS process compared to that in CS. The improvement of the stiffness in UAS may be ascribed to the cutting ability of the tool was improved in the UAS process compared to that in CS.

In addition, as mentioned above, the impact occurs twice in one UV period in *z*-direction. However, owing to the tool moving upward, the impact effect of the tool will not act on the workpiece from 0 to 17.5μs in *y*-direction, thus the impact effect acting on the workpiece occurs only one time in one UV period in *y*-direction. Therefore, two lateral cracks in the lateral side of the groove and one ridge are formed in the bottom of the groove in one UV period as shown in Fig. 5.11(c).

5.4.3 Scratching forces

Figs. 5.13(a) and (b) show the variations of the scratching forces during the CS and UAS processes (time t = 0 is the time when scratching starts), respectively. It can be seen from the figures that for both CS and UAS the mean scratching forces values both in the x- and y-directions tend to gradually increase in the first half from zero to a peak and then they decrease to reach zero again in the latter half, whereas the mean values of the forces in the z-direction remain at zero during the entire time. This is because the nominal tool depth of cut gradually increases in the first half and then decreases in the latter half as illustrated in Fig. 5.2. It is further noted that the three force components either in the CS process or in the UAS process fluctuate during scratching; however, the fluctuations in the UAS process are greater than those in the CS process. Comparing the scratching forces in UAS and CS shows that the mean values of the normal (in y-direction) and tangential (in z-direction) forces in UAS are smaller than those in CS.

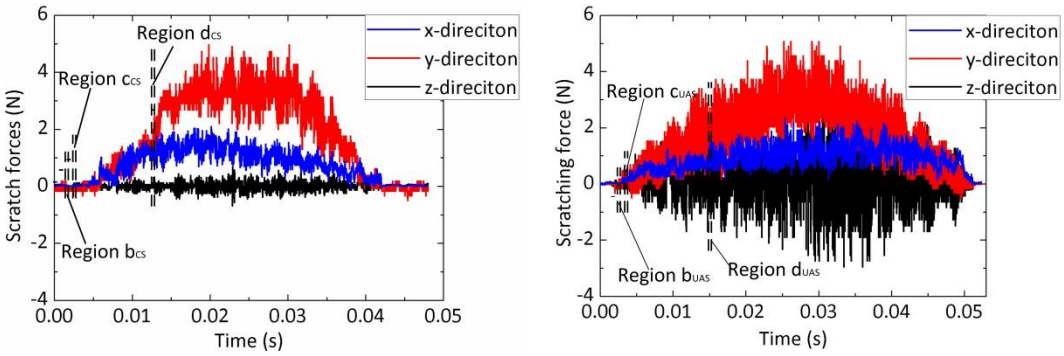

(a) In the whole CS process from L_{CS} to R_{CS}

(b) In the whole UAS process from L_{UAS} to R_{UAS}

Fig. 5.13 Scratching forces in the CS and the UAS processes.

Additionally, the length, L_{UAS}, of the diamond tool's trajectory in the UAS process in the time period from an arbitrary time t_1 to another arbitrary time t_2 ($t_2 > t_1$) is given by the equation below with the help of Eq. (2).

$$L_{UAS} = \int_{t_1}^{t_2} \sqrt{V_x^2(t) + V_y^2(t) + V_z^2(t)}\,dt = \int_{t_1}^{t_2} \sqrt{V_s^2 + (2\pi f A_y \cos(2\pi f t))^2 + (2\pi f A_z \cos(2\pi f t))^2}\,dt \quad (7)$$

As aforementioned, the CS process can be considered to be a special case of UAS where $A_y = 0$ and $A_z = 0$. It is, thus, deduced from Eq. (7) that the length of the tool's trajectory in UAS is longer than that in CS under the same conditions. Zhang et al.[5] reported that, in UAS with constant volumetric material removal, a longer tool trajectory length leads to a smaller tool depth of cut. It is also well known that the cutting forces increase as the depth of cut increases [12]. Thus, it is deduced that the scratching forces will be smaller in UAS compared to CS since the tool trajectory length in UAS is longer than CS when volumetric material removal volume is kept constant. This may result in the mean values of the normal and tangential forces in the UAS process being smaller than those in the CS process, as shown in Figs. 13(a) and (b).

5.4.4 Ductile-brittle transition mechanism

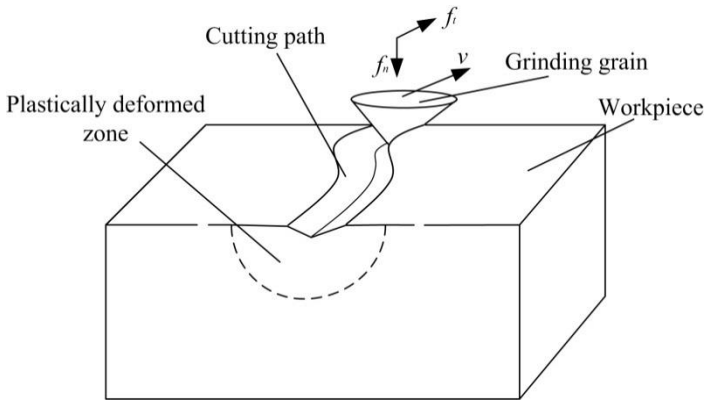

Fig. 5.14 Schematic of an abrasive grain removing material from a brittle workpiece via ductile-mode grinding

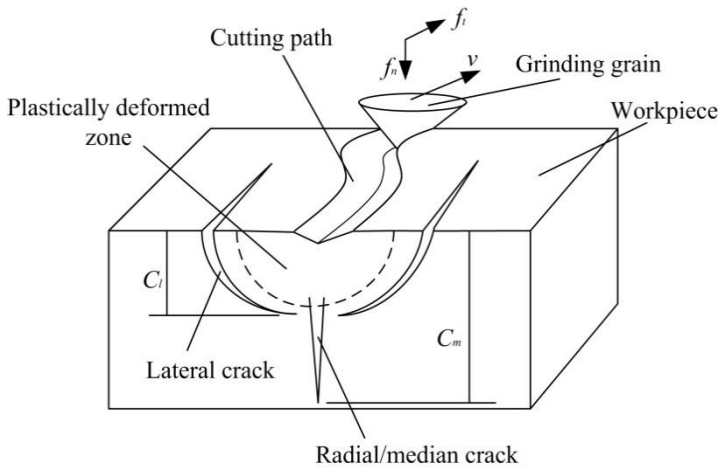

Fig. 5.15 Schematic of an abrasive grain removing material from a brittle workpiece via brittle-mode grinding

Fig. 5.14 is a schematic of an abrasive grain-removing material in a ductile-mode from a brittle workpiece. If the grinding force is small enough, then the grain plows a groove via plastic deformation of the workpiece, leaving a ductile-ground groove and a subsurface region of plastically deformed material. This is the ductile material-removal mode [13].

Just beneath the plastic deformation zone is a region of residual tensile elastic stress resulting from the plastic deformation. If the grinding force is increased, the groove depth, plastic deformation zone, and elastic tensile stresses are also increased. At some critical grinding force, a radical/median crack forms beneath the abrasive grain, propagating to a depth t_c. If the force is increased above the threshold for median crack formation, the residual stresses left in the workpiece at the base of the plastic deformation zone will propagate cracks after the grinding grain has passed. These are called lateral cracks, and their formation and propagation to the workpiece surface leads to brittle material removal. A schematic of brittle-regime material removal is illustrated in Fig. 5.15 [13].

5.4.4.1 Threshold energy for radial/median and lateral fracture

In analysis, the workpiece hardness is assumed constant throughout the region of the grinding. With rise in the grinding force, the volume of the grinding zone as well as plastic zone will increase. At a certain grinding force, the tensile stresses at the boundary of the plastic zone will exceed the fracture limit of the workpiece material and subsequently cracks will initiate. Therefore, the crack initiation can be expressed based on the threshold volume of the indentation zone and denoted by δV [14].

Slikkerveer et al. [15] presented the removed volume related to the crack threshold for radial/median cracks:

$$\delta V_R = \left(\frac{3}{2\pi}\right)^3 \frac{\mu^6}{\beta^6} \frac{E^{3/2} K_{IC}^6}{H^{15/2}} \tag{8}$$

Where E is Young's modulus of the workpiece material, K_{IC} is fracture toughness of the workpiece material, H is hardness of the workpiece material.

And for lateral cracks:

$$\delta V_L = \frac{1}{3} \frac{\zeta_0^{3/2}}{\alpha^{1/2} A^3} \frac{E^{3/2} K_{IC}^6}{H^{15/2}} \tag{9}$$

The parameter μ in Eq. (8) is a dimensionless constant which correlates the size of the grinding zone with that of the plastic zone. Also, parameter β is a constant, independent of material properties and grinding grain shape. Furthermore, the parameter ζ_0 in Eq. (9) is an empirical constant obtained from experiments with Vickers indenters. Finally, α and A are the shape factor of the grinding grain and shape factor of the workpiece material chip above the lateral crack respectively.

The energy U absorbed by workpiece material with the work done by the grinding grain through the cutting event, can be written as the following equation [15]:

$$U = H \cdot \delta V \tag{10}$$

Therefore, the required threshold energy U_r to initiate the radial/median cracks:

$$U_r = \left(\frac{3}{2\pi}\right)^3 \frac{\mu^6}{\beta^6} \frac{E^{3/2} K_{IC}^6}{H^{13/2}} \tag{11}$$

Similarly, the threshold energy U_l for initiation of the lateral cracks is presented as:

$$U_l = \frac{1}{3}\frac{\zeta_0^{3/2}}{\alpha^{1/2}A^3}\frac{E^{3/2}K_{IC}^6}{H^{13/2}} \tag{12}$$

5.4.4.2. Consumed energy in the ductile-mode and brittle-mode grinding

According to the energy conservation law, the energy absorbed by workpiece material is equal to the energy consumed in ductile-mode grinding done by the grinding grain through the cutting event;

The energy consumed in ductile-mode grinding is the product of tangential cutting force and cutting velocity, it can be written as [16]:

$$U_d = f_n v \tag{13}$$

Where U_d is the energy consumed in ductile-mode machining, f_n is the normal force of a single abrasive grain in the cutting process in UAIG, v is the cutting velocity.

In brittle-mode machining, material is removed by crack propagation. From the indentation test results of brittle materials, it has been established that there are two major types of crack systems i.e. radial/median and lateral [13].

$$U_b = (2C_l + 2C_m)v\gamma_s \tag{14}$$

Where U_b is the energy consumed in brittle-mode machining, C_l is the length of lateral crack, C_m is the length of radial/median crack, γ_s is the surface energy of the material (usually a constant).

The length of the radial/median C_m is determined by the critical load of fracture and fracture toughness of the material [17]:

$$C_m = \left(\frac{4\chi P_c}{K_{IC}}\right)^{2/3} \tag{15}$$

Where χ is the geometric constant and its value is 0.064 for most of brittle materials, P_c is the load at the critical point aligned in the direction of radial/median crack, here P_c=f_n.

It was identified in abrasive machining that the surface damage could approximately be correlated to the subsurface damage [13]:

$$C_l \cong \frac{C_m}{7} \tag{16}$$

In brittle-mode grinding, it is important to note that plastically deformed zone still exists though material is removed by the crack propagation as shown in Fig. 2. Therefore, the total consumed energy in brittle-mode grinding is given by:

$$U_{total} = U_d + U_b = (2C_l + 2C_m)v\gamma_s + f_n v = \frac{16}{7} v[\left(\frac{4\chi f_n}{K_{IC}}\right)^{2/3} \gamma_s + f_n] \tag{17}$$

5.4.4.3 Critical depth of cut

Threshold energy for radial/median and lateral cracks could be applied as an indication of the transition points between plastic deformation, radial crack initiation and lateral fracture in processes dealing with machining hard and brittle materials [15]. If the total energy consumed in the brittle-mode grinding which is transferred into the workpiece material done by the grinding grain through the cutting event, exceeds its threshold energy for crack initiation, material removal takes place in brittle mode i.e. by lateral fracture [14]; otherwise, material is removed in a ductile mode. Based on this rationale, one can consider that:

If $U_l < U_{total}$ (18)

Lateral crack and material is removal by crack propagation in a brittle mode.

If $U_l = U_{total}$ (19)

Ductile mode of energy transits into the brittle mode, the transition point is considered as the critical depth of cut.

From Eq. (12), it is known that the threshold energy U_l for initiation of the lateral cracks. i.e., the threshold energy for brittle mode is a constant value. It is known from section 5.4.3 that grinding force in UAIG is smaller than that in CIG, thus, it is deduced from Eq. (17) that the total energy consumed in the brittle-mode grinding U_{total} in UAIG is smaller than that in CIG. Furthermore, it is also known from

chapter 4 that the deeper of the depth of cut is, the bigger a single abrasive grain normal force f_n becomes. Therefore, it is deduced that grinding force in UAS is smaller than that in CS, leading to the deeper depth of cut in UAS being necessary to generate brittle-mode grinding compared to that in CS. This may be the reason the critical depth of cut in the UAS test was larger than that in the CS test.

5.4.5 Cutting efficiency and nature of material removal

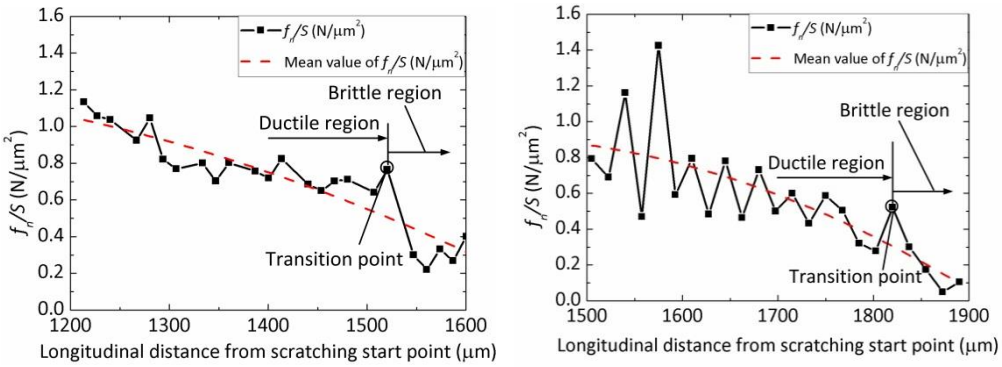

(a) CS (b) UAS

Fig. 5.16 Variation of the f_n/S in ductile-brittle transition region c_{CS} and c_{UAS} during the CS and UAS processes.

To investigate the cutting efficiency of the UAS process, f_n/S, where S is the groove cross sectional area (i.e., the contact area between the tool and the workpiece in the actual cutting action), in the ductile-brittle transition region, c_{CS} and c_{UAS}, are studied. As shown in Fig. 5.16, before the ductile-brittle transition occurs, f_n/S shows a slow decreasing trend both in CS and UAS, whilst f_n/S fluctuates approximately in sinusoidal pattern in UAS. When the ductile-brittle transition occurs, f_n/S rapidly decreases both in CS and UAS. In addition, f_n/S fluctuates with a wider range in UAS than does in CS, and also the mean value of f_n/S in UAS is smaller than that in CS. The smaller the f_n/S is, the smaller the force for removing unit volume of material, indicating that the cutting efficiency has been improved. As a result of the impact of

tool on the workpiece in *y*- direction, more material is removed in UAS compared to that in CS. This eventually lead to the higher cutting efficiency in UAS compared to CS. In addition, f_n/S is smaller in brittle region than that in ductile region, meaning that the cutting efficiency is higher in brittle region than that in ductile region.

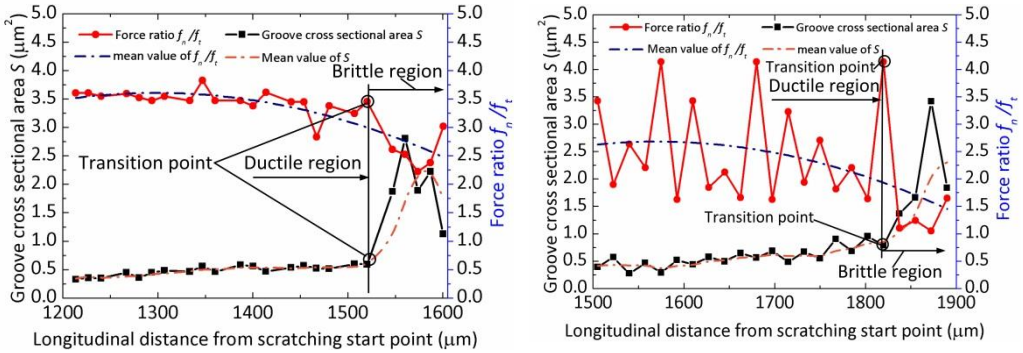

(a) CS (b) UAS

Fig. 5.17 Variation of the groove cross sectional area and the force ratio f_n/f_t during CS and UAS processes.

To understand the nature of the material removal mechanism in UAS, the variation of the groove cross sectional area *S* and the ratio of the normal force f_n to the tangential force f_t, f_n/f_t, during the CS and UAS processes in the ductile-brittle transition regions, c_{CS} and c_{UAS}, are investigated. As shown in Figs. 5.17, before the ductile-brittle transition occurs, groove cross sectional area *S* increases slowly, whilst the force ration f_n/f_t decreases slowly both in the CS and UAS. Further, *S* and f_n/f_t are found to fluctuate approximately in sinusoidal pattern in the UAS. When the ductile-brittle transition occurs, the force ratio f_n/f_t suddenly decreases with a rapid increase in the groove cross sectional area *S* both in UAS and CS. In addition, comparing *S* and f_n/f_t in CS with those in UAS, the results show that although the fluctuations of *S* and f_n/f_t in UAS are heavier than that in CS, the mean value of *S* in UAS is bigger than that in CS while the mean value of f_n/f_t in UAS is smaller than that in CS. In grinding processes, the force ratio f_n/f_t mainly depends on the grindablity of workpiece material [18]. The larger the force ratio f_n/f_t becomes, the lower the grindablity of workpiece material are [19]. Due to the impact of tool on the workpiece

in *y*- direction, the mean value of *S* in UAS is bigger than that in CS as shown in Fig. 5.17. This leads to more materials being removed in UAS compared to CS. The force ratio f_n/f_t is smaller in UAS than that in CS as shown in Fig. 5.17, which leads to the cutting ability in UAS being improved. Moreover, the force ratio f_n/f_t in brittle region is smaller than that in ductile region both in UAS and CS as shown in Fig. 5.17, which leads to the cutting ability being improved in brittle region.

On the basis of above discussions, it is concluded that due to the impact of tool on the workpiece in *y*- direction, not only the more material is removed, but also the cutting efficiency and cutting ability are improved. The impact and cutting action at the tool tip on the machining surface are the main factors contributing to the material removal.

5.5. Simulation details

To fully explore the material removal behavior in the UAS process, a quantitative analysis on the material deformation/fracture process, the stress distribution features, and the mechanical property changes in the UAS process are required. These cannot be observed by experimental method. In the current work, a simulated ultrasonic-assisted scratch (UAS) model with a single abrasive grain performed on SiC ceramics was used to investigate the material removal mechanism in the UAG of SiC ceramics.

In simulation, the workpiece is modeled by smooth particle hydrodynamic (SPH) particles. The SPH method, as a truly meshfree, free Lagrangian, particle method, first introduced by Lucy [20], Gingold and Monaghan [21]. The main advantage of the SPH method is to bypass the requirement for a numerical grid to calculate spatial derivatives. Material properties and state variables are approximated at a discrete set of disordered points, called SPH particles. This avoids severe problems associated with mesh tangling and distortion which usually occur in Lagrangian analyses involving large deformation and/or strain rates and extreme loading events [22]. The

material removal process, energy and stresses distributions, and force change process were well demonstrated by SPH method. Therefore, it is suitable to simulate a cutting process using SPH method to investigate the material removal mechanism of UAS of SiC ceramics.

5.5.1 Simulation Model Development

The simulation model was developed and established in Ansys/Ls-dyna. Before the model was developed, the following assumptions were made:

(1) In reality, an individual grain has many tiny cutting points on the surface. However, for simplicity, the grain tips were approximated as hemisphere (Fig. 5.16).

(2) The influence of temperature was ignored in the cutting process.

(3)The scratch time used in this simulation was 105μs. Correspondingly, the depth of cut a_e was unchanged in this short time in the UAS process.

The main physical and mechanical properties of the materials are detailed in Table 5.1. Fig. 5.18 shows the geometry of the grain and the workpiece. The right side of the figure is an enlarged view of the rake face of the grain. The vertical angle of 80° and nose radius of the grain are 80° and 15μm, respectively. The workpiece is 90μm×80μm×30μm. The contact type between the grain and the SPH workpiece was defined using the automatic node-to-surface contact in Ansys/Ls-dyna. The bottom of the workpiece was fully constrained in the scratch process.

The UV with amplitudes of A_y=0.25 and A_z=0.25, and frequency of f=14.3kHz, and feed speed at a speed of V_s=0.5m/s along the x-direction are added on the diamond tool. Depth of cuts a_e are set to be 0.07μm and 2μm in simulations, respectively.

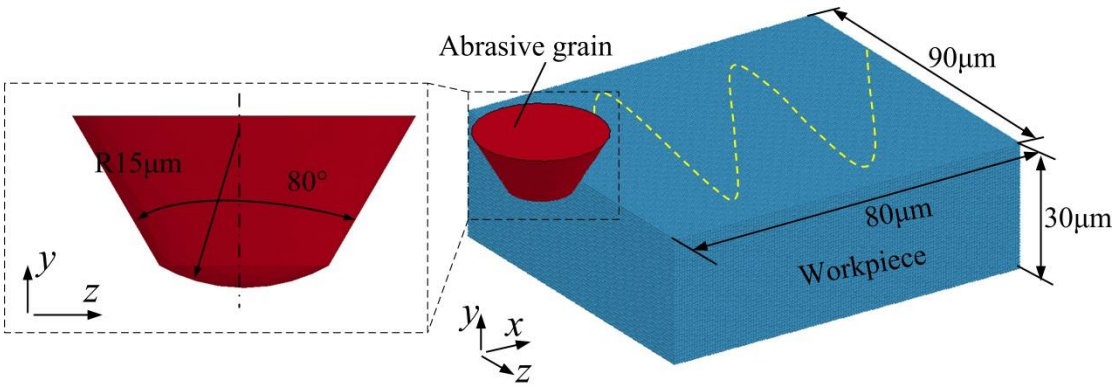

Fig. 5.18 Schematic geometry of the simulation model and tip of the grain

Table 5.1 Material constants of silicon carbide ceramics [23, 24] and diamond [25]

Materials properties	Symbol	Silicon carbide	Diamond
Density	ρ (kg/m^3)	3163	3510
Shear modulus	G (GPa)	183	1200
Poisson's ratio	v		0.1
Tensile strength	T* (GPa)	0.37	
Hugoniot elastic limit (HEL)	HEL (GPa)	14.567	
HEL pressure	p_{HEL} (GPa)	5.90	
HEL strength	T_{HEL} (GPa)	13.0	

5.6 Simulation results and discussion

5.6.1 Cutting force

Figs. 5.19 shows the cutting forces in the scratching process obtained by simulation in the CS and UAS at a_e=0.07μm. In CS process, the forces in x- and y-directions increase from zero until reaching the maximum when the grain cuts into the workpiece completely at 35μs, then the forces stabilize to a certain level until the cutting process was finished, whilst the force in z-direction almost maintains zero in the cutting process (Fig. 5.19(a)). As for the UAS, the cutting forces in x-, y- and

z-directions increase and then decrease severely in a sinusoidal pattern the cutting process (Fig. 5.19(b)). Meanwhile, the force curves are un-continuous.

Shifting the attention to CS at a_e=2μm, similar to that in a_e=0.07μm, the force in *y*-direction increases firstly and then stabilizes to a certain level, whilst the force in *z*-direction also almost maintains zero in the cutting process; however, the force in *x*-direction increases firstly then gradually decreases to stabilized level, which is different from that in a_e=0.07μm (Fig. 5.20(a)). Turing to UAS, the forces also increase and then decrease alternatively whilst the force curves found to be continuous. Further, it is figured out that there are little fluctuations at the a_e=0.07μm (Figs. 5.19(a) and 5.19(b)), while there are obvious abrupt fluctuations at the a_e=2.0μm both in CS and UAS (Figs. 5.20(a) and 5.20(b)). According to the study on scratching of sapphire by Zhang, et al. [15], the scratching forces vary with little fluctuation when the material is removed in ductile mode while fluctuate abruptly when the material is removed in brittle fracture mode. It is hence inferred that the materials were removed in a ductile cutting mode at a_e=0.07μm while the materials were removed in a brittle cutting mode at a_e=2μm.

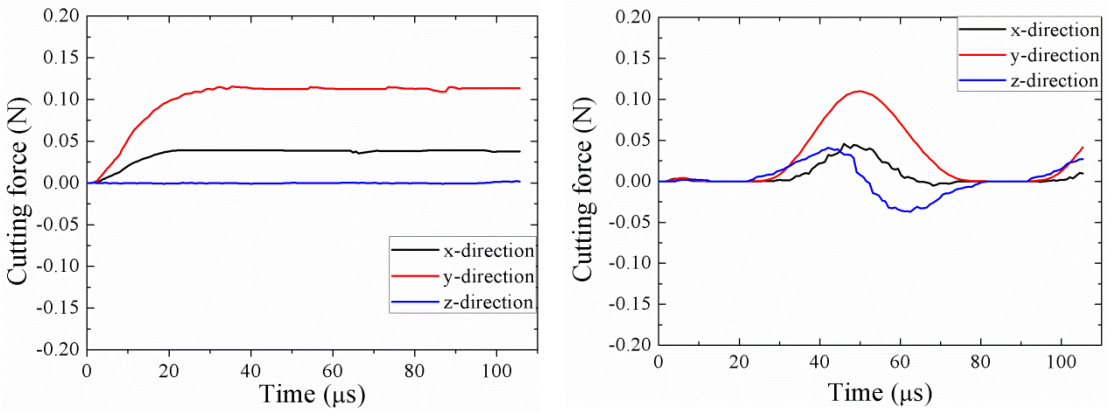

(a) Cutting force in CS (b) Cutting force in UAS

Fig. 5.19 Cutting force in the scratching process in the CS and UAS at a_e=0.07μm.

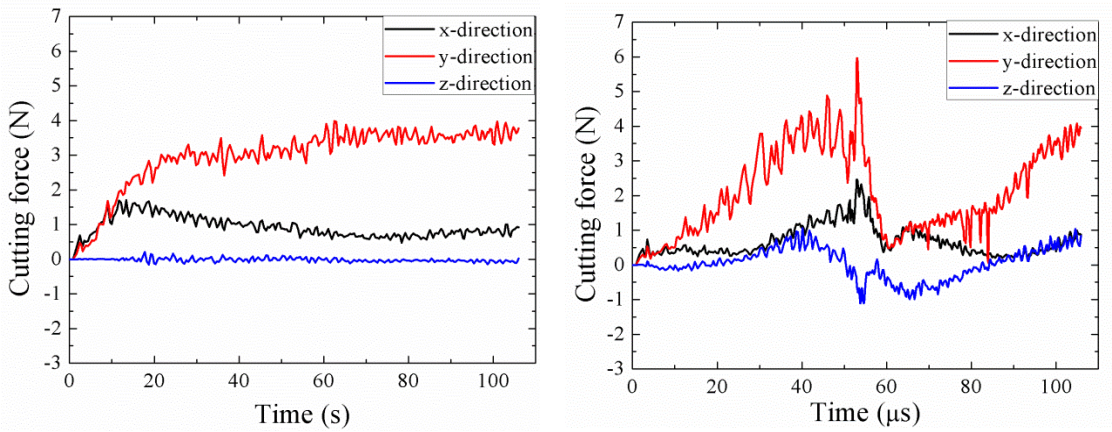

(a) Cutting force in CS (b) Cutting force in UAS

Fig. 5.20 Cutting force in the scratching process in the CS and UAS at a_e=2μm.

5.6.2 Material removal process

Figs. 5.21 describes the chip topographies and material deformations in the CS and UAS at the a_e=0.07μm and a_e=2μm viewed from top. In the case of a_e=0.07μm, it is found that the material was not removed both in CS and UAS, meaning that only plastic deformation occurred. Meanwhile, the scratching in the CS is continuous while in the UAS is intermittent (Fig. 5.21 (a) and 5.21 (b)). These results are consistent with those obtained in the experiments (Figs. 5.8 and 5.9). Turing to a_e=2μm, the deformation fields in the two lateral sides of the groove appear straight in the CS test and serrated in the UAS test (Fig. 5.21 (c) and 5.21 (d)). These findings also agree with the experimental results. Accordingly, the validity of the simulation model is confirmed.

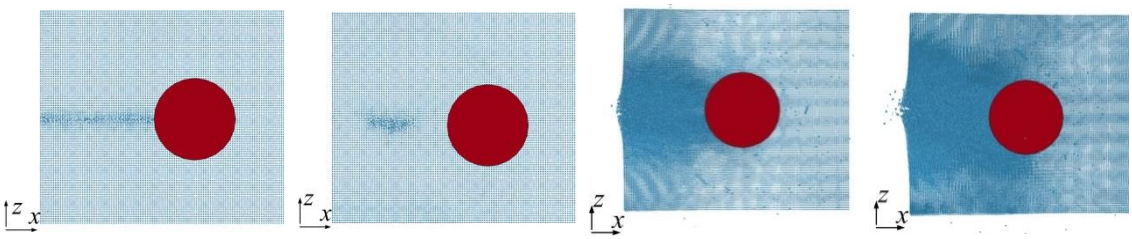

(a) a_e=0.07μm, CS (b)a_e=0.07μm,UAS (c) a_e=2μm, CS (d) a_e=2μm, UAS

Fig. 5.21 Material deformation behavior at a_e=0.07μm and a_e=2μm when time=105μs.

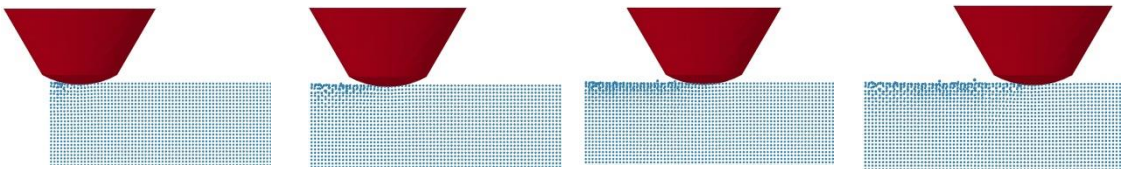

(a) 17.5μs, CS (b) 35μs, CS (c) 52.4μs, CS (d) 69.9μs, CS

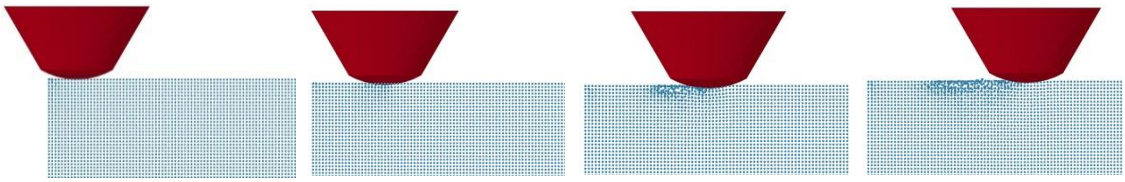

(e) 17.5μs, UAS (f) 35μs, UAS (g) 52.4μs, UAS (h) 69.9μs, UAS

Fig. 5.22 State of workpiece deformation at different times during the scratching process in the UAS and CS tests at a_e=0.07μm.

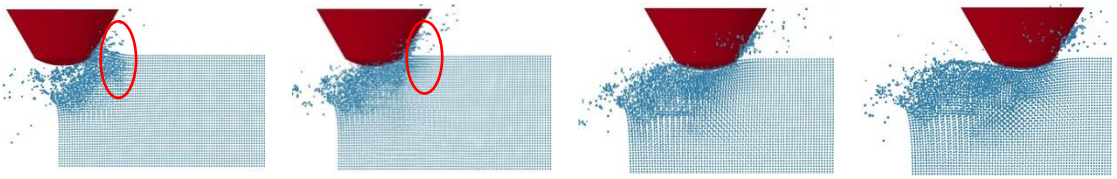

(a) 17.5μs, CS (b) 35μs, CS (c) 52.4μs, CS (d) 69.9μs, CS

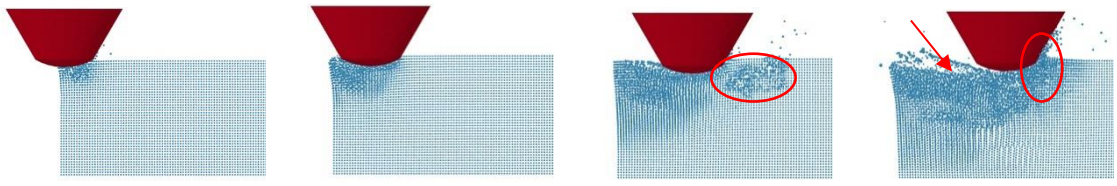

(e) 17.5μs, UAS (f) 35μs, UAS (g) 52.4μs, UAS (h) 69.9μs, UAS

Fig. 5.23 State of workpiece deformation at different times during the scratching process in the UAS and CS tests at a_e=2μm.

To thoroughly understand the material deformation process in the UAS, the workpiece is sliced along the cutting direction of the grain and then compared with that in the CS. The material deformations at time 1/4T = 17.5μs (the period of UV T = 69.9μs), 2/4T = 35.0μs, 3/4 T = 52.4μs, and T = 69.9μs in the UAS, compared with those in the CS, are investigated. Figs. 5.22 and 5.23 show the state of workpiece deformation at different times during the scratching process in the UAS and CS at a_e=0.07μm and a_e=2μm, respectively. With the advancement of the grain, a number of features can be distinguished in the scratching procedure.

In the case of a_e=0.07μm, given the large negative rake angle, the resultant force points to the front surface of and under the grain [26]. As a result, deformation of the workpiece appears on the front surface of and under the grain not only under high compressive stress but also under the action of shear stress (Figs. 5.22(a)-5.22(d)) [7]. But the material is not removed and there is only elastic-plastic deformation can be observed in the CS process, suggesting that the material removal behavior at this depth of cut is deformation and/or ductile removal due to the insufficient compressive stress and shear stress to remove the material. Similar to that in CS, the elastic-plastic deformation also can be observed on the front surface of and under the abrasive grain in UAS (Fig. 5.22(e)-5.22(h)). Meanwhile, it is found that the deformation area is un-continuous. This is because that, as the ultrasonic vibrates in y-direction and its amplitude is larger than the a_e, the grain moves upward in the +y-direction over the period of 0μs to 17.5μs and reaches its highest position in the y-direction, resulting in the grain lifts off completely at 17.5μs (Fig. 5.22(e)); while over the period of 17.5μs to 52.4μs, the grain moves downward in the -y-direction and reaches the deepest depth at 52.4μs, resulting in the grain penetrates into the workpiece (Figs. 5.22(f) and 5.22(g)); Over the period of 52.4μs to 69.9μs, the grain moves upward in the +y-direction and reaches the position same as that in the CS test at 69.9μs (Fig. 5.22(h)). Thus, it is concluded that, due to the UV of the grain in y-direction, the grain depth of cut periodically changes in UAS, eventually leading to the formation of the un-continuous deformation area. The reason why the forces change in an

un-continuous pattern, as previously shown in Fig. 4(b), is ascribed to this.

Turning to a_e=2μm, under the co-action of compressive stress and shear stress, material deformation and dislocation occur, and the material is removed as chips from the front surface of the grain and underneath the grain at 17.5μs in CS (Fig. 5.23(a)). At 35μs, more chips form on the front surface of the grain in the CS compared with those forming at 17.5 μs (see Fig. 5.23(b)). This result can be attributed to the increase in both compressive stress and shear stress. Furthermore, the material deformation area on the front surface of the grain (as indicated by the ellipse in Fig. 5.23(b)) at 35 μs is smaller than that at 17.5 μs (as indicated by the ellipse in Fig. 5.23(a)). This result is brought about by the depth of cut starting from 2μm and not from 0μm at 0μs in this simulation, leading to the impact of the grain on the workpiece at the beginning of the cutting action. The force in *x*-direction is bigger at 17.5μs than any others time as shown in Fig. 5.23(a) may be attributed to the influence of the impact. At 52.4 (Fig. 5.23(c)) and 69.9μs (Fig. 5.23(d)), material deformations in the CS are almost the same as that at 35μs.

In the UAS, no chip can be observed on the front surface of the grain at 17.5μs (Fig. 5.23(e)), mainly because the grain reaches its highest position in the *y*-direction at 17.5μs as mentioned above, resulting in the lowest depth of cut, which causes low compressive stress and shear stress [7]. As a result, the material removed in an elastic plastic mode at 17.5μs. With the continuous advancement of the grain, the grain cuts into the workpiece completely at 35μs. Although the depth of cut in the UAS is the same as that in the CS test, little chips appear on the front surface of the grain in the UAS likely because the compressive stress and shear stress are just beginning to reach the chip formation threshold (Fig. 5.23(f)). At 52.4μs, material deformation in the UAS (Fig. 5.23(g)) is quite different from that at 35μs (Fig. 5.23 (f)) and 17.5μs (Fig. 5.23(d)) as well as from that in the CS (Fig. 5.22 (c)). Brittle fracture can be observed on the front surface of and under the grain (as indicated by the ellipse in Fig. 5.23(g)). These phenomena are absent in the CS perhaps because of the impact arising from the UV against the workpiece in the *y*- and *z*-directions, i.e., the oblique impact of the grain against the workpiece in the *y*- and *z*-directions. Under the co-action of the

impact and the cutting at the grain tip on the machined surface, the material is removed, which can be considered as the main material removal mechanism in the UAS. At 69.9 μs, the material deformation area on the front surface of the grain in the UAS (as marked in Fig. 5.23(h)) is bigger than that in the CS test. This result is attributable to the influence of the impact of the grain on the workpiece at 35μs to 52.4μs.

5.6.3 Scratching-induced stress

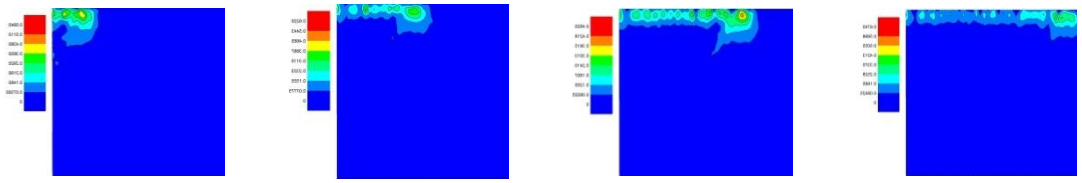

(a) 17.5μs, CS (b) 35μs, CS (c) 52.4μs, CS (d) 69.9μs, CS

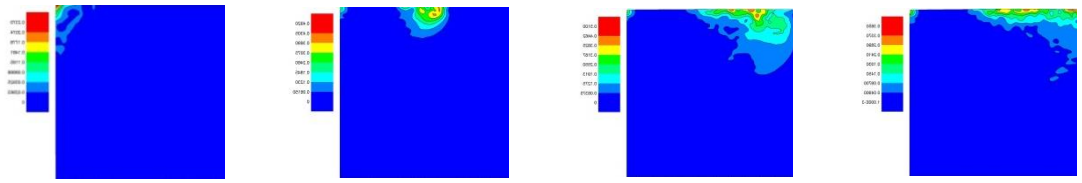

(e)17.5μs, UAS (f) 35μs, UAS (g) 52.4μs, UAS (h) 69.9μs, UAS

Fig. 5.24 Effective stress distribution on the cross surface at a_e=0.07μm.

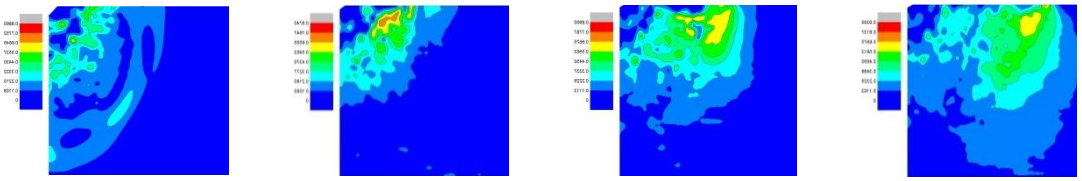

(a)17.5μs, CS (b) 35μs, CS (c) 52.4μs, CS (d) 69.9μs, CS

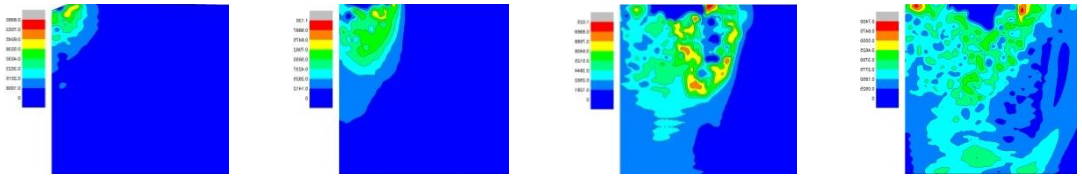

(e)17.5μs, UAS (f) 35μs, UAS (g) 52.4μs, UAS (h) 69.9μs, UAS

Fig. 5.25 Effective stress distribution on the cross surface at a_e=2μm.

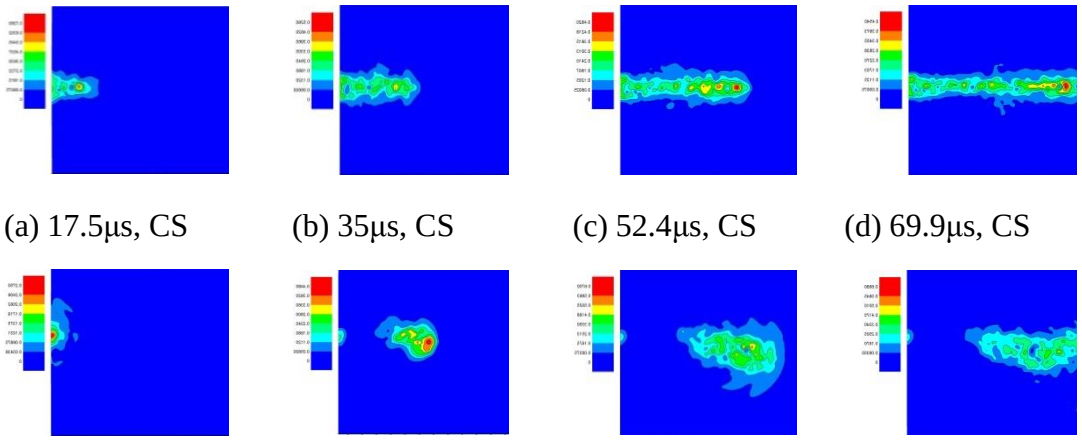

(a) 17.5μs, CS (b) 35μs, CS (c) 52.4μs, CS (d) 69.9μs, CS

(e) 17.5μs, UAS (f) 35μs, UAS (g) 52.4μs, UAS (h) 69.9μs, UAS

Fig. 5.26 Effective stress distribution on the top surface at a_e=0.07μm.

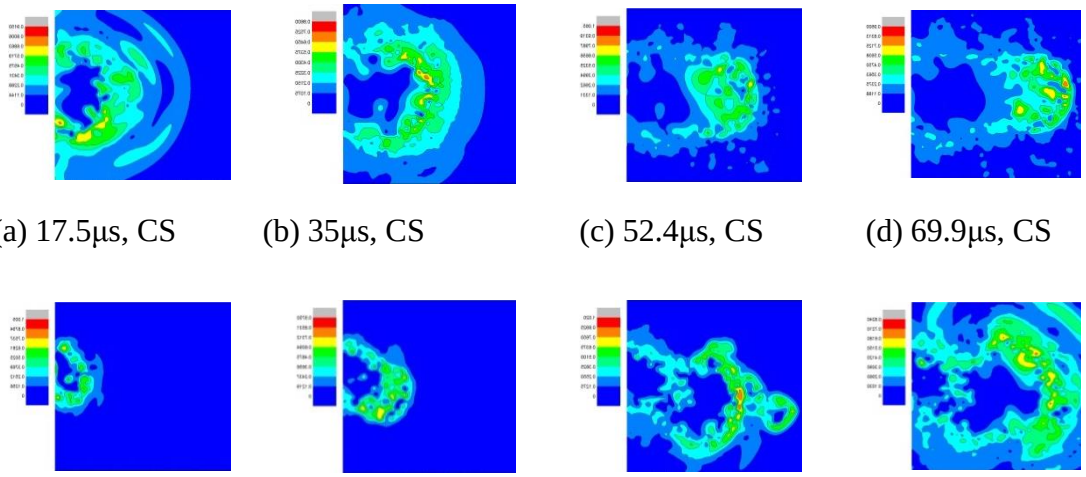

(a) 17.5μs, CS (b) 35μs, CS (c) 52.4μs, CS (d) 69.9μs, CS

(e) 17.5μs, UAS (f) 35μs, UAS (g) 52.4μs, UAS (h) 69.9μs, UAS

Fig. 5.27 Effective stress distribution on the top surface at a_e=2μm.

Knowledge of stress states during the cutting process is key to understanding material removal mechanism [27]. The effective stress field on the cross surface along the cutting direction and that on the top surface during the UAS and CS processes were investigated.

When the grain is cutting into the workpiece, considerable stress is generated in the area around the grain and in the subsurface underneath the grain [7]. In the CS process, the stress fields are basically stabilized after the grain cuts entirely into the workpiece both in the cross surface and the top surface (Figs. 5.24-5.25) both at

a_e=0.07μm and a_e=2μm. These results indicate that the deformation fields are basically stabilized in the CS process after tool cuts entirely into the workpiece. However, the stress fields are wider at 17.5μs and 35μs in the cross surface (see Figs. 5.25(a) and 5.25(b)) and in the top surface (see Figs. 5.25(a) and 5.25(b)) compared with that at other times because of the impact of the grain on the workpiece.

Turing to the UAS process, it is observed that the stress fields are un-continuous at a_e=0.07μm (Figs. 5.24 and 5.26), owing to the ultrasonic vibrates in *y*-direction and its amplitude is larger than the a_e. Further, it is also observed that the stress fields on both surfaces suddenly expand further at 52.4μs (Figs. 5.24(g) and 5.26(g)) and also become wider at 69.9μs than those in the CS process (compare Figs. 5.26(c) and 5.26(g), and Figs. 5.27(c) and 5.27(g)). These are attributed to the impact arising from the UV against the workpiece in the *y*- and *z*-directions. Shifting the attention to a_e=2μm, the stress fields in the cross and top surfaces at 17.5 (Fig. 5.25(e)) and 35μs (Fig. 5.25(f)) are smaller compared with those in the CS process because of the depth of cut is lower than that in CS as mentioned in section 4.2. However, the stress fields on both surfaces suddenly expand further at 52.4μs ((Fig. 5.25(g))) compared with those at 17.5 and 35μs, which are also because of the impact arising from the UV against the workpiece in the y- and z-directions. As the cutting tool continues to move forward, the stress fields on both surfaces at 69.9μs become wider than those at 52.4μs and those in the CS process and at 69.9μs. Therefore, the deformation field is deeper and wider on both the cross and top surfaces.

5.7 Summary

To comprehend the material removal mechanism in the ultrasonic-assisted grinding of SiC ceramics, an ultrasonic-assisted scratching (UAS) test involving SiC ceramics specimen was performed on an in-house-produced experimental setup. The material removal characteristics in the UAS test were compared to the conventional scratching (CS) test without ultrasonic vibration. The results and conclusion can be summarized as follows:

(1) Both in CS and UAS processes, three types of material deformation/fracture are successively generated along the scratching trace: the ductile removal mode, ductile–brittle transition mode, and brittle removal mode; the scratching groove formed appears straight in the CS process while it is sinusoidal in the UAS process.

(2) Depending on the actual depth of cut, there are two scratching modes in the UAS process: one is an intermittent mode and the other is a continuous mode. The UV in *y*-direction strongly contributes to the material removal, whereas the UV in *z*-direction only results in variation of the cutting trace and hardly contributes to the material removal in the UAS process.

(3) Comparing the theoretical depths with experimental ones shows that experimental depth is smaller than the theoretical one in CS, whereas the mean value of the experimental depth is close to the mean value of the theoretical one in UAS. This means that the stiffness of experiment setup is improved by UV assistance.

(4) The mean groove depth in the UAS process is much bigger than the CS process over the entire length of the groove, indicating that the cutting ability of the tool was significantly improved by the assistance of the UV. Furthermore, the critical depth of cut is increased from 0.08 μm in CS to 0.125 μm in UAS, which is an increase of 56.25%. This is likely because the fracture toughness in the UAS process is higher than that in the CS process.

(5) Due to the abrupt variation of the scratching forces, the forces heavily vary but the periods are different from that of the UV of the tool when the material removal is in brittle mode.

(6) The mean values of the f_n/S and the force ratio f_n/f_t in UAS are smaller than those in CS, owing to the improved cutting efficiency and ability in UAS.

(7) Investigations of the stress distribution on the cross and top surfaces along the cutting direction show that the stress fields on both surfaces become wider in the UAS process than in the CS process because of the impact arising from the UV.

(8) The deformation of the SiC ceramics in the UAS process is equivalent to the combined effect of dynamic cutting with a tangential scratching velocity and UV.

The UV impacted the diamond tool, leading to the impact of the tool on the workpiece. Upon impact of the tool on the workpiece, the stress field spreads from the impact site, leading to the expansion of stresses. Such expansion is the main factor that induces deep scratching depths and increases the sizes of the radial and lateral cracks.

Reference

[1] Anderson, D. ; Warkentin, A. ; Bauer, R. Experimental and numerical investigations of single abrasive-grain cutting. *Int. J. Mach. Tools Manuf.* **2011**, *51* (12), 898-910.

[2] Zhang, C. ; Feng, P. ; Zhang, J. Ultrasonic vibration-assisted scratch-induced characteristics o f C-plane sapphire with a spherical indenter. *Int. J. Mach. Tools Manuf.* **2013**, *64*, 38-48.

[3] Gua, W. ; Yao, Z. ; Liang, X. Material removal of optical glass BK7 during single and double scratch tests. *Wear* **2011**, *270* (3-4), 241-246.

[4] Huang, L. ; Bonifacio, C. ; Song, D. ; Benthem, K. V. ; Mukherjee, A. K. ; Schoenung, J. M. Investigation into the microstructure evolution caused by nanoscratch-induced room temperature deformation in M-plane sapphire. *Acta Mater.* **2011**, *59* (13), 5181-5193.

[5] Klecka, M. ; Subhash, G. Grain size dependence of scratch-induced damage in alumina ceramics. *Wear* **2008**, *265* (5-6), 612-619.

[6] Liang, Z. ; Wang, X. ; Wu, Y. ; Xie, L. ; Jiao, L. ; Zhao, W. Experimental study on brittle–ductile transition in elliptical ultrasonic assisted grinding (EUAG) of monocrystal sapphire using single diamond abrasive grain. *International Journal of Machine Tools and Manufacture* **2013**, *71* (0), 41-51.

[7] Chuang, T.-j. ; Jahanmir, S. ; Tang, H. C. Finite element simulation of straight plunge grinding for advanced ceramics. *J. Eur. Ceram. Soc.* **2003**, *23* (10), 1723-1733.

[8] Ghosh, D. ; Subhash, G. ; Radhakrishnan, R. ; Sudarshan, T. S. Scratch-induced microplasticity and microcracking in zirconium diboride–silicon carbide composite

Acta Mater. **2008**, *56* (13), 3011-3022.

[9] Z Fawaz, W. Z., K Behdinan Numerical simulation of normal and oblique ballistic impact on ceramic composite armours *Compos. Struct*, **2004**, *63* (3-4), 387-395.

[10] Lee, M. ; Kim, E. Y. ; Yoo, Y. H. Simulation of high speed impact into ceramic composite systems using cohesive-law fracture model. *Int. J. Impact Eng.* **2008**, *35* (12), 1636-1641.

[11] Kanel, G. I. ; Zaretsky, E. B. ; Rajendran, A. M. ; Razorenov, S. V. ; Savinykh, A. S. ; Paris, V. Search for conditions of compressive fracture of hard brittle ceramics at impact loading. *Int. J. Plast.* **2009**, *25* (4), 649-670.

[12] Shimada, K. ; Takeishi, T. ; Nobuhito, Y. ; Jiwang, Y. ; Tsunemoto, K. Ultrasonic-assisted micro-grinding with electroplated diamond wheels 2nd report: Effect of ultrasonic vibration on workpiece removal in grinding wheel end. *Jpn. Soc. Abras. Technol.* **2010**, *54* (1), 37-40.

[13] Bifano, T. G. ; Fawcett, S. C. Specific grinding energy as an in-process control variable for ductile-regime grinding. *Precision Engineering* **1991**, *13* (4), 256-262.

[14] Zarepour, H. ; Yeo, S. H. Predictive modeling of material removal modes in micro ultrasonic machining. *International Journal of Machine Tools and Manufacture* **2012**, *62*, 13-23.

[15] Slikkerveer, P. J. ; Bouten, P. C. P. ; Veld, F. H. i. t. ; Scholten, H. Erosion and damage by sharp particles. *Wear* **1998**, *217* (2), 237-250.

[16] Arif, M. ; Xinquan, Z. ; Rahman, M. ; Kumar, S. A predictive model of the critical undeformed chip thickness for ductile-brittle transition in nano-machining of brittle materials. *International Journal of Machine Tools and Manufacture* **2013**, *64*, 114-122.

[17] Arif, M. ; Rahman1, M. ; San, W. Y. Analytical model to determine the critical feed per edge for ductile-brittle transition in milling process of brittle materials. *International Journal of Machine Tools and Manufacture* **2011**, *51* (3), 170-181.

[18] Marinescu, I. D. ; Hitchiner, M. ; Uhlmann, E. ; Rowe, W. B. ; Inasaki, I., Handbook of machining with grinding wheels, CRC Press, 2006.

[19] Liang, Z. ; Wang, X. ; Wu, Y. ; Xie, L. ; Liu, Z. ; Zhao, W. An investigation on

wear mechanism of resin-bonded diamond wheel in Elliptical Ultrasonic Assisted Grinding (EUAG) of monocrystal sapphire. *J. Mater. Process. Technol.* **2012**, *212* (4), 868-876.

[20] Lucy, L. B. A numerical approach to the testing of the fission hypothesis. *The Astronomical Journal* **1977**, *82*, 1013-1024.

[21] Gingold, R. A. ; Monaghan, J. J. Smoothed particle hydrodynamics -Theory and application to non-spherical stars. *Monthly Notices of the Royal Astronomical Society* **1977**, *181* (375-389).

[22] Limido, J. ; Espinosa, C. ; Salaün, M. ; Lacome, J.-L. SPH method applied to high speed cutting modelling. *International journal of mechanical sciences* **2007**, *49* (7), 898-908.

[23] Cronin, D. S. ; Bui, K. ; Kaufmann, C. ; McIntosh, G. ; Berstad, T., Implementation and validation of the Johnson-Holmquist ceramic material model in LS-DYNA, in: 4th European LS-dyna users conference, 2003, pp. 47-60.

[24] Wang, Y. F. ; Yang, Z. G. Finite element model of erosive wear on ductile and brittle materials. *Wear* **2008**, *265* (5-6), 871-878.

[25] Anderson, D. ; Warkentin, A. ; Bauer, R. Experimental and numerical investigations of single abrasive-grain cutting. *International Journal of Machine Tools and Manufacture* **2011**, *51* (12), 898-910.

[26] Lin, B. ; Yu, S. Y. ; Wang, S. X. An experimental study on molecular dynamics simulation in nanometer grinding. *J. Mater. Process. Technol.* **2003**, *138* (1-3), 484-488.

[27] Zhang, C. ; Feng, P. ; Zhang, J. Ultrasonic vibration-assisted scratch-induced characteristics of C-plane sapphire with a spherical indenter. *International Journal of Machine Tools and Manufacture* **2013**, *64*, 38-48.

Chapter 6 Approaches to high accuracy internal grinding of SiC ceramics

In chapter 3-5, fundamental Machining Characteristics of UAIG of SiC Ceramics, grinding force reduction mechanism and material removal mechanism were observed. In this chapter, in order to highly efficient and ultra-fine internal grinding of SiC ceramics, the probability of internal grinding of SiC ceramics in ductile mode is observed. In addition, grinding experiments are operated to extend UAIG method to industrial application.

6.1 Internal grinding of SiC ceramics in ductile mode

In order to observe the ductile-brittle transition in internal grinding of SiC ceramics, 4 rounds of grinding tests were performed under different sets of experiment conditions as shown in Table 6.1.

Table 6.1 Experiment conditions for observation of ductile-brittle transition in internal grinding

NO.	Wheel NO.	Workpiece rotational speed n_w (rpm)	Wheel rotational speed n_g (rpm)	Stock removal (μm)	Feed rate V_c(μm/min)	Ultrasonic Amplitude (μm)
1	SD400P100M	300	4000	50	10	0/4
2	SD1000P100M	300	3000	50	10	0/4
3	SD1000P100M	300	4000	50	10	0/4
4	SD3000P100M	300	4000	50	10	0/4

In grinding, the maximum cutting depth of a single grain g_m is determined by [1]:

$$g_m = 2a\frac{V_w}{V_g}\sqrt{\frac{\Delta}{D_e}} \tag{1}$$

Where a is successive cutting edge spacing, V_w is workpiece tangential speed, V_g is grinding wheel tangential speed, Δ is grinding wheel depth of cut, and D_e is equivalent wheel diameter. In internal grinding, D_e can be written by [1]：

$$D_e = \frac{D_g}{1-D_g/D_w} \tag{2}$$

Where D_g is grinding wheel diameter and D_w is workpiece diameter.

successive cutting edge spacing a is determined by [2]：

$$a = 137.9M^{-1.4}\sqrt[3]{\frac{2\pi}{\eta_g}} \tag{3}$$

Where M is is the grit number, η_g is the density of the wheel, (%).

Table 6.2 shows the gm obtained from Eq. (1)-(3) under the condition as shown in table 6.1.

Table 6.2 g_m in different experiment conditions

	No.1	No.2	No.3	No.4
g_m (μm)	0.251μm	0.093μm	0.072μm	0.019μm

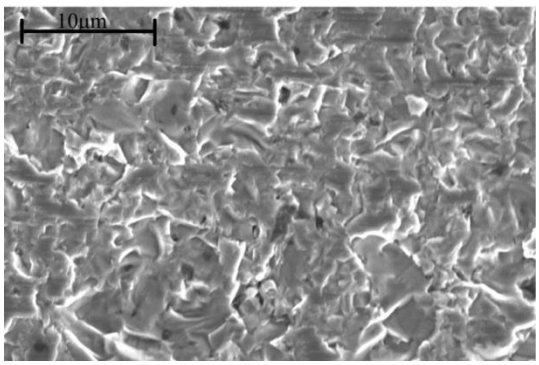

(a) work-surface integrity by CIG at g_m=0.251μm

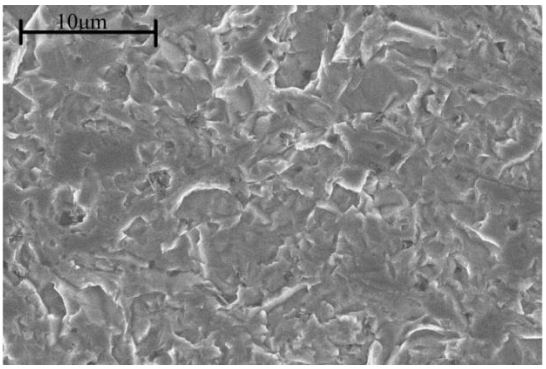

(b) work-surface integrity by UAIG at g_m =0.251μm

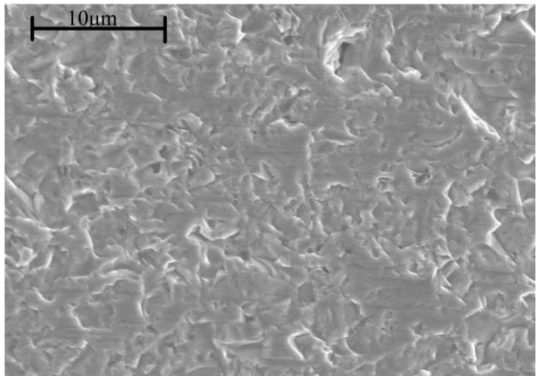

(c) work-surface integrity by CIG at g_m=0.093μm

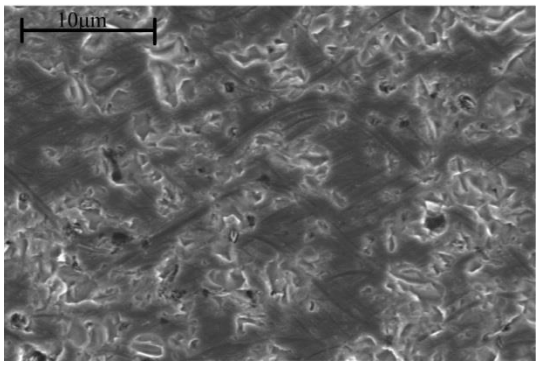

(d) work-surface integrity by UAIG at g_m=0.093μm

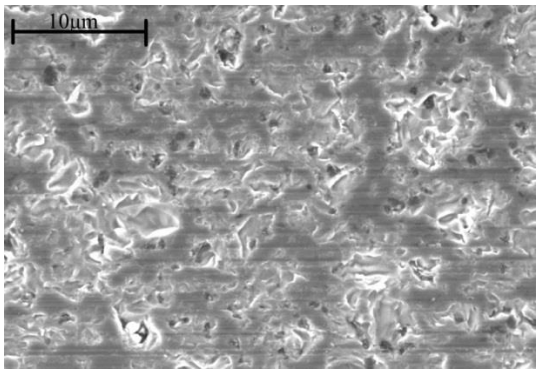

(e) work-surface integrity by CIG at g_m=0.072μm

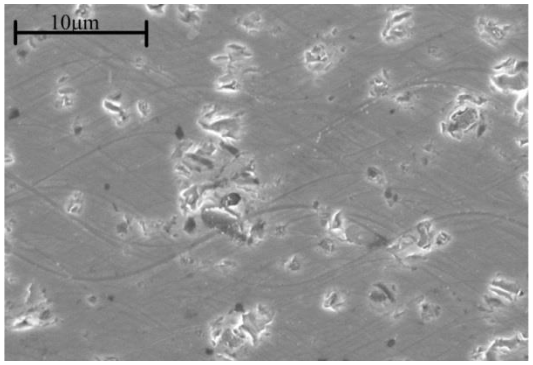

(f) work-surface integrity by UAIG at g_m=0.072μm

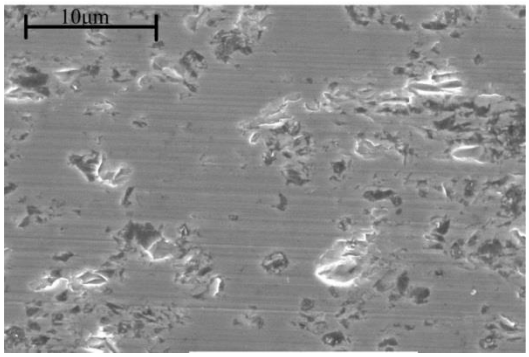

(g) work-surface integrity by CIG at g_m=0.019μm

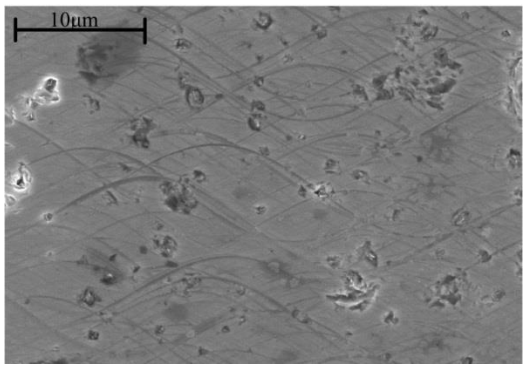

(h) work-surface integrity by UAIG at g_m=0.019μm

Fig. 6.1 SEM images of work-surface by CIG and UAIG at different experiment conditions

Fig. 6.1 shows SEM images of workpiece surface by CIG and UAIG at different experiment conditions. It is found from Fig. 6.1(a) and 6.1(b) that brittle fractures and cracks can be clearly observed in the work-surface both in CIG and UAIG, suggesting

that the brittle fracture mode was the main material removal behavior when g_m=0.251μm due to the cooperative action of the high compressive stress and shear stress [3]. When g_m=0.093μm, obvious macro-brittle fractures and cracks were also generated in work-surface formed by CIG (Fig. 6.1(c)). Different to that in CIG, it is found that smooth surface besides macro-brittle fractures and cracks are formed in the work-surface formed by UAIG, indicating that indicating that a ductile–brittle transition occurred when g_m=0.093μm (Fig. 6.1(d)). However, as observed in Fig. 6.1(e), smooth surface besides macro-brittle fractures and cracks are formed in the work-surface formed by CIG when g_m=0.072μm. By contrast, although some cracks can be observed in the work-surface, almost of the work-surface was smooth in UAIG when g_m=0.072μm (Fig. 6.1(f)), indicating that the grinding mode was predominantly ductile. Shifting attention to Fig. 6.1(g) and 6.1(h), it is found that almost of the work-surface was smooth both in CIG and UAIG, suggesting that the ductile mode was the main material removal behavior when g_m=0.019μm.

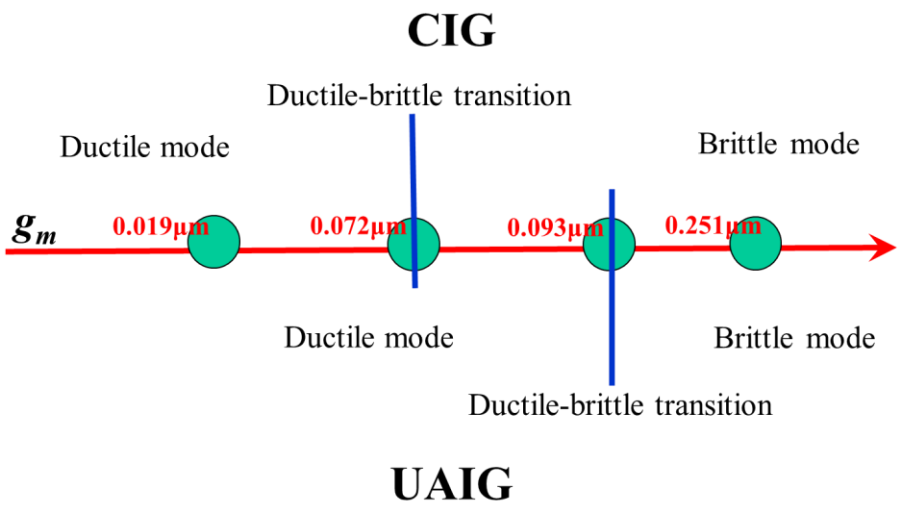

Fig. 6.2 Illustration of ductile-brittle transition in CIG and UAIG

Thus, it is concluded that ductile-brittle transition occurs at g_m=0.072μm in CIG while at g_m=0.093μm in UAIG. This means that critical depth of cut (ductile-brittle transition depth) is increased in UAIG compared with that in

CIG, meaning that ductile mode grinding is easily achieved in UAIG (Fig. 6.2). This findings almost agree with those in scratching tests as shown in chapter 5.

6.2. Grinding efficiency

Understanding physical processes in grinding operation is necessary for the optimal use of UAIG technology. Generally, material removal efficiency is the result of the physical processes in grinding, thus, material removal volume in internal grinding with assistance of UV and without assistance of UV were observed to evaluate the grinding efficiency.

Fig. 6.5 shows experiment method for evaluating the material removal efficiency. In the grinding process, oscillation stroke is not cover the whole internal surface, thus, radial depth will be formed after grinding. We can know the grinding efficiency by measuring the radial depth.

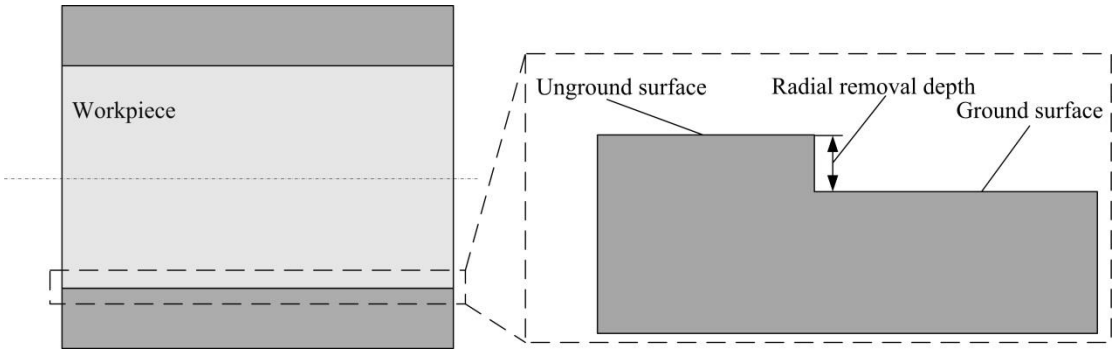

Fig. 6.5 Experiment method for evaluating the material removal efficiency

In order to observe the material removal efficiency in ductile grinding mode and in brittle grinding mode, grinding tests were performed under experiment conditions No.1, No.4 and stock removal=50μm as shown in Table 6.1.

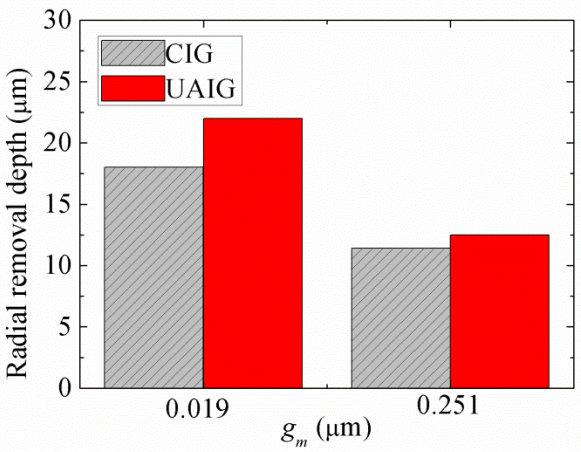

Fig. 6.6 Material removal efficiency in ductile and brittle grinding mode

It is found from Fig. 6.6 that radial removal depth is 12.5μm in UAIG while 11.4μm in CIG at g_m=0.019μm, i.e., a 9.6% increase in ductile grinding mode, whereas radial removal depth is 22μm in UAIG while 18μm in CIG at g_m=0.251μm, i.e., a 22.2% increase in brittle grinding mode. Therefore, it is concluded that the effect of UV on material removal efficiency will be enhanced in brittle grinding mode. In chapter 5, we found that "the difference between the mean values of the groove depths in CS and UAS continue to increase because the groove depth in CS remains shallow over the entire length of the groove, indicating that the cutting ability of the tool was significantly improved by the UV assistance." This means that the UV strongly contributes to the material removal when depth of cut is bigger that of critical depth of cut in the grinding process. This may be the reason the grinding efficiency is higher in brittle grinding mode compared to that in ductile grinding mode in UAIG.

6.3 High accuracy internal grinding of SiC ceramics

In this study, the workpiece is a sleeves mold used for producing aspherical lenses. The ground internal surface of the sleeve should be with high accuracy. The requirements of internal surface accuracy are shown in Table 6.3.

Table 6.3 Accuracy requirements for sleeves mold

Item		Objective
Surface roughness Ra		≤20nm
Form accuracy	Roundness E_r	≤1μm
	Cylindricity E_c	≤3μm

6.3.1 Surface roughness

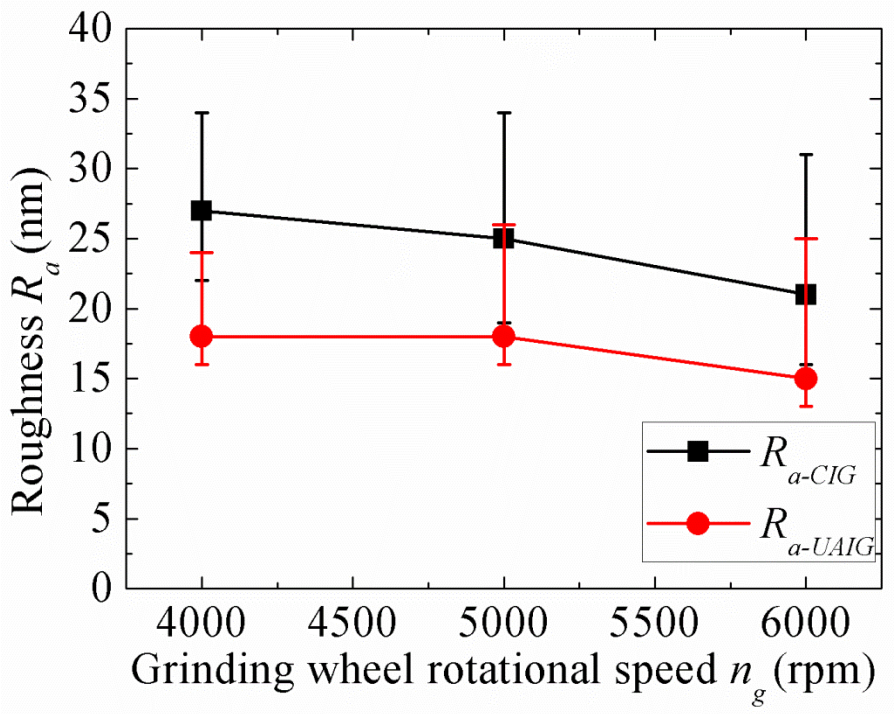

f: 40kHz, *A*:4μm, Grinding wheel: SD3000P100M, V_c: 10μm/min, n_w: 300rpm,

(a) Roughness vs. grinding wheel rotational speed n_g in CIG and UAIG

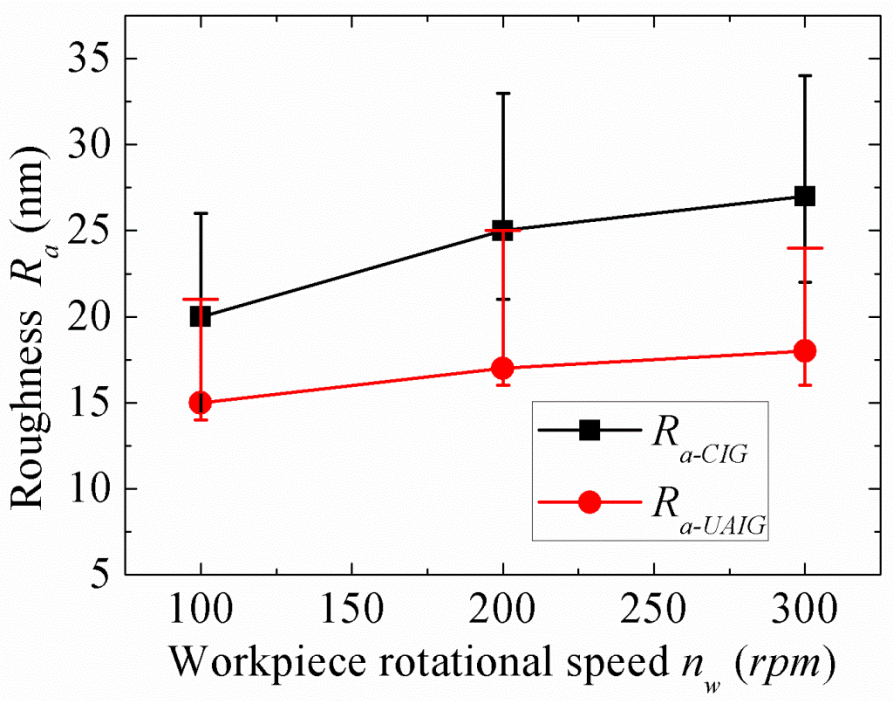

f: 40kHz, *A*:4μm, Grinding wheel: SD3000P100M, n_g: 4000rpm, V_c: 10μm/min

(b) Roughness vs. workpiece rotational speed n_w in CIG and UAIG

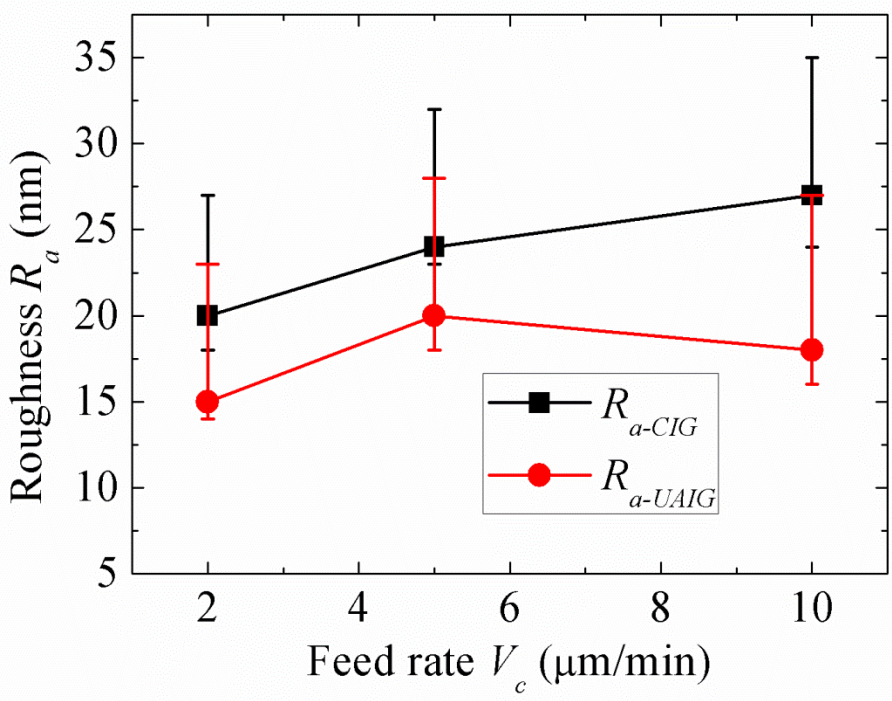

f: 40kHz, *A*:4μm, Grinding wheel: SD3000P100M, n_g: 4000rpm, n_w: 300rpm

(c) Roughness vs. feed rate V_c in CIG and UAIG

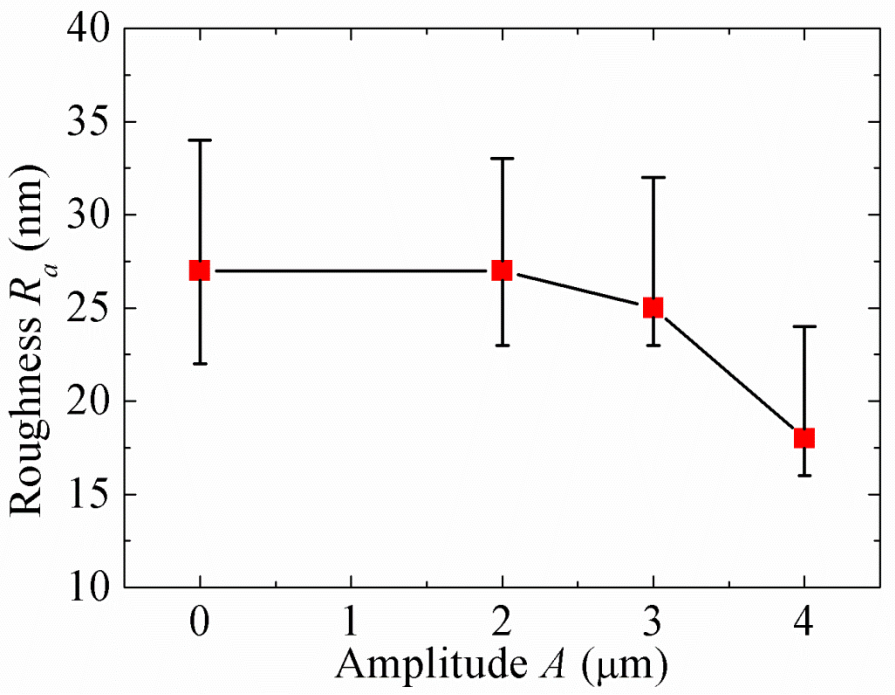

f: 40kHz, Grinding wheel: SD3000P100M, n_g: 4000rpm, V_c: 10μm/min, n_w: 300rpm

(d) Roughness vs. amplitude A in CIG and UAIG

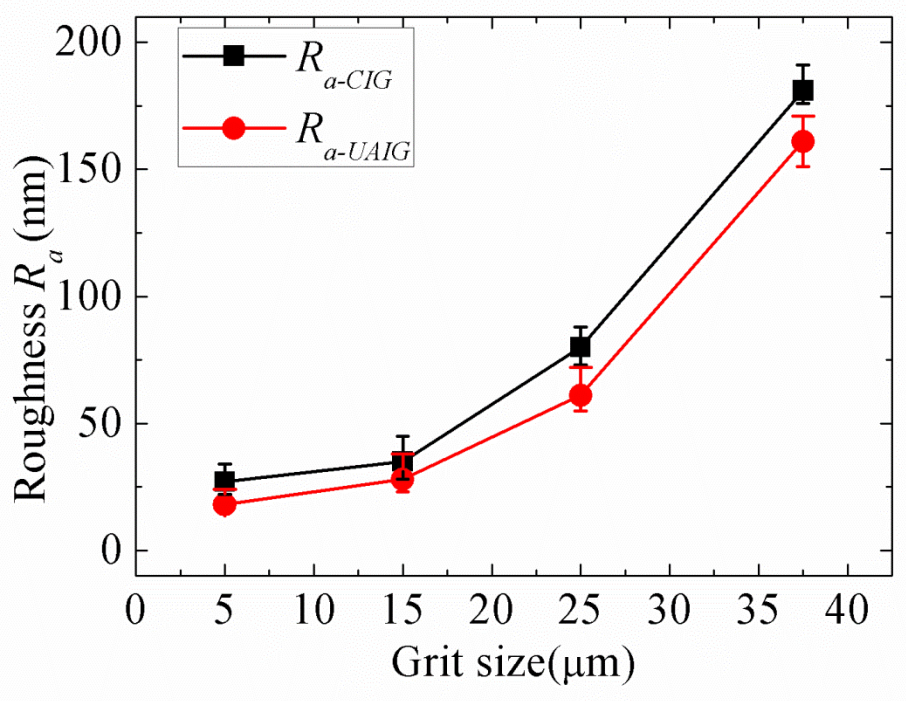

f: 40kHz, A:4μm, n_g: 4000rpm, V_c: 10μm/min, n_w: 300rpm,

(e) Roughness vs. grit size in CIG and UAIG

Fig. 6.5 Roughness vs. grinding parameters in CIG and UAIG

The effect of grinding parameters, namely the workpiece rotational speed n_w, the wheel rotational speed n_g, the wheel infeed rate V_c, grit size and the UV amplitude A, on surface roughness R_a in CIG and UAIG are shown in Fig. 6.5. It is found that both roughness in CIG or in UAIG increase with the increasing of n_g and A, but decrease with the increasing of n_w, V_c and grit size. Furthermore, it is noticed that the roughness R_a in UAIG are significantly smaller than those in CIG, meaning the presence of the UV improves the surface roughness significantly. The improvement of surface quality in UAIG can be considered to be the contribution of the grinding forces reduction [4]. Furthermore, it is concluded from the experiment results that roughness of the ground workpiece obtained by UAIG can agree the accuracy requirement.

6.3.2 Roundness and cylindricity

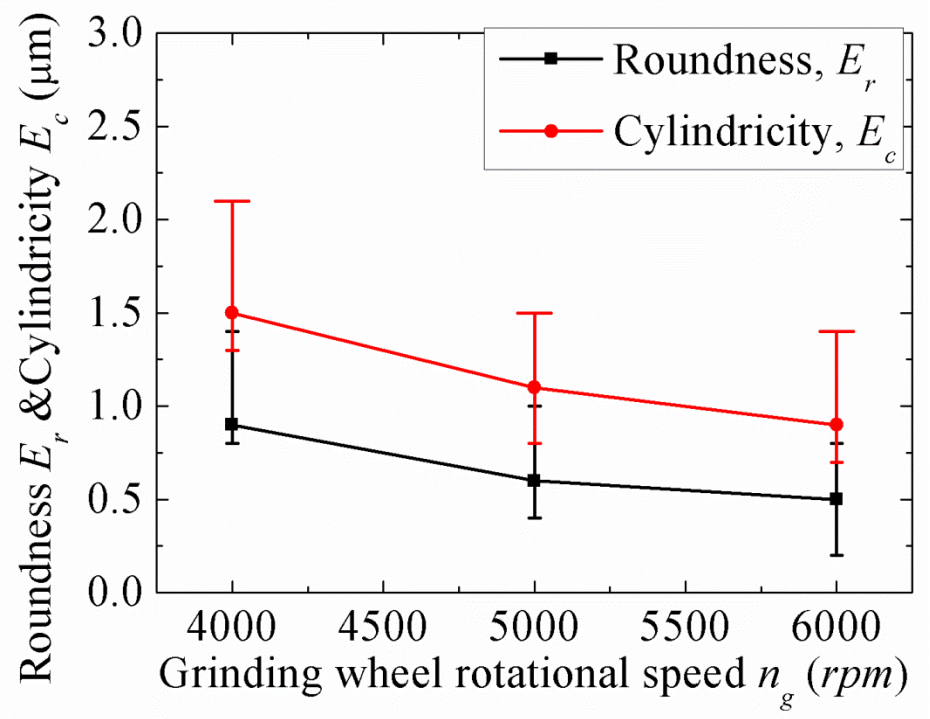

f: 40kHz, A:4μm, Grinding wheel: SD3000P100M, V_c: 10μm/min, n_w: 300rpm,

(a) Roundness E_r and cylindricity E_c vs. grinding wheel rotational speed n_g in UAIG

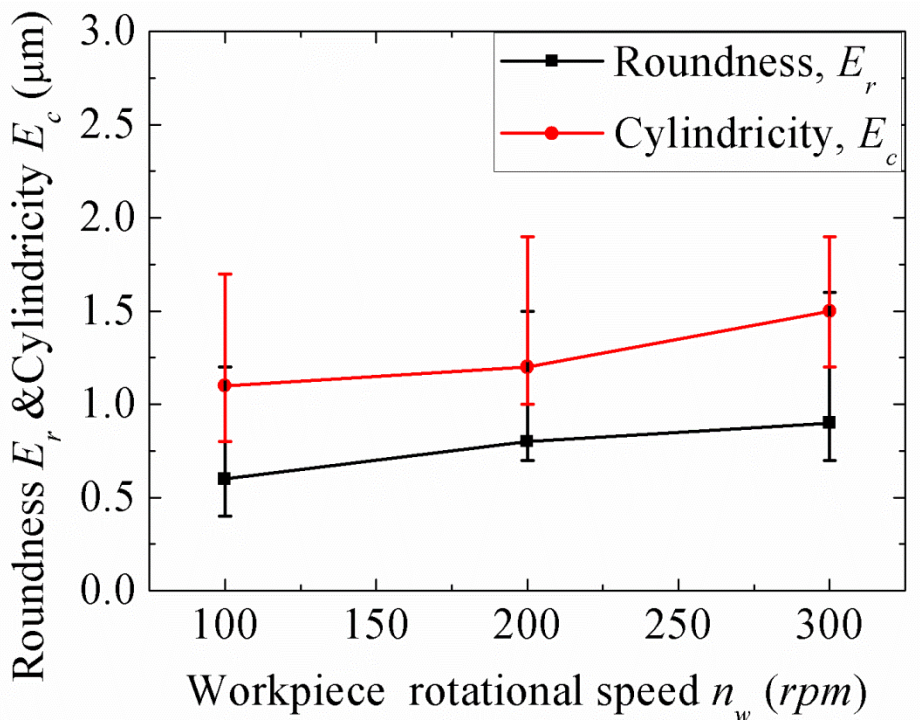

f: 40kHz, *A*:4μm, Grinding wheel: SD3000P100M, n_g: 4000rpm, V_c: 10μm/min

(b) Roundness E_r and cylindricity E_c vs. workpiece rotational speed n_w in UAIG

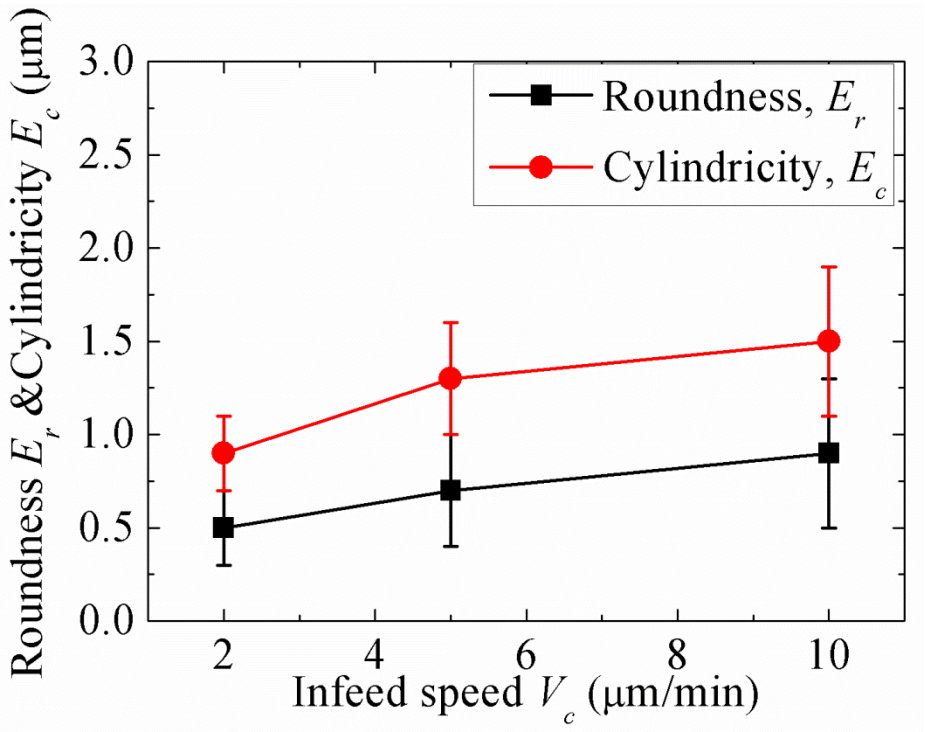

f: 40kHz, *A*:4μm, Grinding wheel: SD3000P100M, n_g: 4000rpm, n_w: 300rpm,

(c) Roundness E_r and cylindricity E_c vs. feed rate V_c in UAIG

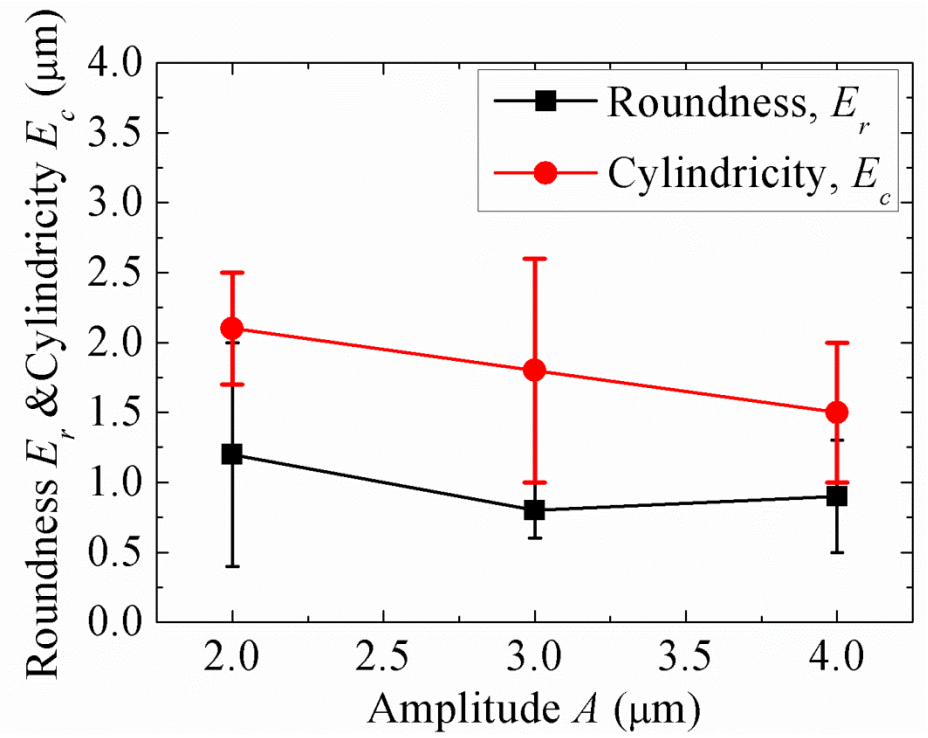

f: 40kHz, Grinding wheel: SD3000P100M, n_g: 4000rpm, V_c: 10μm/min, n_w: 300rpm,

(d) Roundness E_r and cylindricity E_c vs. amplitude A in UAIG

Fig. 6.6 Roundness E_r and cylindricity E_c vs. grinding parameters in CIG and UAIG

The effect of grinding parameters, namely the workpiece rotational speed n_w, the wheel rotational speed n_g, the wheel infeed rate V_c, grit size and the UV amplitude A, on roundness E_r and cylindricity E_c in UAIG are shown in Fig. 6.6. It is found that both roundness E_r and cylindricity E_c in UAIG increase with the decreasing of n_g and A, but increase with the increasing of n_w, V_c. Furthermore, it is concluded from the experiment results that roundness E_r and cylindricity E_c of the ground workpiece obtained by UAIG can agree the accuracy requirement.

6.3.3 Straightness

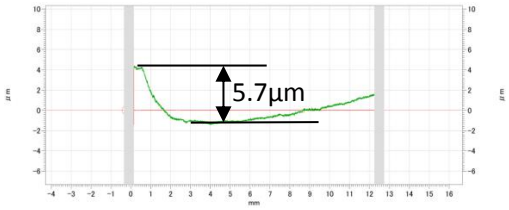

(a) n_w=300rpm, CIG

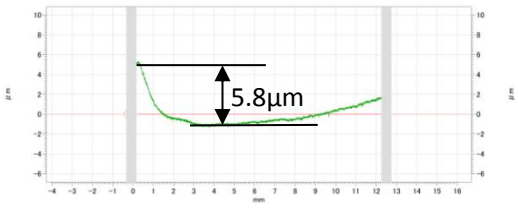

(b) n_w=300rpm, UAIG

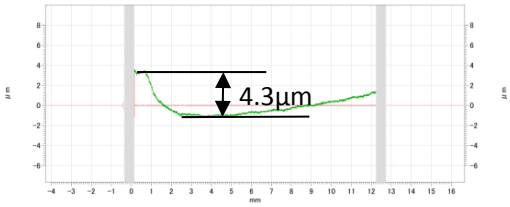

(c) n_w=200rpm, CIG

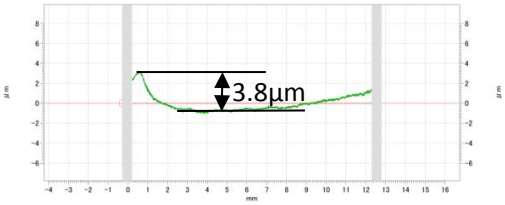

(d) n_w=300rpm, UAIG

(e) n_w=100rpm, CIG

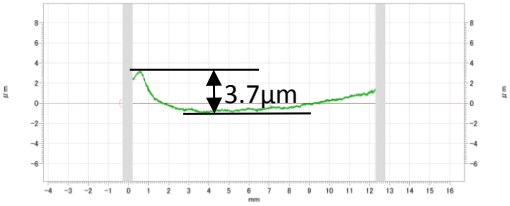

(f) n_w=100rpm, UAIG

f: 40kHz, Grinding wheel: SD3000P100M, n_g: 4000rpm, V_c: 10μm/min, A=44μm, oscillation stroke=12mm, oscillation speed V_{os}=0.1m/min

Fig. 6.7 Straightness vs. workpiece rotational speed n_w in CIG and UAIG

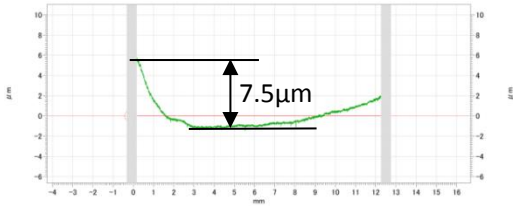

(a) n_g=4000rpm, CIG

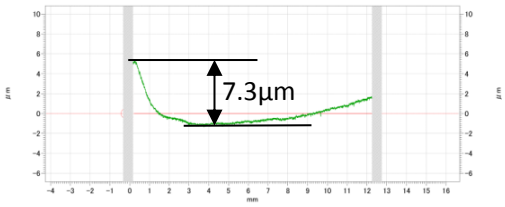

(b) n_g=4000rpm, UAIG

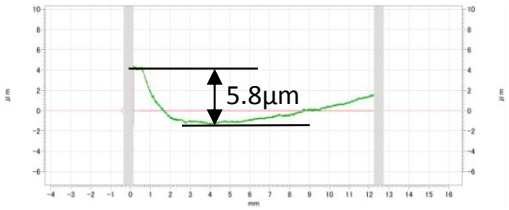

(c) n_g=5000rpm, CIG

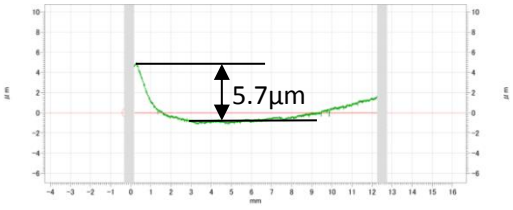

(d) n_g=5000rpm, UAIG

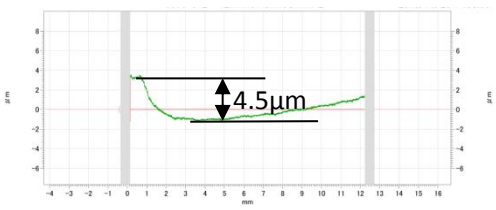

(e) n_g=6000rpm, CIG

(f) n_g=6000rpm, UAIG

f: 40kHz, Grinding wheel: SD3000P100M, V_c: 10μm/min, n_w: 300rpm, oscillation stroke=12mm, oscillation speed V_{os}=0.1m/min

Fig. 6.8 Straightness vs. grinding wheel rotational speed n_g in CIG and UAIG

(a) n_g=10μm/min, CIG

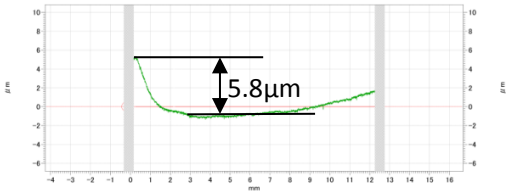

(b) n_g=10μm/min, UAIG

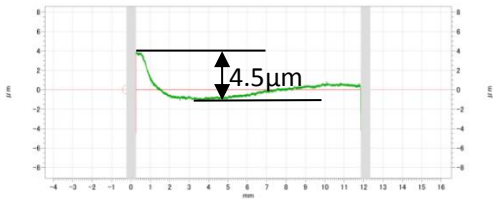

(c) n_g=5μm/min, CIG

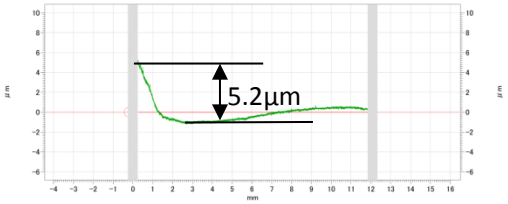

(d) n_g=5μm/min, UAIG

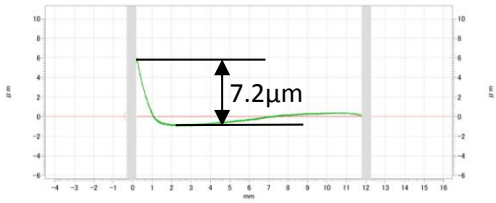

(e) n_g=2μm/min, CIG

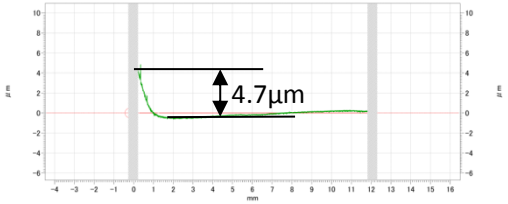

(f) n_g=2μm/min, UAIG

f: 40kHz, Grinding wheel: SD3000P100M, n_w: 300rpm, oscillation stroke=12mm, oscillation speed V_{os}=0.1m/min

Fig. 6.9 Straightness vs. feed rate V_c in CIG and UAIG

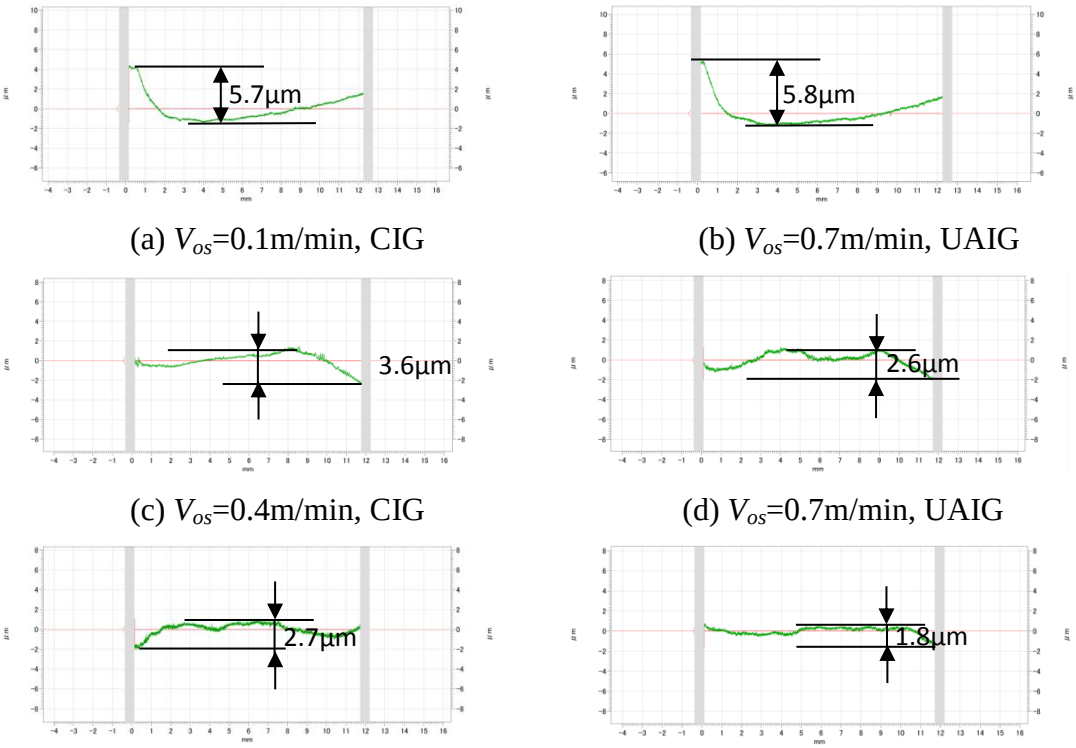

(a) V_{os}=0.1m/min, CIG (b) V_{os}=0.7m/min, UAIG

(c) V_{os}=0.4m/min, CIG (d) V_{os}=0.7m/min, UAIG

(e) V_{os}=0.7m/min, CIG (f) V_{os}=0.7m/min, UAIG

f: 40kHz, Grinding wheel: SD3000P100M, n_w: 300rpm, oscillation stroke=12mm, oscillation speed V_{os}=0.1m/min

Fig. 6.10 Straightness vs. oscillation speed in CIG and UAIG

Figs. 6.7-6.10 shows the comparison of the workpiece straightness after CIG and UAIG with variation of the workpiece rotational speed n_w, the wheel rotational speed n_g, the wheel infeed rate V_c, and oscillation speed V_{os}. It can be found from the figures that the straightness decreases with increasing of the wheel rotational speed n_g and oscillation speed V_{os}, and decreasing of the workpiece rotational speed n_w and the wheel infeed rate V_c. The workpiece rotational speed n_w, the wheel rotational speed n_g, the wheel infeed rate V_c have significantly influence on the improvement of workpiece straightness, whereas oscillation speed V_{os} has significantly influence on workpiece straightness. Especially, the straightness was improved significantly when oscillation speed V_{os} is bigger than 0.4m/min both in CIG and UAIG.

As mention above, in order to agree the accuracy requirement, the experiment condition should be followed as shown in Table 6.4:

Table 6.4 Recommended experiment conditions for accuracy internal grinding

Workpiece rotational speed n_w (rpm)	≤ 300
Wheel rotational speed n_g (rpm)	≥4000
Wheel infeed rate V_c (μm/min)	≤10
Grit size (μm)	≤5
Oscillation speed V_{os} (m/min)	≥0.4
amplitude A (μm)	≥4

6.4 Summary

In this chapter, in order to highly efficient and ultra-fine internal grinding of SiC ceramics, the probability of internal grinding of SiC ceramics in ductile mode and grinding efficiency were observed. The results and conclusion can be summarized as follows:

(1) Critical depth of cut is increased in UAIG compared with that in CIG, meaning that ductile mode grinding is easily achieved in UAIG.

(2) Grinding efficiency is higher in brittle grinding mode compared to that in ductile grinding mode in UAIG.

(3) High accuracy can be achieved by UAIG under the recommended experiment conditions.

Reference

[1] Syoji, K., Grinding manufacturing, Yokendo Press, 2004.

[2] Zhou, X. ; Xi, F. Modeling and predicting surface roughness of the grinding process. *International Journal of Machine Tools and Manufacture* **2002**, *42* (8), 969-977.

[3] Ghosh, D. ; Subhash, G. ; Radhakrishnan, R. ; Sudarshan, T. S. Scratch-induced

microplasticity and microcracking in zirconium diboride–silicon carbide composite *Acta Mater.* **2008**, *56* (13), 3011-3022.

[4] Fujimoto, M. ; Wu, Y. ; Cao, J., High Precision Ultrasonically Assisted Internal Grinding (UAIG) of Difficult-to-machining Materials using Metal Bonded Diamond Wheels, in: The 6th International Conference on Leading Edge Manufacturing in 21st Century, 2011.

This page intentionally left blank.

Chapter 7 Conclusion and future recommendation

7.1 Conclusion

In this study, toward the development of an alternative machining method for the internal grinding of SiC ceramics, the UAIG technique is applied to the internal grinding of SiC ceramics. For this purpose, an experimental rig was constructed by installing an ultrasonic spindle onto a CNC internal grinder and experimental investigations on the machining characteristics of SiC ceramics workpiece were performed on the constructed rig. In order to optimize grinding parameters to achieve high product quality and productivity, a grinding force model for UAIG of SiC ceramics has been developed. Further, to deeply investigate the material removal mechanism in ultrasonic assisted internal grinding of SiC ceramics, the ultrasonic assisted scratching (UAS) tests were performed on SiC ceramics with a self-designed ultrasonic unit. Besides, a validated simulation model is developed to further investigate material removal mechanism in UAS. The obtained results of this study can be summarized as following:

In chapter 1, prevailing technologies, i.e., ultrasonic assisted grinding and ultrasonic assisted internal grinding was outlined. The classical and recent works were reviewed. The motivations for this study were outlined.

In chapter 2, the processing principal of UAIG was introduced. The experiment apparatus and experiment details were presented.

In chapter 3, experimental investigations on the machining characteristics of SiC ceramics workpiece were performed on the constructed rig. The conclusions are obtained as follows:

(1) The normal and tangential grinding force in UAIG are significantly reduced

compared with those in CIG. This is the valuable information for the application of UAIG technique to the internal grinding of SiC ceramics.

(2) The greater improvement of the form accuracy and surface quality are achieved in UAIG compared with those in CIG

(3) Abrasive grain protrusions are observed sufficiently in UAIG. The pullout of grain is considered as the main wheel wear mechanism in CIG while the micro-fracture as well as the slight grain pullout are the dominant mechanisms in UAIG. Observation of subsurface damage shows the fracture depth is decreased and cracks are alleviated.

In chapter 4, a grinding force model for UAIG of SiC ceramics has been developed. The model incorporates input variables of the grinding process and the UV. Comparing the forces predicted using the developed model with the experimental ones shows that the variation tendencies and the quantitative values of the predicted forces agreed reasonably with those of the experimental ones. Relationships between the input variables and the grinding forces in UAIG can be concluded as following:

(1) The grinding forces increase in the grinding process. Furthermore, the grinding forces are reduced in the UAIG compared to CIG, which is attributed to the formation of the smaller the undeformed chip cross sectional area.

(2) The grinding forces increase with the increasing of the workpiece rotational speed n_w and the wheel infeed rate V_c, whereas decrease with the increasing of the wheel rotational speed n_g, the UV amplitude A_u and the oscillation frequency f_o; the influence of the wheel rotational speed n_g, the workpiece rotational speed n_w and the wheel infeed rate V_c on grinding force are much pronounced, whereas that of the UV amplitude A_u and the oscillation frequency f_o are not very noticeable.

(3) The force reduction of UV can be enhanced either by decreasing the wheel rotational speed n_g, the workpiece rotational speed n_w and the wheel infeed rate V_c or increasing the UV amplitude A_u and the oscillation frequency f_o.

In chapter 5, to comprehend the material removal mechanism in the ultrasonic-assisted grinding of SiC ceramics, an ultrasonic-assisted scratching (UAS) test involving SiC ceramics specimen was performed on an in-house-produced

experimental setup. The material removal characteristics in the UAS test were compared to the conventional scratching (CS) test without ultrasonic vibration. The results and conclusion can be summarized as follows:

(1) Both in CS and UAS processes, three types of material deformation/fracture are successively generated along the scratching trace: the ductile removal mode, ductile–brittle transition mode, and brittle removal mode; the scratching groove formed appears straight in the CS process while it is sinusoidal in the UAS process.

(2) The UV in the direction that vertical to work-surface strongly contributes to the material removal, whereas the UV in the direction that parallel to work-surface only results in variation of the cutting trace and hardly contributes to the material removal in the UAS process.

(3) The cutting ability of the tool was significantly improved by the assistance of the UV. Furthermore, the critical depth of cut is increased from 0.08 μm in CS to 0.125 μm in UAS, which is an increase of 56.25%.

(4) The deformation of the SiC ceramics in the UAS process is equivalent to the combined effect of dynamic cutting with a tangential scratch velocity and UV.

In chapter 6, in order to high accuracy internal grinding of SiC ceramics, the probability of internal grinding of SiC ceramics in ductile mode and grinding efficiency were observed. The results showed that critical depth of cut is increased in UAIG compared with that in conventional internal grinding (CIG), meaning that ductile mode grinding is easily achieved in UAIG; grinding efficiency is higher in brittle grinding mode compared to that in ductile grinding mode in UAIG. In addition, high accuracy can be achieved by UAIG under the recommended experiment conditions.

7.2 Future recommendation

The research in the ultrasonic assisted internal grinding is still in preliminary stage.

There are many topics and unclear points that need to be investigated to ensure the reliability to apply this technology on the actual machining. In what follows, some recommendations and notes were list for future work:

(1) Although the material removal behavior in ultrasonic assisted grinding has been sufficiently studied in this study, the material removal mechanism has not been explored fully. This work should be done in the future work.

(2) In this study, it is found that critical depth of cut in ultrasonic assisted grinding is deeper than that in the conventional grinding. This phenomenon also has been found in other researchers' works. However, the reason why critical depth of cut becomes deeper in ultrasonic assisted grinding has not been explored fully.

(3) Much more works should be devoted to the feasibility of the technique in practice.

Acknowledgements

This thesis work is a result of three years of hard work. It would be impossible to complete this work without the assistance and encouragement of many people. I would like to take this opportunity to express my appreciation to many people who have been helping me during my PhD study.

First and foremost, I must thank my advisor, Prof. of Dr. Yongbo Wu. I still remember the moment I came to Akita Prefectural University about three years ago. At that time, I knew nothing about the knowledge of manufacturering, how to do research, how to write a good paper, how to be a good researcher… In a word, I was a blank sheet of paper at that time. However, with Prof. Wu's constant support, guidance, sage advice, and infinite patience, the blank sheet of paper three years ago became a rich and colorful picture today. What I have learned from Prof. Wu will spur me to go on with scientific research and to be a good man throughout the rest of my life.

I would like to thank Dr. Dong Lu for her kind help and assistance in my journal paper revision. Without her countless help, papers could not be successfully published. I am thankful to Associate Professor Mitsuyoshi Nomura and Dr. Masakazu Fujimoto for their invaluable instructions during my PhD study. I also have to thank the Lab technical staff Mr. Seiichi Kimura for his extraordinarily technique support.

I was very fortunate to have participated in Prof. Wu's laboratory, and grateful thanks go to my peer research lab members, including but not limited to, Dr. Weixing Xu, Dr. Yaguo Li, Miss Huiru Guo, Mr. Youliang Wang, Mr. Tailing Zhu, Mr. Shouichi Sasaki, Mr. Ryutaro Mori, Mr. Naoki Kobayashi, Mr. Masashi Ohmura….

Thanks are due to, including but not limited to, the following people for sharing happy and indelible experience in Akita Prefectural University: Ms. Aki Asada, Dr. Wenqing Song, Dr. Li Jiao, Mr. Jingti Niu, Prof. Weiping Yang, Dr. Ye Li, Dr.

Xiongbo Wan, Dr. Yang Zhao, Dr. Zhiyong Feng, Dr. Lin Lei, Dr. Xueli Wu, Mr. Jinkui Ma, Mr. Xiaofeng Li, Mr. Wei Wang, Miss Daiyan Yao, Mr. Xingguo Zhang, Mr. PaiPai Pan, Miss Wenjuan Zhang, Miss Limin Zang, Miss Lijun Wang, Mr. Bin Wang, Mr. Liqiang Gu, Miss Baiyi Chen, Miss Fei Ding, Miss Jingyan Huang… Thanks my Akita Family- Family Saito, Thanks my Japanese teachers, Mrs. Aiba, Miss Toda.

Thanks are also due to the support from my family. Family members' support encourages me to walk in this long journey. I must thank my wife, Weiqun Zhang, whose unconditional love and support have been a bright light that shines on me even in the darkest hours, who motivated me and kept my spirit high whenever I wanted to give up. I love you and wouldn't change anything. To my mother, brother, mother-in-law, father-in-law, my sister-in-law, and my litter nephew, I am sorry for the long distance that separates us and sorrow the long distance has caused, and thank you, you're your undivided love and wishing me always the best.

Accomplishments

I. 博士学位論文に関するもの

著書(分担執筆)

1. Yongbo Wu, Yaguo Li, Jianguo Cao, and Zhiqiang Liang. “Chapter 4: Ultrasonic assisted fixed abrasive machining of hard-brittle materials in Techniques and Practical Applications” in ***Ultrasonics: Theory, Techniques and Practical Application***, H. Ayabito and M. Katsukawa ed., ISBN 978-1-62257-685-2. (第三章)

学術論文

1. Jianguo Cao, Yongbo Wu, Dong Lu, Masakazu Fujimoto, Mitsuyoshi Nomura. Material removal behavior in ultrasonic-assisted grinding of SiC ceramics from scratching test with a single diamond tool, ***International Journal of Machine Tools & Manufacture***, 79 (2014) 49–61 (IF : 2.74). (第五章)
2. Jianguo Cao, Yongbo Wu, Dong Lu, Masakazu Fujimoto, Mitsuyoshi Nomura. Fundamental machining characteristics of ultrasonic assisted internal grinding of SiC ceramics, ***Materials and Manufacturing Processes***, 29 (2014) 557–563. (IF: 1.48). (第三章)
3. J.G. Cao, Y. Wu, H.R. Guo, Y.G. Li, M. Fujimoto, A. Ohmura. Simulation investigation ultrasonically assisted grinding of SiC ceramics with single diamond abrasive grain, ***Key Engineering Materials***, 523-524 (2012) 178-183. (第五章)
4. 曹建国, 野村光由, 呉勇波, 藤本正和. SiC セラミックスの超音波援用研削における材料除去プロセスの研究, *砥粒加工学会誌*. (修正中). (第六章)

国際学術会議

1. Jianguo Cao, Yongbo Wu, Masakazu Fujimoto, Nomura Mitsuyoshi. Simulation investigation of the cutting process in ultrasonic assisted grinding of SiC ceramics from scratching test with a single diamond tool using smooth particle

hydrodynamic (SPH) method, eu**spen**'s 14th International Conference, Jun. 2-6, 2014, Dubrovnik, Croatia.（第五章）

2. Jianguo Cao, Yongbo Wu, Masakazu Fujimoto, Nomura Mitsuyoshi. Experimental investigation of material removal mechanism in ultrasonic assisted grinding of SiC ceramics using a single diamond tool, The 7th International Conference on Leading Edge Manufacturing in 21st Century, Nov. 7–8, 2013, Miyagi, Japan.（第五章）
3. Jianguo Cao, Yongbo Wu, Huiru Guo, Yaguo Li, Masakazu Fujimoto, Akira Ohmura. Simulation investigation of chip formation in ultrasonically assisted grinding of SiC ceramics with single diamond abrasive grain, The 14th International Conference on Precision Enginerring, Nov. 8–10, 2012, Hyogo, Japan.（第五章）

国内学術会議

1. 曹建国，呉勇波，藤本正和，野村光由，大村昭．超音波を援用した SiC セラミックスの内面研削における仕上面性状，2013 年度日本精密工学会東北支部学術講演会，秋田，2013.12.07.（第六章）
2. 曹建国，呉勇波，藤本正和，野村光由．SiC セラミックスの超音波援用内面研削の研究：単石ダイヤモンド工具を用いたスクラッチング試験による材料除去メカニズムの実験調査，2013 年度日本精密工学会春季大会，東京，2013.03.13–2013.03.15.（第五章）
3. 曹 建国，呉 勇波，藤本 正和，野村 光由，大村 昭．SiC セラミックスの超音波援用内面研削におけるメタルボンドダイヤモンド砥石の加工特性，日本機械学会第 9 回生産加工・工作機械部門講演会，秋田，2012.10.27–2012.10.28.（第三章）
4. 曹建国，呉勇波，郭会茹，李亜国，藤本正和．超音波振動を援用した SiC セラミックス内面の精密研削，2011 年度日本精密工学会東北支部学術講演会，宮城，2011.10.21.（第三章）

受賞

1. Student Scholarship. *The eu**spen**'s 14th International Conference,* Dubrovnik, Croatia, Jun. 2-6, 2014.

Ⅱ. その他関連業績

学術論文

1. H.R. Guo, Y. Wu, Y.G. Li, J.G. Cao, M. Fujimoto, S.D. Jacobs. Technical performance of zirconia-coated carbonyl-iron-particles based magnetic compound fluid slurry in ultrafine polishing of PMMA, ***Key Engineering Materials***, 523-524 (2012) 161-166.
2. Y.G. Li, Y. Wu, L. Zhou, H. Guo, J. Cao, M. Fujimoto, M. Kemmochi. Investigation into Chemo-Mechanical Fixed Abrasive Polishing of Fused Silica with the Assistance of Ultrasonic Vibration, ***Key Engineering Materials***, 523-524 (2012) 155-160.
3. Huiru Guo, Yongbo Wu, Li Jiao, Jianguo Cao, Yaguo Li. Ultrafine polishing of Nickle Phosphorus plating with magnetic compound fluid slurry, ***Journal of mechanical engineering,*** 49 (2012) 73-78.
4. Dong Lu, Qiang Wang, Yongbo Wu, Jianguo Cao, Huiru Guo. Fundamental Turning Characteristics of Inconel 718 by Applying Ultrasonic Elliptical Vibration on on the Base Plan, ***Materials and Manufacturing Processes***, (Minor revise, IF:1.48).

国際学術会議

1. M. Fujimoto, Y. Wu, J. Cao. High Precision Ultrasonically Assisted Internal Grinding (UAIG) of Difficult-to-machining Materials using Metal Bonded Diamond Wheels, ***Proceedings of The 6th International Conference on Leading Edge Manufacturing in 21st Century***, Nov. 8-10, 2011, Saitama, Japan.

国内学術会議

1. 李亜国, 呉勇波, 曹建国, 郭会茹, 藤本正和, 周立波. 石英ガラスの超音波援用化学的機械複合研削. 2012 年日本精密工学会春季大会, 首都大学東京, 東京, 2012.03.14–16.
2. 李亜国, 呉勇波, 曹建国, 郭会茹, 藤本正和. 超音波を援用した光学ガラスの化学機械複合研削. 2011 年日本精密工学会東北支部講演会, 宮城, 2011.10.21.
3. Huiru Guo, Yongbo Wu, Yaguo Li, Jianguo Cao, Masakazu Fujimoto, Stephen D.

Jacobs. Fundamental performance of zirconia-coated carbonyl-iron-particles based magnetic compound fluid slurry in ultrafine polishing of PMMA. 2011 年度精密工学会東北支部学術講演会, 宮城, 2011.10.21.